To The Graduate Council:

I am submitting herewith a thesis by Steven Wayne Russell entitled "The Development of Qualification Standards for Cast Duplex Stainless Steel." I have examined the final paper copy of this thesis for form and content and recommend that it be accepted in partial fulfillment of the requirements for the degree of Master of Science, with a major in Materials Science and Engineering.

Carl D. Lundin, Major Professor

We have read this thesis
And recommend its acceptance:

J E Spruiell

R. A. Buchanan

Accepted for the Council:

Vice Provost and Dean of
Graduate Studies

The Development of Qualification Standards for Cast Duplex Stainless Steel

A Thesis
Presented for the
Master of Science
Degree
The University of Tennessee, Knoxville

Steven W. Russell
August 2003

Thesis
2003
.R89

Copyright © 2003 by Steven W. Russell
All rights reserved

Dedication

This thesis is dedicated to my parents

Fred W. Russell

And

Joyce W. Russell

Who have always given me love, support, and encouragement, while making my academic and professional success their top priority.

This thesis is also dedicated to my brother

Dr. Gregory C. Russell

Whose own academic and professional success has driven me to this achievement.

Acknowledgements

The author would like to thank the following individuals for there contributions to this project and the completion of my academic degree. First, I would like to thank my thesis advisor Dr. Carl D. Lundin, who has given me excellent guidance and support throughout this endeavor. Sincere appreciation is also expressed to Dr. Raymond A. Buchanan and Dr. Joseph E. Spruiell for serving on my thesis committee.

I would also like to thank several classmates and members of the Materials Joining Research Group, Dr. Peng Liu, Yan Cui, Songqing Wen, Jerrid Holt, and Jaret Frafjord for their assistance and friendship.

A special thanks is expressed to Mr. Malcolm Blair, Vice President of the Steel Founders' Society (SFSA) for his commitment to research. Appreciation is expressed to Daniel DeMiglio (Lincoln Electric Company), Dr. George Vander Voort (Buehler Ltd.), Chris McCowan (NIST), Elaine Thomas (Atlas Foundry & Machine Company), Ron Bird (Stainless Foundry & Engineering, Inc.), Gil Catherwood (A.G. Anderson Ltd.), Ken Blankenship (Sherry Labs), Dr. John F. Grubb (Allegheny Ludlum), Jonathan Lee (Chicago Bridge & Iron Company), and Joe McEnerney (Gibson Tube) for their participation in the round robin test series.

Finally, I would like to thank the Department of Energy, the Steel Founders' Society of America, and the University of Tennessee for their academic and financial support.

Abstract

The scope of testing cast Duplex Stainless Steel (DSS) required testing to several ASTM specifications, while formulating and conducting industry round robin tests to verify and study the reproducibility of the results. ASTM E562 (Standard Test Method for Determining Volume Fraction by Systematic manual Point Count) and ASTM A923 (Standard Test Methods for Detecting Detrimental Intermetallic Phase in Wrought Duplex Austenitic/Ferritic Stainless Steels) were the specifications utilized in conducting this work. An ASTM E562 industry round robin, ASTM A923 applicability study, ASTM A923 industry round robin, and an ASTM A923 study of the effectiveness of existing foundry solution annealing procedures for producing cast DSS without intermetallic phases were implemented.

In the ASTM E562 study, 5 samples were extracted from various cast austenitic and DSS in order to have varying amounts of ferrite. Each sample was metallographically prepared by UT and sent to each of 8 participants for volume fraction of ferrite measurements. Volume fraction of ferrite was measured using manual point count per ASTM E562. FN was measured from the Feritescope® and converted to volume fraction of ferrite. Results indicate that ASTM E562 is applicable to DSS and the results have excellent lab-to-lab reproducibility. Also, volume fraction of ferrite conversions from the FN measured by the Feritescope® were similar to volume fraction of ferrite measured per ASTM E562.

In the ASTM A923 applicability to cast DSS study, 8 different heat treatments were performed on 3 lots of ASTM A890-4A (CD3MN) castings and 1 lot of 2205

wrought DSS. The heat treatments were selected to produce a wide range of cooling rates and hold times in order to study the suitability of ASTM A923 to the response of varying amounts on intermetallic phases [117]. The test parameters were identical to those used to develop ASTM A923 for wrought DSS. Charpy V-notch impact samples were extracted from the castings and wrought DSS and tested per ASTM A923 method B (Charpy impact test). Method A (sodium hydroxide etch test) was performed on one half of a fractured Charpy V-notch impact sample and Method C (ferric chloride corrosion weight loss test) was performed on another half. Test results for the three cast lots and one wrought lot indicate that ASTM A923 is relevant for detecting intermetallic phases in cast DSS.

In the ASTM A923 round robin study, five laboratories conducted ASTM A923 Methods A & C on cast DSS material and the lab-to-lab reproducibility of the data was determined. Two groups of samples were sent to the participants. Group 1 samples were tested per ASTM A923 Method A, group 2 samples were tested by ASTM A923 Method C. Testing procedures for this round robin study were identical to those used in the ASTM A923 applicability study. Results from this round robin indicate that there is excellent lab-to-lab reproducibility of ASTM A923 with respect to cast DSS and that ASTM A923 could be expanded to cover both wrought and cast DSS.

In the ASTM A923 study of the effectiveness of existing foundry solution annealing procedures for producing cast DSS without intermetallic phases, Ten heats of ASTM A890-4A (CD3MN) in the foundry solution annealed condition were tested per ASTM A923 Methods A, B, & C. Testing of these materials per ASTM A923 was used to

determine if the foundry solution anneal procedures were adequate to completely eliminate any intermetallic phases, which may have precipitated during the casting and subsequent heat treatment processes. All heats showed no sign of intermetallic phase per Method A, passed minimum Charpy impact energy requirements per Method B (> 40 ft-lbs @ -40°C (-40°F)), and showed negligible weight loss per Method C (< 10 mdd). These results indicate that the solution annealing procedure used by foundries is adequate to produce a product free from intermetallic phases.

Table of Contents

Heading	Page
I. Program Introduction	1
II. Project Goals	2
III. Literature Review	3
Introduction	3
Metallurgy of DSS	4
Secondary Phases	4
Sigma (σ) Phase	4
Chi (χ) Phase	9
R-Phase	9
π-Phase	11
Secondary Austenite (γ_2)	11
Cr_2N	12
Carbides $M_{23}C_6$ and M_7C_3	12
Cu-rich epsilon (ε) Phase	13
Microstructural Investigation Techniques	13
Alloying Elements	16
Chromium (Cr)	16
Molybdenum (Mo)	16
Nickel (Ni)	16
Nitrogen (N)	17
Manganese (Mn)	17
Copper (Cu)	17
Tungsten (W)	17
Effect of Solution Heat Treating	18
Effect of Heat Treatment Temperature	18
Effect of Other Heat Treatment Variables	20
Corrosion Behavior of Duplex Stainless Steels	22
Pitting Corrosion	22
Intergranular Corrosion	25
Toughness	25
Welding of DSS	26
Welding Metallurgy	26
Heat Affected Zone (HAZ)	27
Weld Fusion Zone	35
Ferrite Prediction and Measurement	36
WRC-1992 Diagram	38
The Schoeffer Diagram	40
Ferrite Measurement	42
Point Count	43
Magne-Gage: Magnetic Adhesion Method	44

Eddy Current Method: Magnetic Induction Method 46
Ferrite Number vs. Ferrite Percent 48
Weldability 48
Fusion Zone Solidification Cracking 49
Heat Affected Zone Liquation Cracking 50
Hydrogen Assisted Cold Cracking 50
Welding Procedures 51
Welding Processes 52
SMAW 54
GTAW 55
Other Welding Processes 57
Filler Metal 57
Shielding and Backing Gases 59
Other Welding Related Issues 61
Casting Related Issues 62
Casting Production 63
IV. Experimental Procedures 64
ASTM E562 Ferrite Measurement Round Robin Study 64
Materials 64
Testing Method 64
The Suitability of ASTM A923 for Detecting the Presence of Intermetallic Phases in Duplex Stainless Steel Castings 69
Materials 69
Heat Treatments 70
Testing Methods 70
Test Method B 70
Test Method A 74
Test Method C 77
ASTM A923 Method A & C Round Robin Study 79
Materials 79
Testing Methods 80
ASTM A923 Study of the Effectiveness of Existing Foundry Solution Annealing Procedures for Producing Cast DSS Without Intermetallic Phases 80
Materials 80
Heat Treatment 80
Test Methods 82
V. Results and Discussion 83
ASTM E562 Ferrite Measurement Round Robin Study 83
The Suitability of ASTM A923 for Detecting the Presence of Intermetallic Phases in Duplex Stainless Steel Castings 86
Test Method B 86
Test Method A 86
Test Method C 86

ASTM A923 Method A & C Round Robin Study 109
Test Method A 109
Test Method C 109
ASTM A923 Study of the Effectiveness of Existing Foundry Solution Annealing Procedures for Producing Cast DSS Without Intermetallic Phases 133
Test Method A 133
Test Method B 133
Test Method C 133
VI. Conclusions 145
References 148
Appendix: Specifications 165
Vita 167

List of Tables

Table		Page
Table 1.	Crystallographic Data for Various Phases	8
Table 2.	Five Step Contemporary Automated Preparation Practice	14
Table 3.	Heat Treatment Requirements by ASTM A 890-4A	19
Table 4.	Welding Process Characteristics	53
Table 5.	Round Robin Sample Set	64
Table 6.	Chemical Composition of Tested Materials	69
Table 7.	Heat Treatment Schedule	71
Table 8.	Chemical Composition of Foundry Solution Annealed Materials	81
Table 9.	Foundry Solution Anneal Heat Treatment Schedule	81
Table 10.	Volume Percent Ferrite	81
Table 11.	ASTM E562 Results	84
Table 12.	Charpy Impact Toughness at –40°C (-40°F)	87
Table 13.	Classification of Etch Structure	89
Table 14.	Corrosion Rates for ASTM A923 Study	106
Table 15.	Classification of Etch Structure	110
Table 16.	Corrosion Rates for ASTM A923 Round Robin Study	131
Table 17.	Classification of Etch Structure for Foundry Solution Anneal Study	136
Table 18.	Charpy Impact Toughness at –40°C (-40°F) for Foundry Solution Anneal Study	142
Table 19.	Corrosion Rates for Foundry Solution Anneal Study	143

List of Figures

Figure		Page
Figure 1.	Possible Precipitates in DSS	5
Figure 2.	Micrographs Showing Different Morphologies of σ-phase	7
Figure 3.	BSEM Micrograph Showing Contrast Difference for χ-phase and σ-phase Due to Difference in Chemical Composition	10
Figure 4.	Effect of Solution Annealing Temperature on Ferrite and Austenite Content	21
Figure 5.	Effect of Solution Annealing Temperature on the Relative Amounts of the Ferrite and Austenite Phases	23
Figure 6.	Modified Ternary Section of the Fe-Cr-Ni Phase Diagram Plotted Using the WRC-1992 Equivalent Relationships	30
Figure 7.	Micrographs Showing Microstructures of SAF 2205 and 2507 After Gleeble Simulation at $\Delta t = 93.0s$	31
Figure 8.	Schematic Showing HAZs Experience Different Thermal Cycles	33
Figure 9.	Schematic Diagram Illustrating the Relative Positions of the Different Thermal Cycles in a Two Pass Weld Deposit	34
Figure 10.	The Schaeffler's Diagram	37
Figure 11.	The WRC-1992 Diagram	39
Figure 12.	The Schoeffer Diagram	41
Figure 13.	Photograph of a Standard Mage-Gage	45
Figure 14.	Schematic of the Magnetic Induction Method	47
Figure 15.	Effect of Welding on Impact Toughness	56
Figure 16.	Effect of Shielding Gas Compositions on Pitting Corrosion Resistance of Duplex Stainless Steels	60

Figure 17.	Microstructure of Round Robin Sample "A", NaOH, 100x	65
Figure 18.	Microstructure of Round Robin Sample "E", NaOH, 100x	65
Figure 19.	Microstructure of Round Robin Sample "F", NaOH, 100x	66
Figure 20.	Microstructure of Round Robin Sample "J", NaOH, 100x	66
Figure 21.	Microstructure of Round Robin Sample "K", NaOH, 100x	67
Figure 22.	Actual Thermal History for Various Heat Treatments	71
Figure 23.	Charpy Impact Sample Extraction Location	72
Figure 24.	Charpy Impact Notch Geometry	72
Figure 25.	Charpy Impact Test Apparatus	73
Figure 26.	Unaffected Structure from ASTM A923	76
Figure 27.	Possibly Affected Structure from ASTM A923	76
Figure 28.	Affected Structure from ASTM A923	76
Figure 29.	Centerline Structure from ASTM A923	76
Figure 30.	Temperature Controlled Water Bath	78
Figure 31.	Comparison of Volume Fraction of Ferrite per Feritescope® and ASTM E562 Manual Point Count	85
Figure 32.	Charpy Impact Toughness at –40°C (-40°F)	88
Figure 33.	Microstructure of 2205-A-3, NaOH, 400x	90
Figure 34.	Microstructure of 41NCC-A-1, NaOH, 400x	90
Figure 35.	Microstructure of 42RA-1, NaOH, 400x	91
Figure 36.	Microstructure of CD3-A-2, NaOH, 400x	91
Figure 37.	Microstructure of 2205-B-2, NaOH, 400x	92
Figure 38.	Microstructure of 41NCC-B-2, NaOH, 400x	92

Figure 39. Microstructure of 42R-B-1, NaOH, 400x 93

Figure 40. Microstructure of CD3-B-1, NaOH, 400x 93

Figure 41. Microstructure of 2205-C-1, NaOH, 400x 94

Figure 42. Microstructure of 41NCC-C-1, NaOH, 400x 94

Figure 43. Microstructure of 42R-C-1, NaOH, 400x 95

Figure 44. Microstructure of CD3-C-2, NaOH, 400x 95

Figure 45. Microstructure of 2205-D-1, NaOH, 400x 96

Figure 46. Microstructure of 41NCC-D-2, NaOH, 400x 96

Figure 47. Microstructure of 42R-D-1, NaOH, 400x 97

Figure 48. Microstructure of CD3-D-2, NaOH, 400x 97

Figure 49. Microstructure of 2205-E-1, NaOH, 400x 98

Figure 50. Microstructure of 41NCC-E-1, NaOH, 400x 98

Figure 51. Microstructure of 42R-E-1, NaOH, 400x 99

Figure 52. Microstructure of CD3-E-3, NaOH, 400x 99

Figure 53. Microstructure of 2205-F-3, NaOH, 400x 100

Figure 54. Microstructure of 41NCC-F-2, NaOH, 400x 100

Figure 55. Microstructure of 42R-F-3, NaOH, 400x 101

Figure 56. Microstructure of CD3-F-2, NaOH, 400x 101

Figure 57. Microstructure of 2205-G-2, NaOH, 400x 102

Figure 58. Microstructure of 41NCC-G-3, NaOH, 400x 102

Figure 59. Microstructure of 42R-G-2, NaOH, 400x 103

Figure 60. Microstructure of CD3-G-2, NaOH, 400x 103

Figure 61. Microstructure of 2205-H-2, NaOH, 400x 104

Figure 62. Microstructure of 41N-H-3, NaOH, 400x 104

Figure 63. Microstructure of 42R-H-1, NaOH, 400x 105

Figure 64. Microstructure of CD3-H-1, NaOH, 400x 105

Figure 65. Corrosion Rates for ASTM A923 Study 107

Figure 66. Microstructure of 41NCC-A-1, NaOH, 400x, Participant 1 111

Figure 67. Microstructure of 41NCC-A-1, NaOH, 400x, Participant 2 111

Figure 68. Microstructure of 41NCC-A-1, NaOH, 500x, Participant 3 112

Figure 69. Microstructure of 41NCC-A-1, NaOH, 500x, Participant 4 112

Figure 70. Microstructure of 41NCC-A-1, NaOH, 400x, Participant 5 113

Figure 71. Microstructure of 41NCC-B-3, NaOH, 400x, Participant 1 113

Figure 72. Microstructure of 41NCC-B-3, NaOH, 400x, Participant 2 114

Figure 73. Microstructure of 41NCC-B-3, NaOH, 500x, Participant 3 114

Figure 74. Microstructure of 41NCC-B-3, NaOH, 500x, Participant 4 115

Figure 75. Microstructure of 41NCC-B-3, NaOH, 400x, Participant 5 115

Figure 76. Microstructure of 41NCC-C-2, NaOH, 400x, Participant 1 116

Figure 77. Microstructure of 41NCC-C-2, NaOH, 400x, Participant 2 116

Figure 78. Microstructure of 41NCC-C-2, NaOH, 500x, Participant 3 117

Figure 79. Microstructure of 41NCC-C-2, NaOH, 500x, Participant 4 117

Figure 80. Microstructure of 41NCC-C-2, NaOH, 400x, Participant 5 118

Figure 81. Microstructure of 41NCC-D-1, NaOH, 400x, Participant 1 118

Figure 82. Microstructure of 41NCC-D-1, NaOH, 400x, Participant 2 119

Figure 83. Microstructure of 41NCC-D-1, NaOH, 500x, Participant 3 119

Figure 84. Microstructure of 41NCC-D-1, NaOH, 500x, Participant 4 120

Figure 85. Microstructure of 41NCC-D-1, NaOH, 400x, Participant 5 120

Figure 86. Microstructure of 41NCC-E-2, NaOH, 400x, Participant 1 121

Figure 87. Microstructure of 41NCC-E-2, NaOH, 400x, Participant 2 121

Figure 88. Microstructure of 41NCC-E-2, NaOH, 500x, Participant 3 122

Figure 89. Microstructure of 41NCC-E-2, NaOH, 500x, Participant 4 122

Figure 90. Microstructure of 41NCC-E-2, NaOH, 400x, Participant 5 123

Figure 91. Microstructure of 41NCC-F-1, NaOH, 400x, Participant 1 123

Figure 92. Microstructure of 41NCC-F-1, NaOH, 400x, Participant 2 124

Figure 93. Microstructure of 41NCC-F-1, NaOH, 500x, Participant 3 124

Figure 94. Microstructure of 41NCC-F-1, NaOH, 500x, Participant 4 125

Figure 95. Microstructure of 41NCC-F-1, NaOH, 400x, Participant 5 125

Figure 96. Microstructure of 41NCC-G-1, NaOH, 400x, Participant 1 126

Figure 97. Microstructure of 41NCC-G-1, NaOH, 400x, Participant 2 126

Figure 98. Microstructure of 41NCC-G-1, NaOH, 500x, Participant 3 127

Figure 99. Microstructure of 41NCC-G-1, NaOH, 500x, Participant 4 127

Figure 100. Microstructure of 41NCC-G-1, NaOH, 400x, Participant 5 128

Figure 101. Microstructure of 41NCC-H-1, NaOH, 400x, Participant 1 128

Figure 102. Microstructure of 41NCC-H-1, NaOH, 400x, Participant 2 129

Figure 103. Microstructure of 41NCC-H-1, NaOH, 500x, Participant 3 129

Figure 104. Microstructure of 41NCC-H-1, NaOH, 500x, Participant 4 130

Figure 105. Microstructure of 41NCC-H-1, NaOH, 400x, Participant 5 130

Figure 106. Unaffected Structure, No Evidence of Intermetallic Phase, NaOH, 400x 134

Figure 107. Possibly Affected Structure, Interphase Boundaries Show Fine Waviness, NaOH, 400x 134

Figure 108. Affected Structure 1, Intermetallic Phase is Evident, NaOH 400x 135

Figure 109. Affected Structure 2, Intermetallic Phase is Evident, NaOH, 400x 135

Figure 110. Microstructure of 4A-SA-1, NaOH, 400x 136

Figure 111. Microstructure of 4A-SA-2, NaOH, 400x 137

Figure 112. Microstructure of 4A-SA-3, NaOH, 400x 137

Figure 113. Microstructure of 4A-SA-4, NaOH, 400x 138

Figure 114. Microstructure of 4A-SA-6, NaOH, 400x 138

Figure 115. Microstructure of 4A-SA-7, NaOH, 400x 139

Figure 116. Microstructure of 4A-SA-8, NaOH, 400x 139

Figure 117. Microstructure of 4A-SA-9, NaOH, 400x 140

Figure 118. Microstructure of 4A-SA-10, NaOH, 400x 140

Figure 119. Microstructure of 4A-SA-11, NaOH, 400x 141

Figure 120. Charpy Impact Toughness at –40°C (-40°F)for Foundry Solution Anneal Study 143

I. Program Introduction

Duplex stainless steels (DSS), which were originally developed in Europe during the 1930s, have been gaining popularity in the U.S. in recent years. At one time, DSS were considered an exotic alloy but now are considered industrial steel thanks to its widespread use in the paper, chemical, and off-shore petroleum industry.

Wrought DSS has been enjoying rapid growth in the U.S. market while its cast counterpart has had limited use due to very few qualification standards being available. This program was designed to develop a database of information for developing cast DSS practices and standards from the existing wrought DSS practices and standards. Two of the main factors which cause cast DSS to perform at less than desirable levels is an inappropriate austenite/ferrite balance and the precipitation of detrimental intermetallic phases during the casting or subsequent welding process. This program will address the applicability ASTM E562 (Standard Test Method for Determining Volume Fraction by Systematic Manual Point Count) for determining ferrite content in DSS and will also address the applicability of ASTM A923 (Standard Test Methods for Detecting Detrimental Intermetallic Phase in Wrought Duplex Austenitic/Ferritic Stainless Steels) to cast DSS. The data can then be used in further development of cast DSS specifications which may increase the use of cast DSS in U.S. industry.

II. Project Goals

The following project goals have been established for this program:

1. Establish the lab-to-lab reproducibility of ASTM E562 "Standard Test Method for Determining Volume Fraction by Systematic Manual Point Count" with respect to ferrite volume fraction measurement in DSS.
2. Compare ASTM E562 round robin results to Feritescope® measurement results with respect to ferrite volume fraction measurement in DSS.
3. Determine the suitability of ASTM A923 "Standard Test Methods for Detecting Detrimental Intermetallic Phase in Wrought Duplex Austenitic/Ferritic Stainless Steels" for ASTM A890-4A cast DSS.
4. Determine the lab-to-lab reproducibility of ASTM A923 Method A (Sodium Hydroxide Etch Test for Classification of Etch Structures of Duplex Stainless Steels) and Method C (Ferric Chloride Corrosion Test for Classification of Structures of Duplex Stainless Steels" for ASTM A890-4A cast DSS.

III. Literature Review

Introduction

DSS was developed in Europe in the early 1930's. Development of DSS progressed slowly until the early 1950's, when the first generation alloys were first produced. These early alloys were found to have a poor balance of austenite and ferrite, thus producing poor mechanical properties and corrosion resistance. In a second generation of these alloys, the austenite and ferrite balance was more stringently controlled, which led to increased performance. DSS has been gaining popularity in the United States due to its excellent resistance to stress corrosion cracking along with its combination of strength and pitting and corrosion resistance.

DSS has been enjoying widespread use in European industry while just recently being applied to industrial use in the United States. DSS is commonly used in the pulp and paper industry, chemical industry, and in corrosive chemical containment pressure vessels [130].

Although few standards exist it has been recognized that these metallurgically complex alloys require high processing controls to ensure that they can be produced economically and with desirable properties. Standards for wrought DSS have been established and research dedicated to the establishment of suitable cast DSS standards is currently being conducted.

Metallurgy of DSS

Duplex defines a stainless steel that contains both austenite and ferrite. The simultaneous presence of both phases makes DSS show excellent resistance to stress corrosion cracking (SCC). While the optimum austenite/ferrite ratio is 50%, the austenite/ferrite balance generally depends on the chemical composition of the alloy.

The presence of ferrite is beneficial in reducing hot cracking tendency during casting and welding. However, the presence of ferrite also raises the risk of secondary phase precipitation, which can be detrimental to mechanical properties and corrosion resistance.

Secondary Phases

Secondary phases describe the different precipitates that have been found in DSS. Each of the following phases vary with respect to their formation mechanisms, appearance, and effect on properties but all have been found to be detrimental in some way. Figure 1 [1] shows the possible secondary phases in DSS.

Sigma (σ) Phase

The deleterious Cr, Mo rich σ-phase is a hard embrittling precipitate, which forms between 650 and 1000°C often associated with a reduction in both impact properties and corrosion resistance [1]. The detrimental effects to corrosion can be attributed to the high Cr and Mo content in σ-phase, typically Fe-30Cr-4Ni and 4-7 Mo [3], depleting the surrounding ferrite matrix of these elements, which are necessary for corrosion resistance.

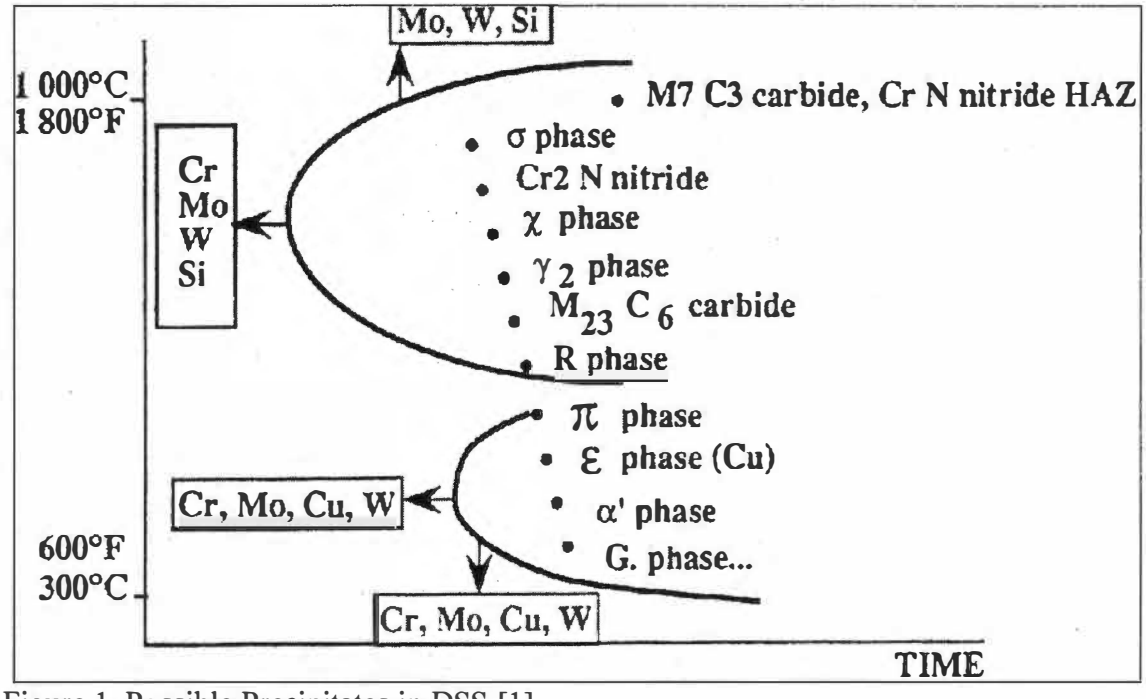


Figure 1. Possible Precipitates in DSS [1]

Sigma phase has been found to nucleate preferentially at ferrite/ferrite/austenite triple points and growth occurs along ferrite/ferrite boundaries [13, 41]. Atamert and King [43] suggested that sigma phase preferentially grows into ferrite because the ferrite phase is thermodynamically metastable at temperatures where sigma phase precipitates. Therefore, formation of sigma is simply the transformation of ferrite phase from a metastable state to an equilibrium state.

Sigma phase has different morphologies depending on whether it precipitates at ferrite/austenite of ferrite/ferrite interfaces or if it co-precipitates with secondary austenite. Figure 2 [22] illustrates the different morphologies of sigma phase.

Sigma phase is distinguishable by SEM-EDS. This technique defines the ratio of iron-chromium-molybdenum and is often used to determine whether the precipitates are sigma phase or some other secondary phase.

The removal of sigma phase from cast or as-rolled materials is usually performed through a solution annealing heat treatment. The solution annealing heat treatment reaches a high enough temperature to completely dissolve sigma and the steel is then rapid cooled to ensure that sigma does not reform. High solution annealing temperatures tend to increase the volume fraction of ferrite, which consequently is diluted with respect to ferrite forming elements; therefore, sigma formation is suppressed [8].

Identification of sigma phase by chemical composition is not always definitive. The identification of precipitates should be combined with crystallography deteminations. Table 1 [38] shows the crystallographic data for the types of precipitates that occur in DSS.

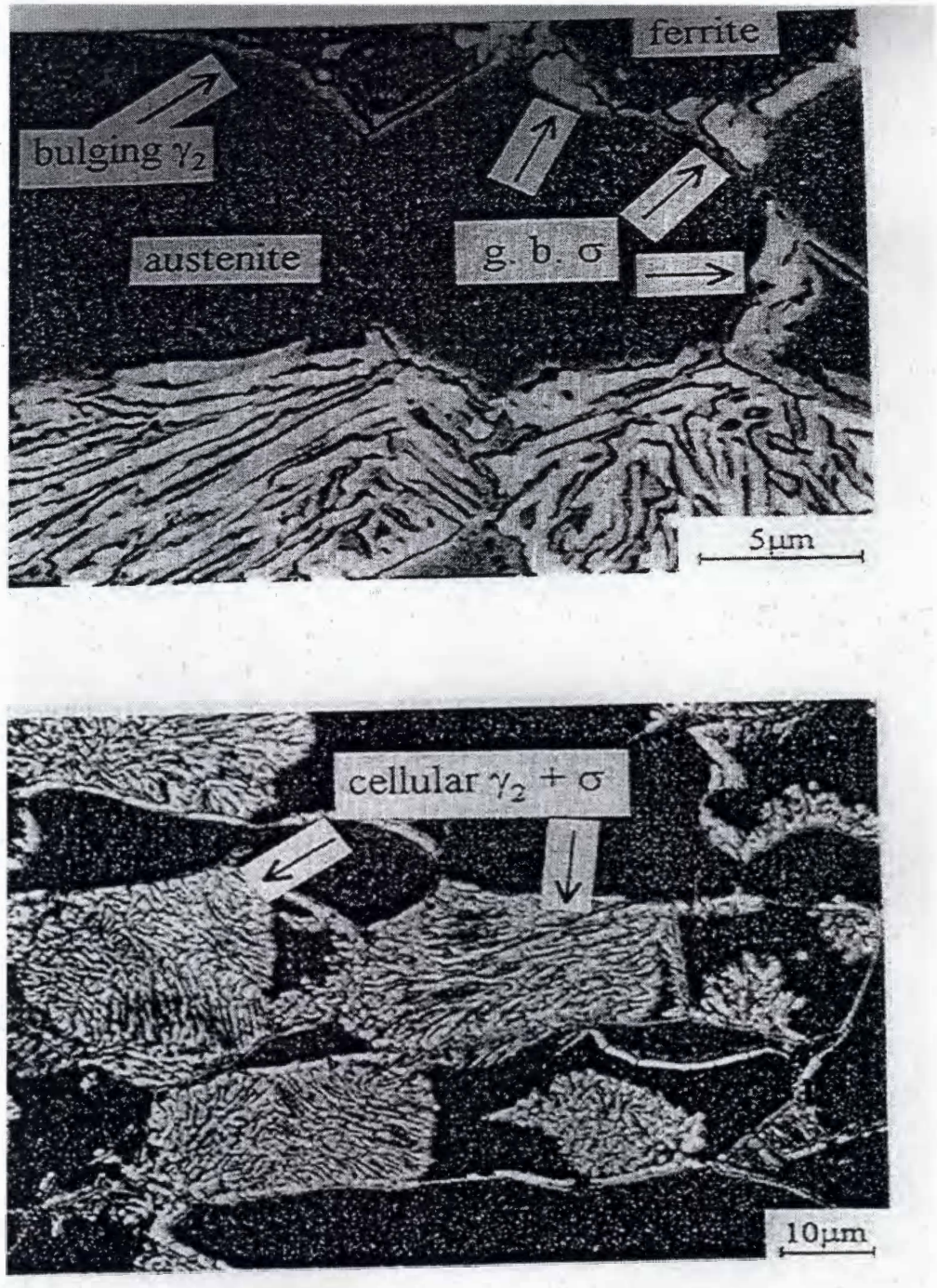


Figure 2. Micrographs Showing Different Morphologies of σ-phase [22]

Table 1. Crystallographic Data for Various Phases [38]

Type of Precipitate	Lattice Type	Space Group	Lattice Parameter
δ	BCC	Im3m	a = 2.86 – 2.88
$\gamma/(\gamma_2)$	FCC	Fm3m	a = 3.58 – 3.62
σ	tetragonal	$P4_2/mnm$	a = 8.79, c = 4.54
χ	cubic	I43m	a = 8.92
R	rhombohedral	R3	a = 10.90, c = 19.34
π	cubic	$P4_132$	a = 6.47
Cr_2N	hexagonal	P31m	a = 4.80, c = 4.47
$M_{23}C_6$	cubic	Fm3m	a = 10.56 –10.65
M_7C_3	hexagonal	Pnma	A = 4.52, b = 6.99, c = 12.11

Chi (χ) Phase

χ-phase forms between 700 and 900°C and has similar Cr content and much higher Mo content than σ-phase. χ-phase usually exists in much smaller quantities than σ-phase[10], and also is associated with a reduction in both impact properties and corrosion resistance [133]. However, χ-phase and σ-phase usually exist simultaneously, thus it is difficult to study their individual effect on impact properties and corrosion resistance [1]. Also, it has been indicated that χ-phase precipitates faster in the range of800 to 850°C and upon long-term aging, χ-phase will convert into σ-phase [11].

χ-phase usually forms at the δ/γ interface and grows into the ferrite, but unlike σ-phase, χ-phase is not distinguishable by optical light microscopy (OLM) and must be studied using either TEM or backscattered (BS) SEM [11]. χ –phase can be distinguished from σ-phase by TEM due the difference in crystallographic structure, as shown in Table 1, and by BS SEM because of the brighter contrast of χ-phase compared to σ-phase. Figure 3 [12], illustrates the difference between the two phase using BS SEM.

R-Phase

R-phase forms between 550 and 800°C and is a Mo rich intermetallic compound having a rhombohedral crystal structure, as shown in Table 1. R-phase, like other intermetallic compounds, reduces impact properties and corrosion resistance. R-phase forms rapidly from 550 to 650°C and at higher temperatures converts to σ-phase with relatively short aging time.

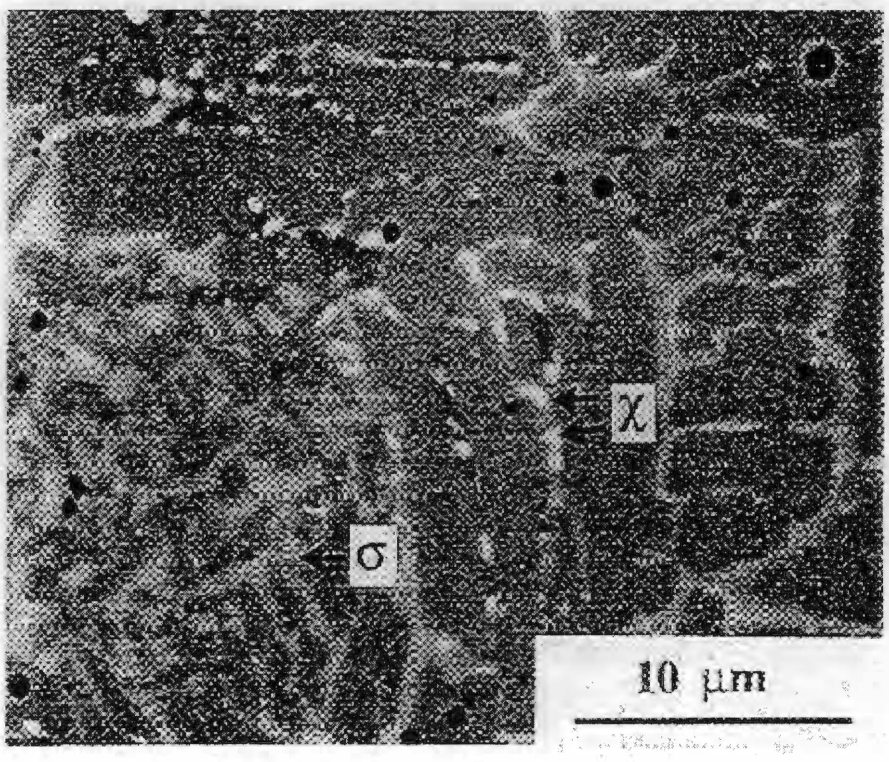


Figure 3. BSEM Micrograph Showing Contrast Difference for χ-phase and σ-phase Due to Difference in Chemical Composition [12]

R-phase is not distinguishable by OLM and is difficult to identify even with advanced techniques such as TEM or SEM. Combinations of TEM and SEM/EDS are usually employed for the identification of R-phase.

π-Phase

π-Phase has been identified as a nitride and is found at intragranular sites in DSS after isothermal heat treatment at 600°C for several hours. Because of its Cr and Mo enriched composition, π-phase has sometimes been confused with σ-phase. Similar to other intermetallic precipitates, π-phase is also detrimental to toughness and pitting corrosion resistance [13]. π-phase is also not distinguishable by OLM techniques. TEM is normally used for identification [11].

Secondary Austenite (γ_2)

Secondary Austenite (γ_2) is termed as such because it has a FCC crystal structure, which is the same crystallographic structure as primary austenite. γ_2 is usually found at austenite/ferrite boundaries or inside ferrite grains [12]. γ_2 forms relatively quickly and by different mechanisms as a function of temperature.

Below 650°C, γ_2 is similar in composition to the surrounding ferrite, suggesting a diffusionless transformation, with characteristics similar to martensite formation [14]. The orientation relationship is found to obey the Nishiyama-Wasserman (N-W) relationship [11].

At a temperature range between 650 and 800°C, where diffusion is rapid, Widmanstätten austenite can form [15]. In this temperature range, γ_2 obeys the Kurdjumov-Sachs relationship, its formation involves diffusion as it is enriched in Ni compared to the ferrite matrix [16]. Also, in this temperature range, the composition of γ_2, with respect to Cr and N, is substantially lower than that of primary austenite.

In the temperature range between 700 and 900°C, an eutectoid reaction of γ_2 + σ-phase can form. In this reaction the Cr and Mo rich σ-phase is surrounded by γ_2, which absorbs Ni and becomes depleted of Cr and Mo.

Cr_2N

Cr_2N is formed after a high temperature solution annealing heat treatment and rapid cooling. This formation is caused by the supersaturation of nitrogen in the ferrite matrix during the rapid cool, thus the amount of Cr_2N present is a function of the amount of nitrogen present. Formation occurs in the ferrite matrix between 700 and 900°C and takes the form of intragranularly precipitated elongated particles or intergranularly precipitated globular particles.

Carbides $M_{23}C_6$ and M_7C_3

$M_{23}C_6$ carbides precipitate rapidly between 650 and 950°C and require less than one minute to form at 800°C. M_7C_3 carbides precipitate between 950 and 1050°C and, like $M_{23}C_6$, are predominantly located at austenite/ferrite boundaries.

Cu-rich epsilon (ε) Phase

Cu-rich ε-Phase occurs only in DSS alloys containing Cu. ε-phase precipitates after 100 hours at 500°C because of the supersaturation of ferrite due to the decrease in solubility at lower temperatures. ε-phase has shown the ability to refine microstructure but the effect on toughness and corrosion properties has not been very well documented.

Microstructural Investigation Techniques

Vander Voort [39] stated in general, preparing DSS is not difficult, at least to a level where the true structure can be seen. However, to remove all scratches can be more of a challenge. As some of the precipitates that can form are harder than either matrix phase, relief may occur. A contemporary method has been described for preparing DSS specimens. This procedure, shown in Table 2, produces better, more consistent surfaces where the true microstructure can be revealed clearly and sharply with good contrast.

Microstructural evaluation of DSS must be performed with the proper etching techniques in order to use OLM or SEM. Numerous etchants and electro-chemical etching techniques have been identified for revelation of the microstructures in DSS.

The following is a list of various etching techniques and the types of microstructure they reveal:

1) 10% KOH electrolytical etchant, 5 V. Ferrite is stained yellow, austenite is unattacked, σ-phase is stained reddish brown, and carbides are stained black [17].
2) A two-step electrolytical etching technique was developed by Nilson et al. [12] to reveal the contrast of intermetallic phase. Step 1 uses dilute HNO_3 to reveal

Table 2. Five Step Contemporary Automated Preparation Practice [39]

Step	Surface/Abrasive	Rpm	Direction	Load (lbs)	Time (minutes)
1	240-grit SiC	240-300	Head and plate rotating in same direction	6	Remove All Cutting Damage
2	9-μm diamond on UltraPol™ Cloth	120-150	Head and plate rotating in same direction	6	5
3	3-μm diamond on Texmet 1000® Cloth	120-150	Head and plate rotating in same direction	6	3
4	1-μm diamond on Trident™ Cloth	120-150	Head and plate rotating in same direction	6	2
5	Masterprep™ alumina suspension on a Chemomet® Cloth	120-150	Head and plate rotating in opposite direction	6	1.5-2

phase boundaries. Step 2 uses saturated KOH to enhance precipitate contrast. The use of 2.2g $(NH_4)HF_2$, 0.2g $K_2S_2O_5$, 18 ml HCl, 100 ml distilled H_2O, known as Beraha etchant, produces as-welded microstructures with high contrast secondary austenite when etched for 10 to 20 seconds. This technique also colors ferrite blue while austenite remains uncolored.

3) Cheng et al. [18] used a heated solution of 50 g $K_3Fe(CN)_6$, 30 g KOH, and 100 ml distilled H_2O for DSS etching.
4) 1.5g $CuCl_2$, 33 ml HCl, 33 ml alcohol, and 33 ml distilled H_2O, known as Kallings reagent, is an acid chloride solution that does not require electrolytical techniques or heating. Kallings reagent stains ferrite dark and austenite light [19].
5) 10% Oxalic, 40% NaOH, and Glyceregia electrolytical etching are the most common etchants used on DSS.

OLM techniques are used for the revelation of ferrite and austenite microstructure as well as for the revelation of σ-phase, but this technique is not sufficient for the identification of other secondary phases. Also, SEM/EDS is not sufficient due to the similar chemical compositions of many of the secondary phases. TEM is time-consuming and sometimes costly but it is the most effective way of revealing and identifying secondary phases. TEM requires a sample thinning solution of 20% perchloric acid, 10% glycerol, and 70% ethyl alcohol, which is performed at 0°C and 25 to 45V on a twin jet polishing unit [20].

Alloying Elements

Alloying elements affect properties and microstructure of DSS in various ways, thus each must be understood in order to maximize the effectiveness and to prevent the alloying element from becoming harmful instead of beneficial to the complex metallurgical system.

Chromium (Cr)

Cr is a strong ferrite former and is the essential element for the excellent corrosion resistance of stainless steels. However, there is a limit to the level of Cr that can be added, as the beneficial effect of ever higher levels is negated by the enhanced precipitation of intermetallic phases such as σ-phase, as shown in Figure 1 [1].

Molybdenum (Mo)

Mo has a similar effect on ferrite stability as Cr and increases crevice corrosion and pitting resistance. The mechanism by which Mo increases the pitting resistance has been found to be the suppression of active sites via formation of an oxy-hydroxide or molybdate ion [2].

Nickel (Ni)

Ni is a strong austenite former and is added to maintain the ferrite/austenite balance in DSS. Excessive Ni can enhance the precipitation of σ-phase by promoting greater concentrations of ferrite stabilizers such as Cr and Mo in the ferrite matrix.

Nitrogen (N)

N, like Ni, is a strong austenite former and can often be used in place of Ni for austenite stabilization. N also effectively increases strength without the risk of sensitization, increases localized corrosion performance, and critical pitting temperature (CPT).

Manganese (Mn)

Mn increases abrasion, wear resistance, and tensile properties without a loss in ductility [4]. However, Mn additions in excess of 3% and 6%, for nitrogen levels of 0.1% and 0.23% respectively, significantly decrease the CPT due to the increased likelihood of MnS inclusions, which can act as initiation sites for pits [5].

Copper (Cu)

Cu plays a minor role in DSS but can increase the corrosion resistance when added not in excess of 2%. However, additions of Cu can cause the supersaturation of ferrite due to the decrease in solubility at lower temperatures, which can lead to the precipitation of extremely fine Cu-rich ε-phase particles after 100 hours at 500°C [6]. This can severely limit the service performance of DSS at temperatures near or in excess of 500°C.

Tungsten (W)

W additions of up to 2% in DSS improves the pitting resistance and crevice corrosion resistance [7]. W is known to encourage the formation of intermetallics in the

700 to 1000°C temperature range, as shown previously in Figure 1 [1], and encourages secondary austenite [8]. Also, W has been shown to form chi phase more rapidly than otherwise similar chemical compositions without the W addition [9].

Effect of Solution Heat Treating

Slow cooling of DSS from the solution annealing temperature has been found to lead to precipitation of detrimental intermetallic phases. DSS is normally water quenched from elevated temperatures but even this type of cooling can be slow enough at the center of heavy sections to allow formation of intermetallic phases. Proper solution annealing heat treatments are employed to dissolve intermetallic phases and restore mechanical properties and corrosion resistance to cast and wrought DSS.

The influences of certain elements play a role in defining the correct solution annealing temperatures. Ni stabilizes sigma phase and Cr and Mo promote the formation of sigma and other detrimental phases. Table 3 shows the correct solution annealing temperature for cast DSS as defined by ASTM A 890-94a.

Effect of Heat Treatment Temperature

A maximum solution annealing temperature must be specified because too high of a temperature can result in an increase of ferrite [22]. The modified ternary section of the Fe-Cr-Ni phase diagram illustrates this increase in ferrite with respect to high solution annealing temperatures. Higher ferrite content is not the only effect of high solution annealing temperatures; these high temperatures can also:

Table 3. Heat Treatment Requirements by ASTM A890-94a

Grade	Heat Treatment
4A	Heat to 1120°C for sufficient time to heat casting uniformly to temperature and water quench, or the casting may be furnace cooled to 1010°C minimum, hold for 15 minutes minimum and then water quench. A rapid cool by other means may be employed in lieu of water quench.
5A	Heat to 1120°C minimum, hold for sufficient time to heat casting to temperature, furnace cool to 1045°C minimum, quench in water or rapid cool by other means.
6A	Heat to 1100°C minimum, hold for sufficient time to heat casting uniformly to temperature, quench in water or cool rapidly by other means.
7A	Heat to 1040°C minimum, hold for sufficient time to heat casting uniformly, quench in water or rapid cool by other means.

1) Lower the portioning coefficients [23]. This makes DSS less susceptible to intermetallic phase transformations but more sensitive to secondary austenite and Cr_2N formation [34].
2) Decrease chromium content and increase nickel content in the ferrite as shown in Figure 4 [22]. Consequently, Lai et al. [22] also demonstrated that this effect dramatically slows the formation of sigma phase.
3) Change the morphology of austenite and ferrite. Radenkovic et al. [21] observed that the morphology of the austenite changes from a relatively discontinuous network to grain boundary morphology. Grain boundaries also become smoother than their previous irregular shape as solution annealing temperature increases. An increase in grain size has also been observed with an increase in peak temperature [24].

Solution annealing temperatures should be chosen, as a function of specific heat chemistry instead of selecting a temperature from the ASTM required minimum. High solution annealing temperatures are required to dissolve sigma phase and obtain a required ferrite content but the temperature must be controlled as not to increase the ferrite to an abnormally high level, which can cause a decrease in impact toughness, ductility, and corrosion resistance.

Effect of Other Heat Treatment Variables

As discussed in the previous section, heat treatment at excessively high temperatures is undesirable but other variables in the heat treatment of DSS also need to be stringently

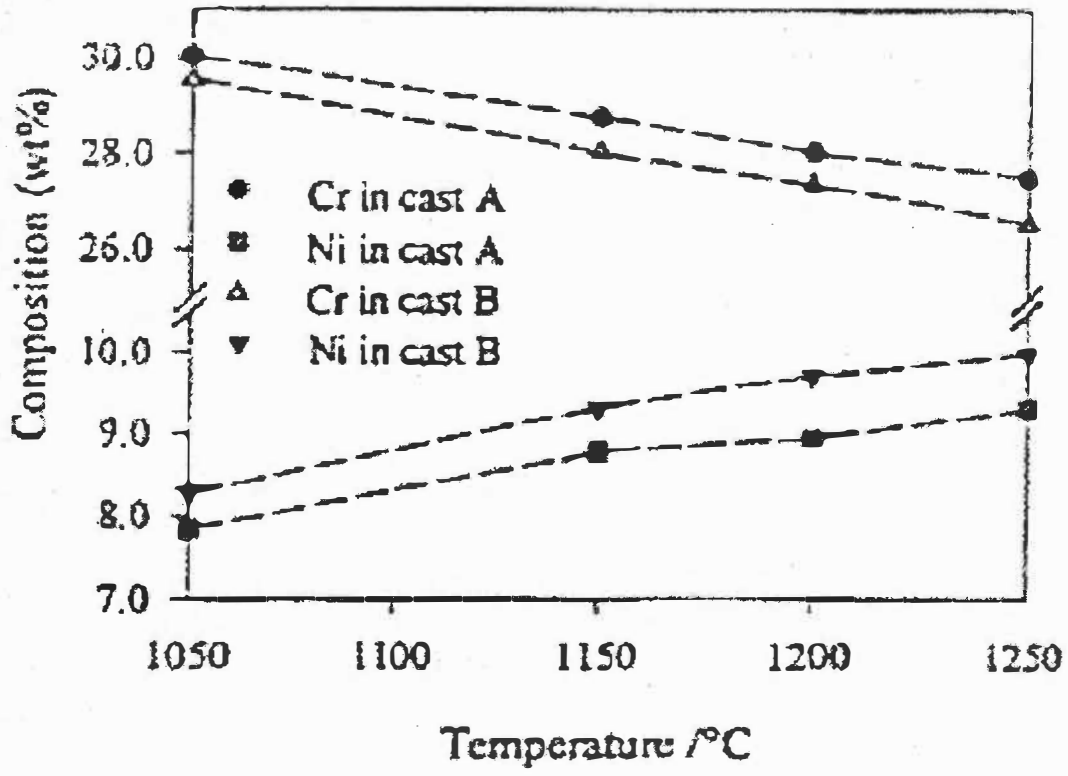


Figure 4. Effect of Solution Annealing Temperature on Ferrite and Austenite Content [22]

controlled. Figure 5 [22], shows the effect of annealing temperature on the relative amounts ferrite and austenite. Excessively high heat treatment temperature can cause heat treatment time to have an even greater effect on ferrite content.

Step annealing/cooling heat treatment procedures for SAF 2205 and Ferralium 255 weld metals were analyzed by Kotecki [25]; no particular advantages or disadvantaged were observed.

Corrosion Behavior of Duplex Stainless Steels

It is well known that DSS has a high resistance to stress corrosion cracking (SCC) due to its ferrite/austenite microstructure. SCC is not in the scope of this research so it will not be discussed in this review. However, DSS is affected by two other corrosion mechanisms known as pitting corrosion and intergranular corrosion.

Pitting Corrosion

The pitting resistance of DSS in a chloride environment has been related essentially to Cr, Mo, and Ni. The pitting resistance equivalent number, PREN, was developed to relate the amount of these elements present to the corrosion potential of the alloy. However, numerous researchers [19, 26-29] have determined that this equation can be misleading when calculated from the bulk alloy composition because DSS alloys contain austenite and ferrite, which have different compositions. Ferrite is enriched in Cr and Mo, while austenite is enriched in N. In general, austenite has a lower PREN than ferrite in the base material, but austenite has higher PREN than ferrite in the weld metal.

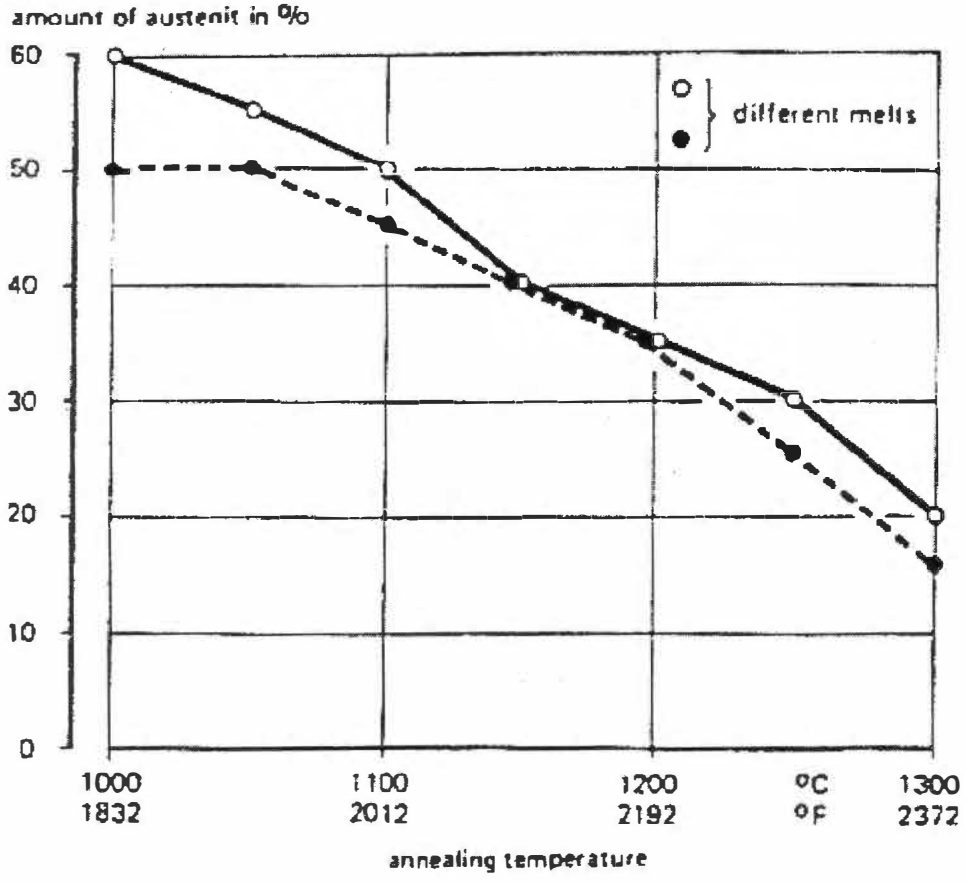


Figure 5. Effect of Solution Annealing Temperature on the Relative Amounts of the Ferrite and Austenite Phases [22]

However, Bernhardsson [29] showed by theoretical calculation, that an equal PREN for both austenite and ferrite can be achieved by adjusting the ferrite/austenite balance via adjusting Ni content and the heat treatment temperature. Tungsten was introduced as an active element with respect to pitting corrosion resistance and the following expression was proposed:

$$PRE_W = Cr + 3.3\ Mo + 1.15\ W + 16\ N \qquad \text{Equation 2 [1]}$$

The pitting resistance is a reflection of microstructural integrity, therefore to best achieve pitting corrosion resistance, the physical metallurgy and welding metallurgy of DSS must be understood. The following areas should always be addressed:

1) Ferrite/austenite balance: Cr_2N or other intermetallic phases can be caused by excess ferrite, whereas excess austenite will reduce the nitrogen concentration in the austenite and can cause greater segregation of Cr and Mo in the austenite [30].
2) Ni content control: High nickel content will result in excess austenite and the stabilization of sigma phase, whereas low nickel content will result in excess ferrite.
3) Proper selection of heat treatment temperature: Solution annealing temperature has a significant effect on the ferrite/austenite balance in DSS. A given nitrogen content needs a higher solution annealing temperature which in turn can cause excess ferrite.

4) Proper selection of welding procedures: Welding parameters, joint geometry, heat input, filler metal, and shielding/backing gases should always be carefully considered. Excessive dilution and extremely rapid or slow cooling rates must be avoided.

Intergranular Corrosion

If a DSS is properly solution annealed and cooled, which dissolves intermetallic compounds and chromium carbides, it is immune to intergranular corrosion [17, 31-35]. However, it was found that a high Mo content in oxidizing environments would result in higher general corrosion rates [36].

Phase balance plays a crucial role in the intergranular corrosion resistance of DSS. Gooch [30] showed that excess ferrite in weld HAZ's causes decreased resistance to intergranular corrosion. However, if enough austenite is formed along with the ferrite the HAZ is nearly immune to intergranular corrosion, therefore, microstructural control is again proven to be of great importance.

Toughness

The Charpy Impact test is a supplementary requirement for DSS castings specified to ASTM A890-4A. Druce et al. [118] determined that the V-notch specified by ASTM was the best geometry for the impact toughness testing of cast DSS.

This literature review mentions, in detail, the factors that can lead to reduced impact toughness in DSS, therefore, no further discussion of these factors will be included in this section of the review.

Welding of DSS

Welding Metallurgy

Farrar [40] noted that the transformation of delta-ferrite and the formation of intermetallic phases is controlled by the local microsegregation of chromium and molybdenum, not the bulk concentration. It was also shown by Farrar, that the delta-ferrite to austenite transformation is accompanied by significant diffusion of both Cr and Mo across the austenite/ferrite boundary to the delta-ferrite and that the enrichment strongly influences the formation of intermetallic phase.

Elemental partitioning of Cr, Mo, Ni, and N was studied by Atamart and King [41]. Mo was found to partition preferentially to ferrite as temperature decreased. With increasing temperature, the partitioning of Ni to austenite was determined to decrease gradually. It was also determined that N has the most profound effect on the austenite/ferrite phase balance. The volume fraction of austenite is extremely sensitive to small N additions, which suggests that the phase balance after welding can be controlled by the N content.

Similar studies by Ogawa and Koseki [27] showed that the microsegregation of Ni is more pronounced than Mo, which is more pronounced than that of Cr. The authors also noted that the partitioning of Cr, Mo, and Ni during ferrite solidification is not as

pronounced as during austenite segregation. Also, the partitioning of Cr, Mo, and Ni between austenite and ferrite was not significant. However, by increasing the austenite transformation temperature with the addition of Ni and/or N, partitioning was promoted.

Heat Affected Zone (HAZ)

The HAZ in welds experiences a range of thermal histories with peak temperatures reaching solidus adjacent to the weld and falling to ambient at greater distances from the weld. The total thermal cycle at a specific point in the HAZ is often very complicated to determine due to the rapid heating and cooling, and in multipass welds, the repeated exposure to high temperatures. The thermal history of the HAZ must be understood in order to identify potential metallurgical consequences in terms of austenite/ferrite phase balance, intermetallic phase precipitation, grain growth, and the HAZ width, which all effect mechanical properties and corrosion performance of DSS.

Austenite/ferrite phase balance control in the HAZ is important from a corrosion standpoint, in that the intergranular corrosion resistance, which is the major advantage of DSS over fully austenitic stainless steels, deteriorates with high ferrite contents. Also, austenite/ferrite content is important from a fracture toughness standpoint. As the ferrite content of DSS increases, impact toughness decreases. Therefore, proper balance of ferrite and austenite must be maintained.

For a given plate thickness, the cooling rate decreases as the heat input is increased. Also, for a given heat input, the cooling rate decreases as the plate thickness decreases. For these reasons, the welding heat input cannot be considered alone. However, for the

following discussion, the plate thickness and joint configuration is assumed to be the same.

Ferrite content in DSS is a function of heat input and cooling rate. The lower the heat input, the higher the ferrite content and the lower the impact toughness [42-53]. Draugelates et al. [48] explained that the higher cooling rates suppress the diffusion-controlled processes in austenite reformation, hence, the original phase ratio of ferrite to austenite is shifted towards higher ferrite content.

Secondary phase precipitation is also significantly effected by high cooling rates. Lippold et al. [51] ad Kirieva and Hanerz [52] explained that the presence of chromium-rich nitrides (Cr_2N) is observed over a wide range of cooling rates and the effect is particularly evident for microstructures with a high ferrite content (usually the result of a fast cooling rate). These chromium rich nitrides also significantly decrease the impact toughness and pitting corrosion resistance. A risk of chromium nitride formation in ferrite is also noticed with an increase in ferrite and increased nitrogen levels due to the lower solubility of nitrogen in ferrite. However, high cooling rates do reduce σ-phase and χ-phase precipitation.

It has been determined, however, that excessively high heat input may not be beneficial due to the risk of intermetallic phase precipitation and grain growth, both of which reduce impact toughness [40, 52-56].

Studies have also been conducted to compare the sensitivity with respect to cooling rate for different grades of DSS. As previously discussed, alloying elements, such as nickel and nitrogen, can increase the temperature range at which ferrite to austenite

transformation begins. Lippold et al. [51] investigated alloys SAF 2205, SAF 2507, and 52 N^+. Alloy 2507 was found to be less sensitive to HAZ microstructural degradation than Alloy 2205 over a wide range of cooling rates and heat inputs. It was suggested by the authors that the highly ferritic HAZ of Alloy 2507 is due to the greater temperature range between solidus and ferrite solvus temperature for Alloy 2205. Figure 6, from Lippold et al., shows the ferrite solvus temperature, A_4, is approximately 1180°C for Alloy 2205 and increases to approximately 1350°C for Alloy 2507 due to the higher content of nickel and nitrogen. Kivinera and Hanerz [52] showed that at a similar cooling rate, more ferrite was found in SAF 2205 HAZ than in SAF 2507 HAZ. Figure 7, illustrates these findings.

The effect of cooling rate on Alloy SAF 2205 and Ferralium 255 was compared by Lippold et al. For cooling rates from 2 C°/min. to 50 C°/min, the HAZ ferrite content for both alloys is nearly the same. Due to the chemistries of each alloy, this study showed that nickel and nitrogen are dominant elements in ferrite content control.

The effect of varying nitrogen content in super duplex stainless steel was investigated by Hoffmeister and Lothongkum [53]. It was determined that the A_4 temperature was increased and the ferrite to austenite transformation was accelerated as nitrogen content increased. However, a medium nitrogen content of approximately 0.10% was determined to be detrimental due to precipitation of Cr_2N when the cooling rate is high.

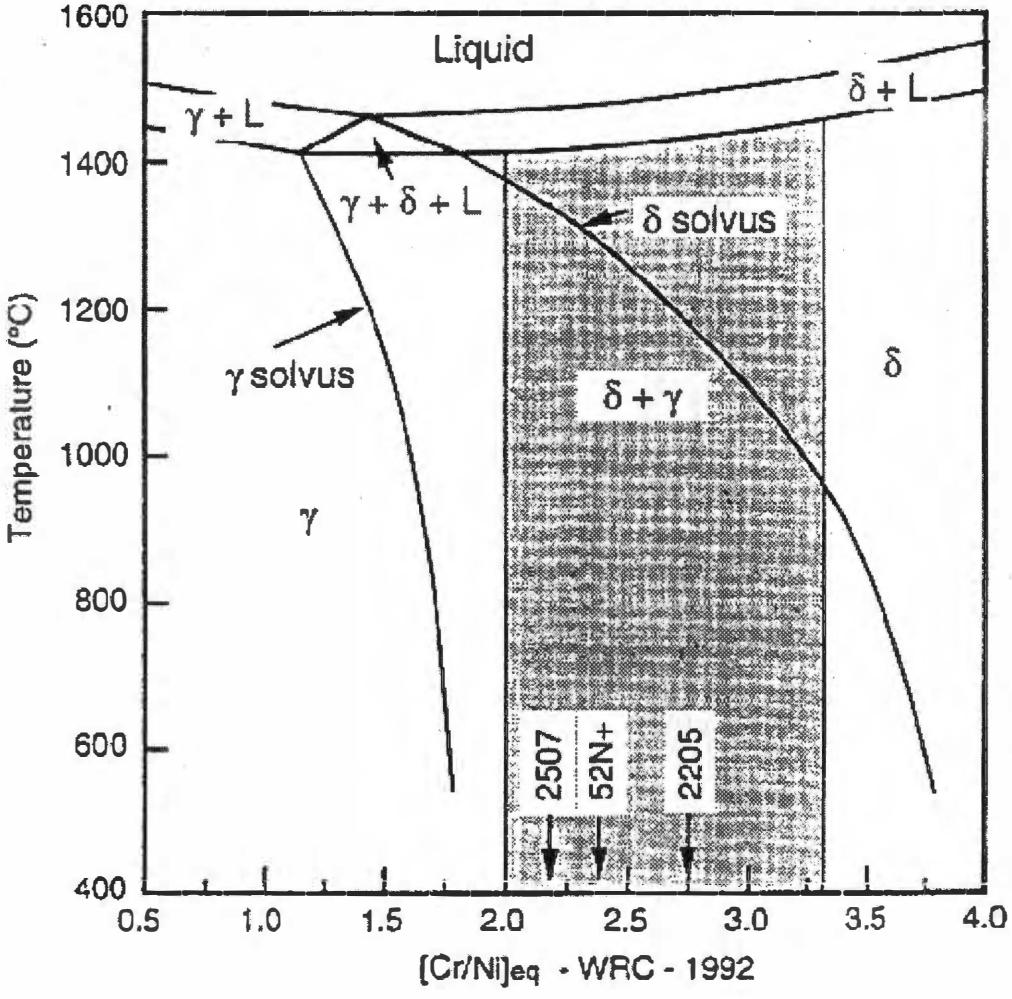
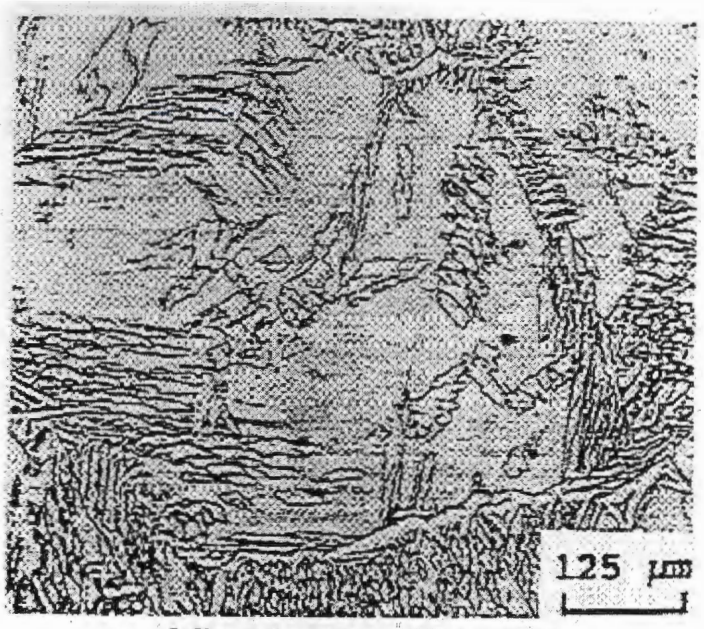
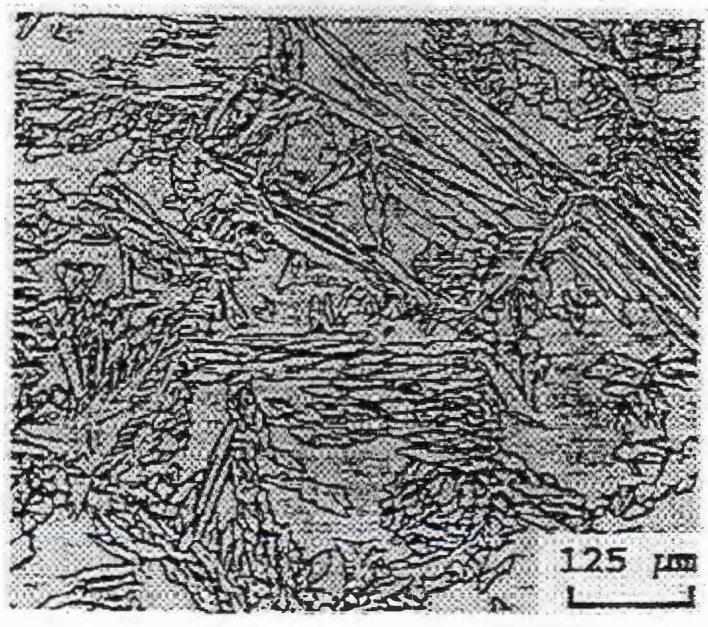


Figure 6. Modified Ternary Section of the Fe-Cr-Ni Phase Diagram Plotted Using the WRC-1992 Equivalent Relationships [51]



Microstructure of SAF 2205 after Gleeble simulation $\Delta t_{12/8}$ = 93.0 s



Microstructure of SAF 2507 after Gleeble simulation $\Delta t_{12/8}$ = 93.5 s

Figure 7. Micrographs Showing Microstructures of SAF 2205 and 2507 after Gleeble Simulation at Δt = 93.0 s [52]

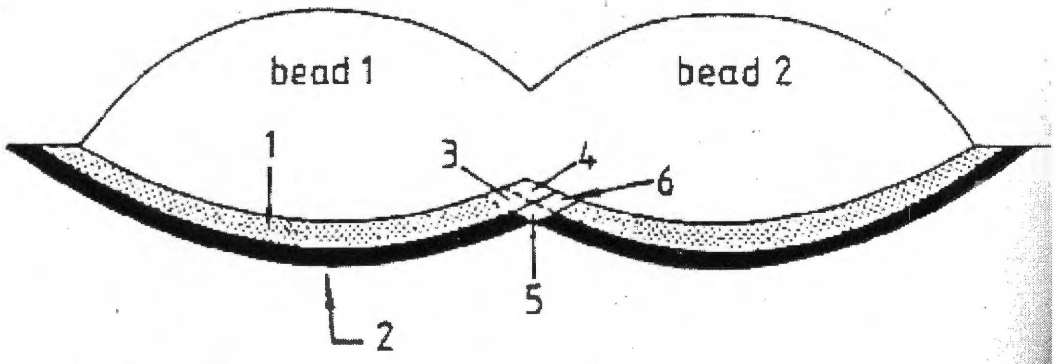
Generally, for a given cooling rate, the higher the peak temperature, the higher the ferrite content. Heating rate and base metal structure can also affect the final amount of ferrite. It was shown by Lippold et al [51] that fast heating rates can retard the dissolution of austenite therefore preventing a high ferrite content in the HAZ.

Grain growth can also be a problem in the HAZ. High peak temperatures may cause excessive grain growth, which can lower impact toughness [40, 52-56]. Atamert and King [42] showed that when the spacing between austenite particles is large, grain growth can be excessive.

The prior discussions of the HAZ are limited to single pass welding. However, it is important to consider multipass welding since it is normally used in industrial practice. During multipass welding the HAZ is reheated during subsequent weld passes, to a degree dependent on the position of the HAZ relative to the heat source. Figure 8 [42], shows the effect of multipass welding on the HAZ. Regions of the HAZ that are affected by the second pass may experience significant microstructural change.

In multipass welds , underlying weld metal is also reheated by the deposition of each subsequent pass. Figure 9 [57], shows another schematic of multipass effects on the HAZ.

A maximum interpass temperature of 150°C is normally recommended for multipass welding of DSS. [58,59]. However, Sandvik Steel [134] specifies a maximum interpass temperature of 150°C for SAF 2507 and 250°C for SAF 2304 and SAF 2205.



Region	First cycle	Second cycle
1	$T_{peak} > T_\delta$	...
2	$T_\tau < T_{peak} < T_\delta$	...
3	$T_{peak} > T_\delta$	$T_\tau < T_{peak} < T_\delta$
4	$T_{peak} > T_\delta$	$T_{peak} > T_\delta$
5	$T_\tau < T_{peak} < T_\delta$	$T_\tau < T_{peak} < T_\delta$
6	$T_\tau < T_{peak} < T_\delta$	$T_{peak} > T_\delta$

Figure 8. Schematic Showing HAZs Experience Different Thermal Cycles [42]

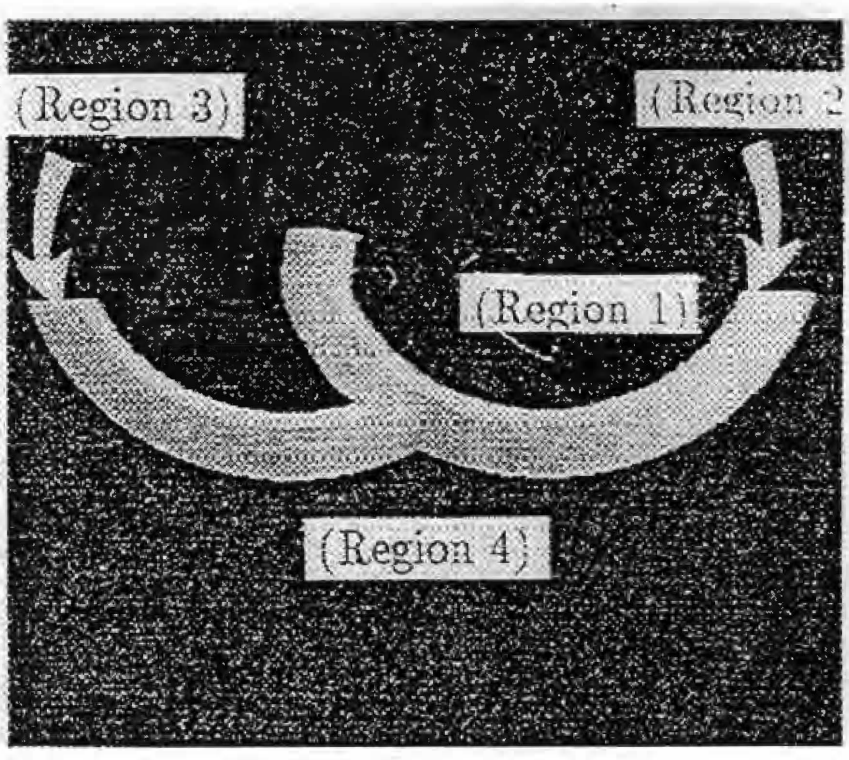


Figure 9. Schematic Diagram Illustrating the Relative Positions of the Different Thermal Cycles in a Two Pass Weld Deposit [57]

Region 1	Peak Temperature > T_S
Region 2	T_S > Peak Temperature > T_δ
Region 3	T_δ > Peak Temperature > T_F
Region 4	T_F > Peak Temperature

Where T_S = solidus temperature
T_δ = ferritization temperature
T_F = a temperature high enough to allow precipitation of austenite

Weld Fusion Zone

The weld fusion zone is similar to a casting in that segregation of alloying elements occurs. DSS weld metal solidifies mainly as ferrite, which leads to less segregation of chromium and molybdenum. Also, diffusion rates are at high temperatures just below the melting point, so homogenization of alloy elements in the ferrite can occur [30].

Heat input is of major concern when welding DSS. At low heat input, the ferrite/austenite transformation is controlled by nitrogen, so there may be little difference between the substitutional element contents of the two phases upon cooling to room temperature, although nitrogen will be enriched in the austenite. At high heat input, there is sufficient time for diffusion of Cr, Mo, and Ni to occur, therefore, there will be significant differences in the final alloy content between the two phases [30].

Autogenous welding of DSS is generally not recommended unless a post weld solution annealing heat treatment will be employed, due to the fact that a high ferrite content will produced and a brittle weld metal can exist [39]. DSS is generally welded with filler metals containing at least 2% higher nickel content than the base metal. However, if the filler metal composition is biased to austenite by adding nickel, an adverse weldment performance may result due to the following reasons:

1.) Increasing the nickel content promotes austenite formation and dilution of nitrogen content in the austenite and thus lowers the corrosion resistance of the austenite and the weld metal in general.

2.) High Ni promotes austenite formation but also promotes a greater concentration of ferrite stabilizing elements (Cr, Mo) in the remaining ferrite, therefore, more

susceptibility to the precipitation of sigma. Consequently, higher post weld solution heat treatment temperatures (1100 to 1150°C) must be utilized to dissolve all sigma phases [6].

3.) If the dilution from the parent steel is low, ferrite levels can be too low to even satisfy the weld metal strength requirements.

Ferrite Prediction and Measurement

It is essential for DSS to have appropriate ferrite content in order to achieve a desirable combination of strength, toughness, and corrosion resistance. Also, appropriate ferrite content helps to reduce the susceptibility of DSS to hot cracking and microfissuring. Excessively low levels of ferrite in DSS will cause low strength, poor intergranular corrosion resistance, and susceptibility to hot cracking. On the other hand, excessively high levels of ferrite in DSS will cause low toughness, poor intergranular and pitting corrosion resistance, and susceptibility to cold cracking embrittlement problems. From this, it is obvious that appropriate levels of ferrite must be maintained and accurate ferrite measurement techniques must be used in DSS castings and welds so that ferrite content can be achieved through chemical composition adjustment.

In 1949, Schaeffler [65] began some of the earliest work on ferrite prediction in weld metals. Delong [66] expanded on this work, as did Kotecki [62-64], who also accomplished significant research on ferrite measurement.

The Schaeffler diagram, Figure 10, first developed in 1949, contains phase fields and isoferrite lines that predict weld metal structure as a function of composition.

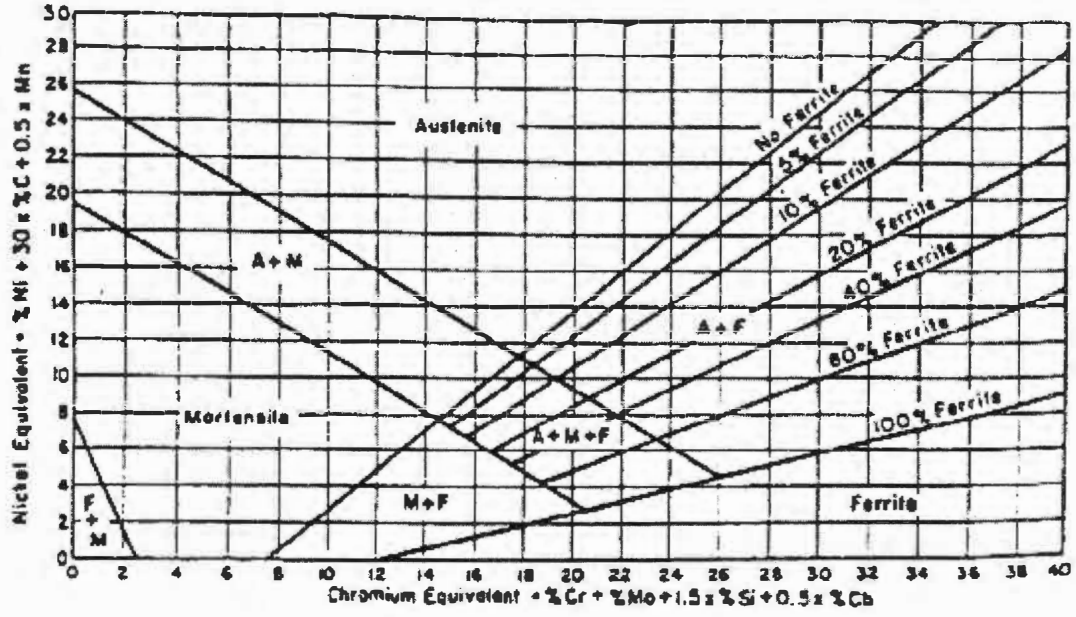


Figure 10. The Schaeffler's Diagram [65]

A "chromium equivalent" (Cr_{eq}) and a "nickel equivalent" (Ni_{eq}) are calculated for each base metal and filler metal. The equivalents are then plotted on the Schaeffler diagram and tie lines are drawn through the plotted points, proportioned according to expected dilution, to obtain a weld metal ferrite content estimation.

Based on the Schaeffler diagram, the WRC-1992 diagram was developed. Due to the fact that the Schaeffler diagram was replaced by the WRC-1992 diagram in codes such as ASME Boiler and Pressure Vessel Code [86], this review focuses on the WRC-1992 diagram and the on-going debate over possible modifications. Also, the Schoefer diagram, which was developed similarly to the Schaeffler diagram, has been a standard for stainless steel castings and will also be addressed in this review.

WRC-1992 Diagram

Figure 11, shows the WRC-1992 diagram. Cr_{eq} and Ni_{eq} for the WRC-1992 diagram are calculated as:

$$Cr_{eq} = Cr + Mo + 0.7\ Nb \qquad \text{Equation 3}$$

$$Ni_{eq} = Ni + 35\ C + 20\ N + 0.25\ Cu \qquad \text{Equation 4}$$

The significant addition in developing the WRC-1992 diagram was the recognition that a coefficient of Cu needed to be added to the Ni_{eq}. Kotecki [62] stated that the importance of the effect of Cu on ferrite content has long been recognized and various coefficients have been proposed. Lake [67] developed data specifically for evaluation of the effect of Cu. The data was developed by determining the effect of Cu through the

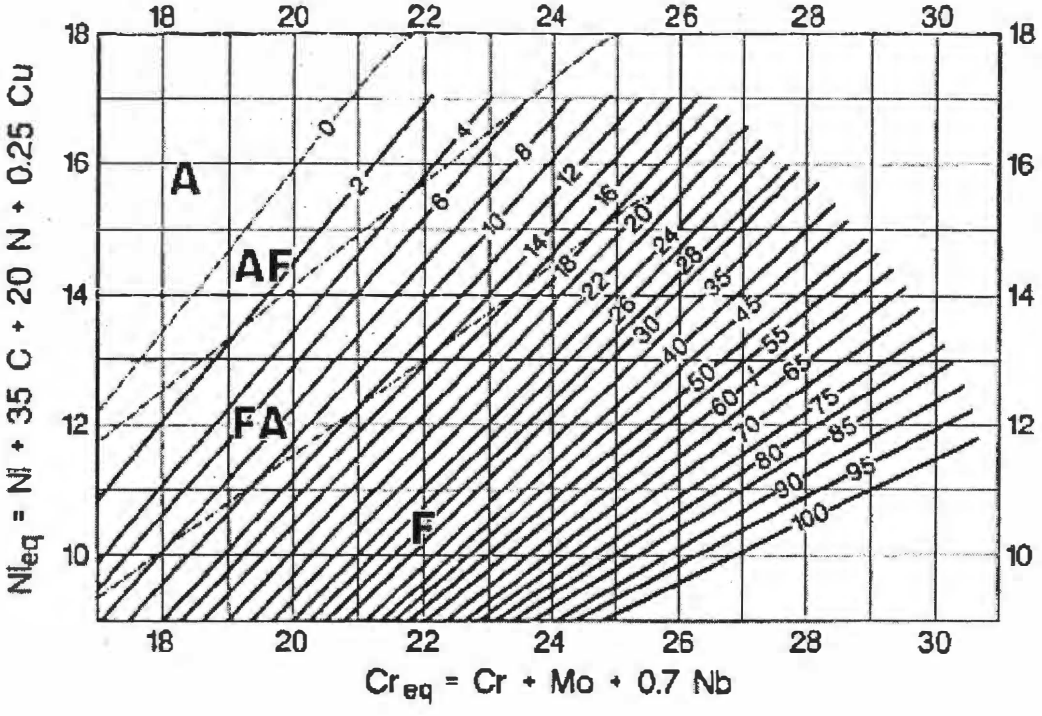


Figure 11. The WRC-1992 Diagram [62]

addition of 0 – 4% Cu. Building on Lake's research, Kotecki [68] proposed a coefficient of 0.25 for Cu and demonstrated the validity. Kotecki [62] also noted that the predictions of the WRC-1992 diagram are only valid over limited Cr_{eq} and Ni_{eq} ranges, 17-31 and 9-8, respectively. However demonstrations were made that proved lower ranges of Cr_{eq} and Ni_{eq} could be valid.

The Schoeffer Diagram

Figure 12 shows the Schoeffer diagram, which was adopted by ASTM and used in Specification A 800. As with similar diagrams, the Schoeffer diagram requires that Cr_{eq} and Ni_{eq} be calculated but the calculations for the Schoeffer diagram are vastly different than calculations for other diagrams. The calculation for Cr_{eq} and Ni_{eq} are shown below:

$$Cr_{eq} = Cr + 1.5\ Si + 1.4\ Mo + Nb - 4.99 \qquad \text{Equation 5}$$

$$Ni_{eq} = Ni + 30\ C + 0.5\ Mn + 26\ (N-0.02) + 2.77 \qquad \text{Equation 6}$$

where the elemental concentrations are given in weight percent.

It must be noted that the WRC-1992 diagram bases ferrite content in Ferrite Number (FN), which is based on magnetic response. In the Schoeffer diagram, the ferrite content is based on volume fraction. A comparison between FN and ferrite percent will be addressed later in this review.

ASTM A 800-91 states that the Schoeffer diagram is applicable to alloys containing elements in the following ranges:

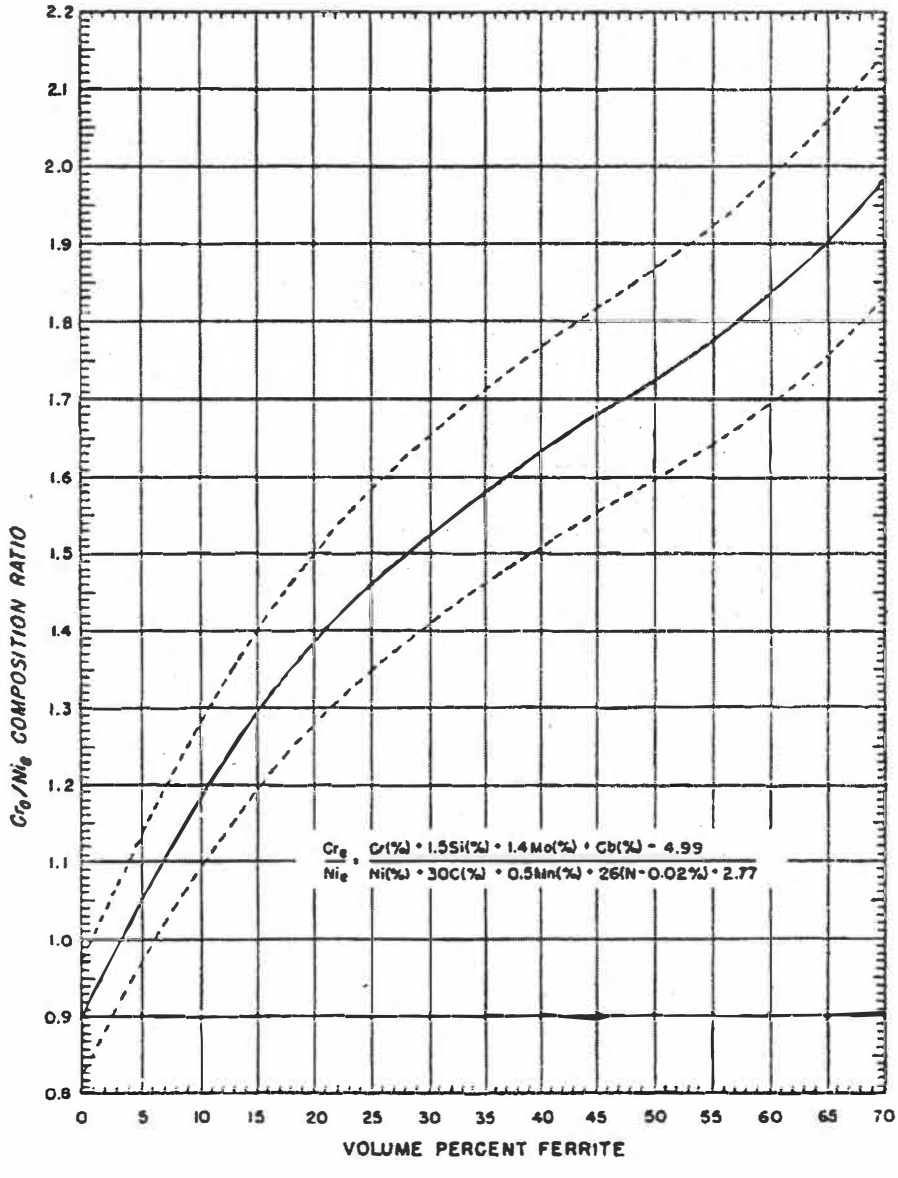


Figure 12. The Schoeffer Diagram (from ASTM A 800-91)

Carbon	0.20 max
Manganese	2.00 max
Silicon	2.00 max
Chromium	17.0 – 28.0
Nickel	4.0 – 13.0
Molybdenum	4.00 max
Columbium	1.00 max
Nitrogen	0.20 max

By examining the elemental content of DSS, nitrogen, which is a strong austenite former and Mo, which is a strong ferrite promoter, can easily exceed the Schoeffer diagram elemental limitations, which produces concerns for the accuracy of estimations produced by this method for DSS ferrite prediction. However, presently there are no alternate "quick" methods for ferrite prediction in DSS.

Ferrite Measurement

Discussions on ferrite prediction have shown that no one method is completely accurate for DSS. Therefore, it is imperative that accurate ferrite measurement techniques be established in order to ensure that an appropriate balance of ferrite and austenite in DSS castings and weld metal is achieved.

The following sections will address advantages and disadvantages of the current ferrite measurement techniques that have been established, with some being standardized and others not.

Point Count

ASTM E562, a standard method for point counting has long been the traditional method for the determination of ferrite content in DSS castings and weld metal. This test method involves the preparation of a specimen to a metallographic finish, selecting a proper magnification and grid, and manually counting ferrite that lies on the intersection of grid lines. Disadvantages of this method have been recognized and are summarized below:

1) Destructive: Samples must be cut from the part in order to conduct the point counting evaluation.
2) Time Consuming: Preparation of test samples and counting of phases can take a considerable amount of time.
3) May Be Inaccurate: Errors can occur due to operator bias, improper grid selection, and a non-homogeneous amount of phase to be counted. In addition, for DSS weld metal, ferrite morphologies can be fine and irregular [93,94], which causes difficulty in accurate point counting.

Etching solutions to be used are dependent upon the actual phase that is going to be counted. In ferrite point counting in DSS, 40% NaOH etching solution is recommended, which stains ferrite dark and austenite light.

Magne-Gage: Magnetic Adhesion Method

The ferromagnetic property of ferrite has been used in many instruments, to determine the ferrite content in DSS castings and weld metal. The Magne-Gage is one of the most widely applied instruments, which uses the ferromagnetic property of ferrite to make measurements.

Figure 13 [69] shows a standard version of the Magne-Gage. The white dial (WD) scale measures the range of 0-28 FN with a #3 magnet. The white dial readings decrease as the FN increases, therefore 0 FN usually corresponds to a WD greater than 100. The range in measurement of 0-28 F for the Magne-Gage is certainly a major limitation, but this problem can be solved using the Extended ferrite Number (EFN) system.

It is imperative to recognize the advantages of using FN in place of volume % ferrite. The arbitrary FN scale was first adopted in the U.S. as ASI/AWS A4.2-74 [70]. FN has been found to be very reproducible, which is the main advantage for its use and standardization. However, FN has been found to appreciable overstate the volume % ferrite in weld metal [70].

Calibration of the Magne-Gage must be performed in order to accurately develop the EFN as a function of WD. Primary and secondary standards are specified, in ANSI/AWS A4.2-91 [71] ad ASTM A 799-92, for the calibration. Primary standards are available from the U.S. National Institute of Standards and Technology (NIST), formerly known as the National Bureau of Standards (NBS), and consist of a non-magnetic coating over a carbon steel substrate. Secondary standards are cast stainless steel or DSS weld metals whose ferrite percent has been determined "in house" by a primary instrument. Detailed

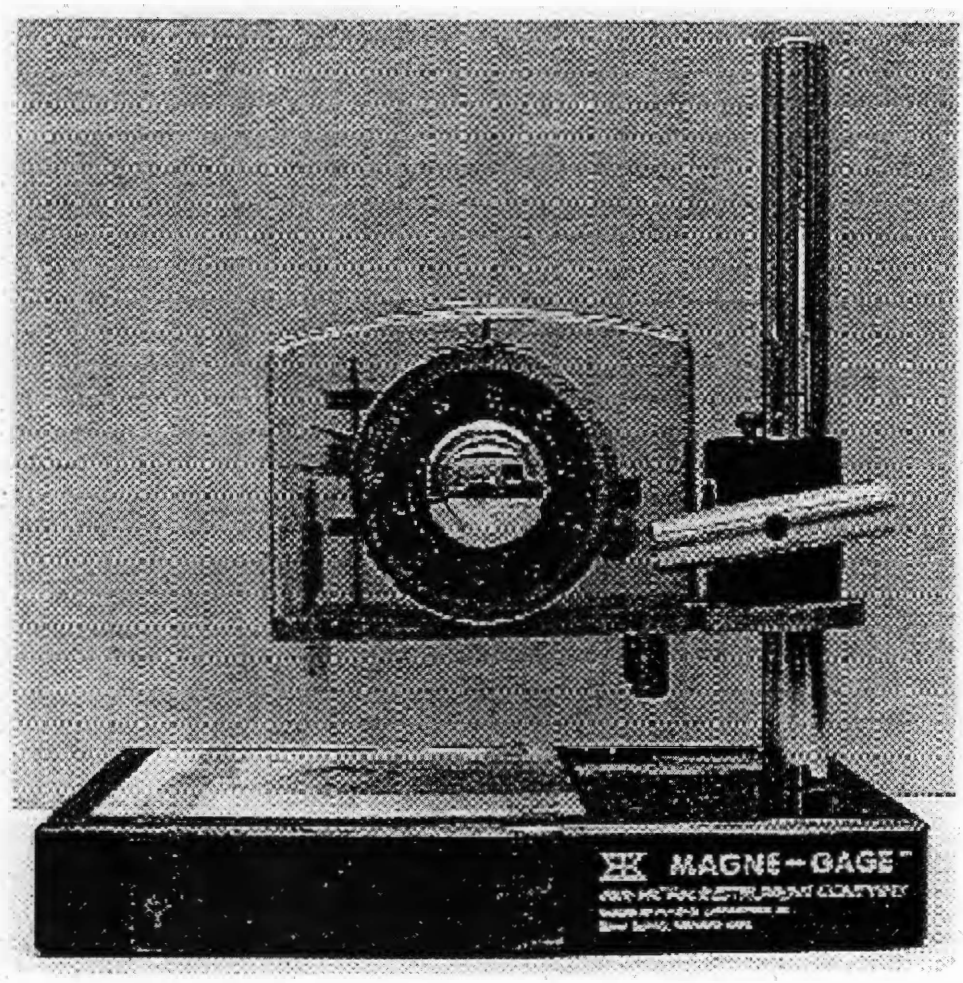


Figure 13. Photograph of a Standard Magne-Gage

calibration procedures are described in ANSI/AWS A4.2-91 and ASTM A 799-92. Readers are referred to Kotecki [86,88,96] for details on the lengthy procedures for developing EFN as a function of WD.

Measurements taken from the Magne-Gage are very reproducible, however, the Magne-gage is not well suited for field use. Also, the Magne-Gage is not well suited for measuring ferrite content of specimens with smaller contact surfaces than the contact surface of the magnet used in the gage.

Eddy Current Method: Magnetic Induction Method

Instrumentation for the eddy current method usually includes a display and control unit and a hand-held eddy current probe, which makes this method particularly well suited for field measurements of ferrite content.

Figure 14, shows a schematic of the magnetic induction measurement method. The method utilizes a low frequency alternating current through the field coil, generating an alternating magnetic field that penetrates the specimen. The interaction between the field and specimen produces an alternating voltage in the detection coil that is proportional to the ferrite content in the volume of the measurement, which means this method determines ferrite in terms of volume %.

The Feritscope® is a commercially available instrument that incorporates this measurement technique. The accuracy of the Feritscope® is affected by the electromagnetic properties of the ferrite and morphology of the ferrite [72].

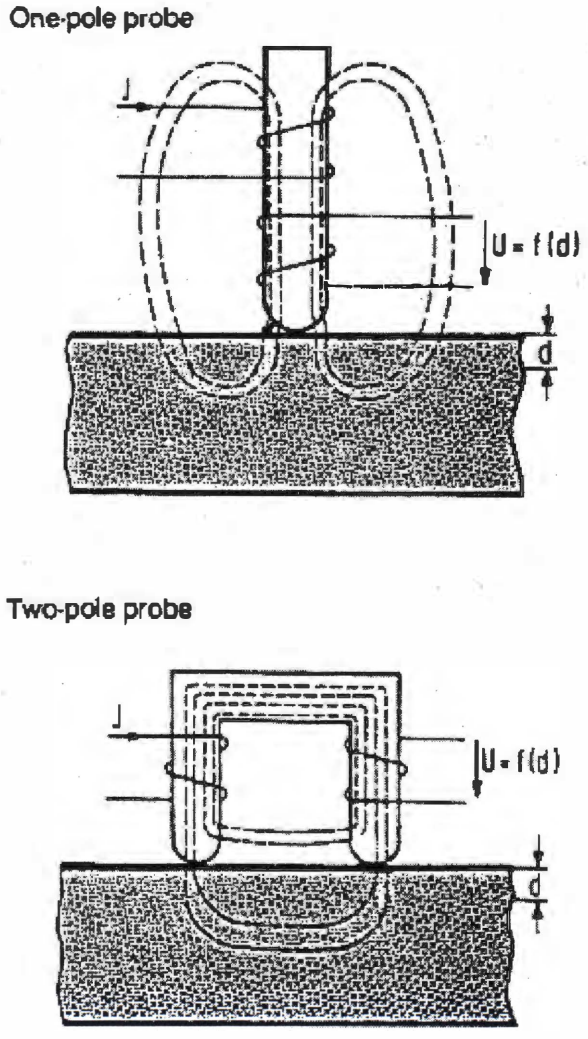


Figure 14. Schematic of the Magnetic Induction Method

Distance between the probe and the surface of the specimen and the curvature of the specimen can also affect the accuracy.

Ferrite Number vs. Ferrite Percent

Point Counting and the Feritscope® measure ferrite content in ferrite %, whereas the Magne-Gage measures ferrite content in FN. There is not a simple relationship between FN and ferrite % mainly because the relationship depends upon the composition of the ferrite [73]. FN is clearly preferable to ferrite % for the determination of ferrite in duplex stainless steel weld metal [74]. However, Kotecki [73] indicated that such is not the case with cast alloy, in which the ferrite is much coarser and more regularly shaped than in the weld metal. Taylor [75] suggested a relationship between FN and ferrite %:

$$\% \text{ Ferrite} = 0.55(\text{Extended Ferrite Number}) + 10.6 \qquad \text{Equation 7}$$

Since EFN is used in this equation, FN in the range of 0-28 is not applicable for this equation.

Weldability

Weldability defines the ease of producing a defect-free weld with adequate mechanical properties and corrosion resistance. Hot cracks in the fusion zone or HAZ and hydrogen assisted cold cracking are the defects of interest in DSS. The following

sections will address proper welding procedures, to avoid these types of defects and to achieve adequate mechanical properties and corrosion resistance.

Fusion Zone Solidification Cracking

Weld solidification cracking is caused by a crack-susceptible microstructure which forms at the final stage of the solidification process due to the low melting impurities enriched in the final liquid films. A Cr_{eq}/Ni_{eq} ratio of less than 1.5 causes DSS welds to solidify in a primary austenite mode causing severe partitioning of impurities such as S and P, which form liquid films which can wet austenite/austenite grain boundaries and lead to solidification cracking. A Cr_{eq}/Ni_{eq} ratio of 1.5 – 2.0 has been determined as the optimum level for resistance to hot cracking in DSS. A Cr_{eq}/Ni_{eq} ratio above 2.0 has been shown to have a highly ferritic solidification, which also produces cracking tendencies.

Little research on DSS fusion zone solidification cracking exists. Fabrication experience with a number of commercial DSS has suggested that weld solidification cracking is not a significant problem [76]. DSS alloys solidify with ferrite as the primary phase, which causes these alloys to be less susceptible to solidification cracking than those that solidify with austenite as the primary phase. The difference in cracking susceptibility as a function of primary solidification product is generally ascribed to the greater affinity of the ferrite phase for the impurity elements such as sulfur and phosphorus and the reduced tendency for liquid films to wet ferrite/ferrite boundaries [99].

Heat Affected Zone Liquation Cracking

Lippold et al. [77] concluded that the susceptibility of DSS to liquation-related HAZ cracking is negligible. It was noted that ferritic microstructures are generally resistant to grain boundary liquation because of the high diffusivity of impurities at high temperatures and because DSS generally contain low amounts of impurities.

Hydrogen Assisted Cold Cracking

Cold cracking, also known as hydrogen assisted cracking, susceptibility is determined by three factors: susceptible microstructure, the presence of hydrogen, and restraint. Although ferrite in DSS helps to eliminate hot cracking problems, it increases the risk of cold cracking.

Highly ferritic microstructures are considered susceptible because they have high strength, low toughness, and high diffusivity for hydrogen.

Hydrogen can be introduced into welds in many ways but most commonly through the use of electrodes that have absorbed moisture or from the atmosphere, which is not properly shielded during welding. Ar-5% H_2 has been used as a common shielding gas when joining DSS using the gas tungsten arc welding process [59, 61, , 78-84]. Research [78-84] has shown that cold cracking susceptibility of DSS increases as ferrite content increases; therefore, it is necessary to have a properly controlled ferrite/austenite balance.

The work of Ogawa and Miura [79] showed that by increasing austenite formation, by increasing the N_2 and Ni content, cold cracking problems will be reduced. The reason for this is that the diffusivity of hydrogen in austenite is significantly lower than in ferrite.

Therefore, for a given hydrogen level in the weld, the lower the amount of ferrite, the lower the tendency for cold cracking. Hoffmeister et al. [81] showed that an interaction between nitrogen and hydrogen occurs during welding. When welding DSS containing N_2, the loss of N_2 is more severe when H_2 bearing Ar is used. For this reason, Hoffmeister et al. suggested that H_2 needs to be mixed with Ar, N_2 should also be mixed, mainly because N_2 and H_2 loss in the weld metal is reduced. Shinozaki et al. [78], warned that adding Nitrogen may not be beneficial depending on whether nitrogen is indeed dissolved in austenite. If this happens, the higher nitrogen content causes a higher amount of Cr_2N precipitation, which can increase the risk of cold cracking. Preheating the material at 100 – 200°C is viable to decrease the cooling rate [79].

Postweld solution heat treatment immediately after welding is another suggested method for eliminating hydrogen cracking [79]. However, section size limitations and material chemistry may make preheating or postweld heat treatment difficult. Therefore, the most viable option for eliminating cold cracking is the elimination of H_2 from the welding process.

Readers interested in cold cracking susceptibility tests are referred to Shinozaki et al. [78], Ogawa and Miura [79], Lundin et al. [84], and Walker and Gooch [85].

Welding Procedures

Good welding practice must be appreciated and implemented when fabricating DSS. The details of, for example, the welding energy input must be related to the grade and thickness being welded [121]. Welding procedures must be correctly designed as an aid

to the welder, not simply as a document for the owner and authorities [121]. Balanced welding and distortion control techniques have positive implications on the technical and economic success of duplex fabrication [121].

Welding Processes

The following welding process have been determined as viable methods for DSS [86-94]:

1) SMAW Shielded Metal Arc Welding (stick electrode welding)
2) GTAW Gas Tungsten Arc Welding
3) GMAW Gas Metal Arc Welding
4) FCAW Flux Cored Arc Welding
5) SAW Submerged Arc Welding
6) PAW Plasma Arc Welding

Table 4 gives a brief summary of the characteristics of the welding processes listed above. Resistance welding (RW), laser welding (LW), electron beam welding (EBW) and friction welding (FW) are considered immature processes for DSS [94].
These processes are considered immature due to the fact that rapid cooling rates are generally produced, which often leads to high ferrite content in DSS weld metals and HAZ. Similarly, electroslag welding (ESW) is not recommended because it requires high

Table 4. Welding Process Characteristics (From Nassau et al. [86])

Welding Process	Characteristics
SMAW	Readily available, all positions, slag on weld to be removed, low deposition rate
GTAW	Requires good skill, most suitable for pipe welding, high effect of dilution in root runs, low deposition rate, can be mechanized/automated
GMAW	Requires good skill, more setup work, metal transfer depends on wire quality (spattering), commonly only for filling of joint, high deposition rate, can be automated
FCAW	Limited availability of consumables, only for filling of joint, limited positional welding, high deposition rate, slag protection
SAW	Only mechanized, required set-up arrangements, only downhand (flat) welding, high dilution affects weld properties, higher deposition rate, slag removal in joint may be difficult
PAW	Requires complex equipment, only mechanized welding, no filler metal added, plate composition determines weld properties, high welding speed

heat inputs and can produce extremely slow cooling rates, which can lead to intermetallic phase precipitation in DSS.

SMAW and GTAW are the most used processes for the welding of DSS, therefore the focus of this review will be these processes.

SMAW

Table 4 shows that SMAW is a versatile welding process, which can be used in all welding positions. For the repair welding of castings and other structures, SMAW is usually selected [86]. Basic SMAW electrodes usually result in poor cosmetic appearance of the weld and difficulty in removing slag, therefore rutile coated electrodes are normally the electrode of choice. However, basic electrodes show good low temperature impact values because of their lower oxygen and silicon content deposited in the weld.

The control of moisture is important to eliminate cold cracking problems and porosity [87, 89, 91, 95]. A method for moisture control in SMAW electrodes is to bake for approximately two hours at 250 – 305°C before welding. Extra-moisture-resistant (EMR) electrodes, which have a manufacturer's guarantee of low moisture content, are also an excellent option for control of cold cracking.

SMAW relies on gases and slag from the electrode to protect the pool during welding. Holmberg [91] recommended that an arc as short as possible should be maintained in order to offer the best protection of the weld pool. Oxides, porosity,

reduced mechanical properties, and excessive heat input can be produced if the arc is long.

Heat input in DSS welding is of major importance. Low heat inputs result in fast cooling rates causing high ferrite content and Cr_2N precipitates, which in turn, causes brittleness in the weld. High heat inputs result in slow cooling rates, which can lead to the precipitation of detrimental intermetallic phases in DSS. A range of heat inputs for a broad range of thicknesses was recommended by Holmberg [91], 0.2 –1.5 KJ/mm for alloy SAF 2507 and 0.5 – 2.5 KJ/mm for 22Cr DSS. Readers are encouraged to consult the material producers for detailed welding parameter information.

GTAW

GTAW is a slow process but it can be ideal for certain welding situations. GTAW is the process of choice for high-quality root passes in piping because, with proper backing, it prevents slag, spatter, and oxidation on the inside root pass. Also, automated GTAW shows great weld to weld repeatability.

Figure 15 shows the impact toughness characteristics of GTAW as opposed to various other welding processes. GTAW exhibits better impact toughness because of the absence of slag and oxidation.

Root pass dilution can be severe in GTAW therefore filler metal must be added to control this phenomenon. Autogenous GTAW is generally not recommended unless a PWHT is to be performed [87, 89, 91].

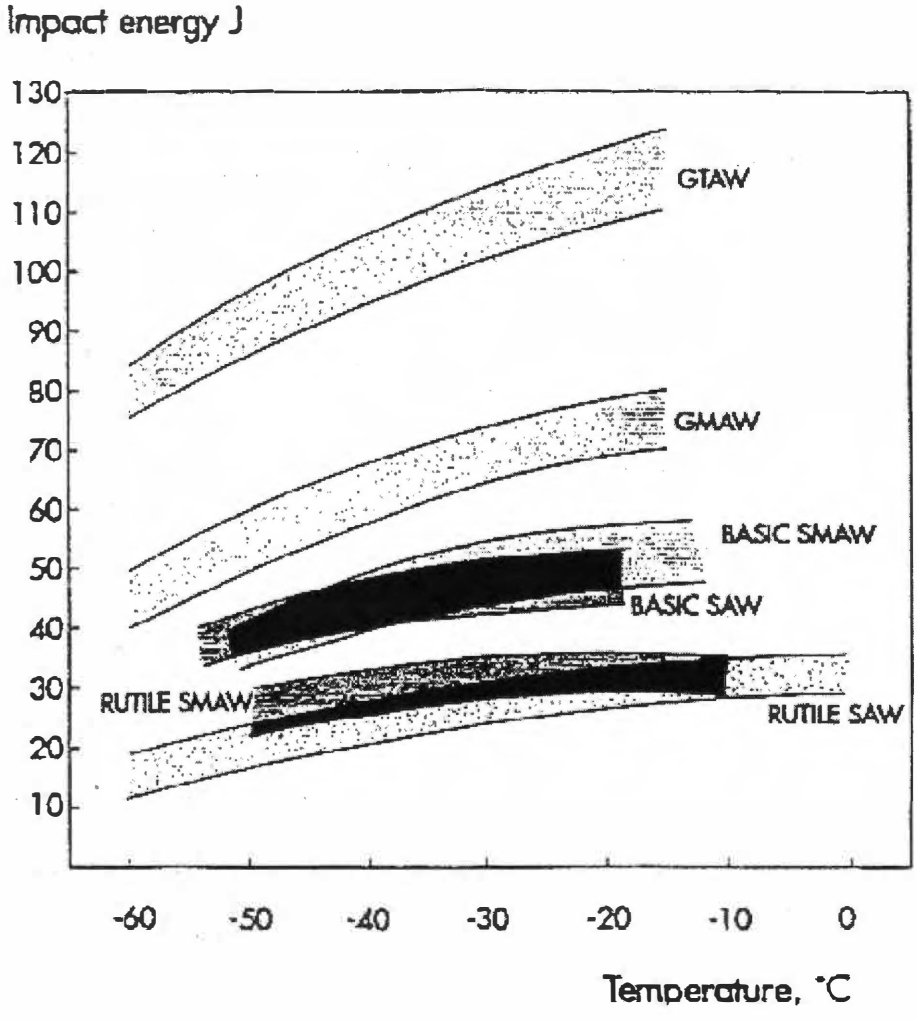


Figure 15. Effect of Welding Process on Impact Toughness (From Noble and Gunn [88])

Nitrogen is known to promote austenite formation in DSS and a loss of nitrogen can lead to high ferrite content. GTAW is known to be susceptible to nitrogen dilution, therefore N_2 addition to the shielding gas is generally recommended. A common shielding gas used in GTAW is the addition of 5% N_2 into Ar. 100% N_2 backing gas is recommended for welding the root pas [11]. Shielding and backing gas will be discussed, in greater detail, later in this review.

GTAW heat input ranges are similar to SMAW therefore refer to recommended ranges for SMAW.

Other Welding Processes

The major concern for using GMAW and FCAW is to have proper shielding gas [96] or flux so that oxygen in the weld metal is kept to a minimum. Dilution is a major concern for SAW and PAW. SAW dilution can be controlled through proper weld preparation and heat input [98] and proper control of interpass temperature. PAW should employ nickel-based filler metal along with a postweld heat treatment. Stringer beads should be used for these processes for accurate control of the heat input.

Filler Metal

The selection of a proper filler metal is critical in the welding of DSS in order to achieve the desired ferrite balance. The use of a matching filler metal does not work well with DSS unless a postweld solution anneal is employed to restore the chemistry balance that is upset by the dilution effect [75, 100]. Overmatching consumables are now

considered to be a viable option, which can give improved mechanical properties and corrosion resistance provided the correct welding procedures and heat treatments are applied [122].

Overmatched filler metals are generally the rule of thumb for DSS welding. Weld metal ferrite contents show very modest reductions after solution annealing, there is no evidence to support the concern that has been sometimes expressed that overmatching weld metals would contain insufficient ferrite [122]. The filler metal chemistry is modified to provide comparable mechanical properties and improved corrosion resistance to allow for the loss of particular elements in the arc [75]. For this reason, DSS filler metals normally contain nitrogen and have high levels of nickel. N_2 is added to control ferrite content and increase pitting corrosion resistance, while Ni is added for ferrite content control only.

Covered electrodes high in silicon, such as rutile electrodes, also produce high oxygen content in the weld metal. It has been documented that weld metal toughness is affected by ferrite content and oxygen content, therefore basic covered electrodes may produce better properties due to the lower silicon and oxygen levels they contain [100].

Increased corrosion resistance can be achieved through the use of Ni-base filler metals. However, Holmberg [100] concluded that the combination of Ni-base fillers in the root and duplex fillers in the intermediate passes and cap passes may result in brittle microstructures. It was concluded by Ödegärd and Fager [101], that welding super DSS using high Ni filler metal produced Cr_2N in the reheated regions and resulted in lower toughness. Electrode OK 92.95, was recommended by Karlsson et al. [101], to solve

these problems. It was shown that weld metal deposited with electrode OK 92.95 has an impact toughness value of > 50 J at 196°C.

The development of welding filler electrodes and wires for DSS has been rapid but the standardization of welding consumables is limited [86]. It was stated, by van Nassau et al. [86], that covered electrodes can only be made to the following drafts of national and international standards or working documents:

1) AWS A 5.4-92
2) AWS A 5.9-93
3) CEN (TC121 PREN...)
4) IIW (Subcommittee IIE. Doc. II-E-118-91)

Shielding and Backing Gases

The role of welding gases in the fabrication of DSS has been of interest, especially for GTAW [102-106]. Pitting corrosion resistance, for welds made with nitrogen additions in shielding and backing gases, has been shown to significantly improve over normal pure argon shielding and backing gases. The effect of various shielding gases on critical pitting resistance (CPT) of DSS is shown in Figure 16 [102]. While backing gases are encouraged to be 100% N_2 [102-106], the nitrogen content in shielding gas has been limited to a maximum of 5% due to weldability problems. More than 5% N_2 can cause detrimental effects on the weldability of DSS, namely, tungsten electrode contamination, unstable arc conditions, weld pool turbulence, spatter, and weld metal porosity. Helium and hydrogen can also be added to argon in shielding gas, the additions

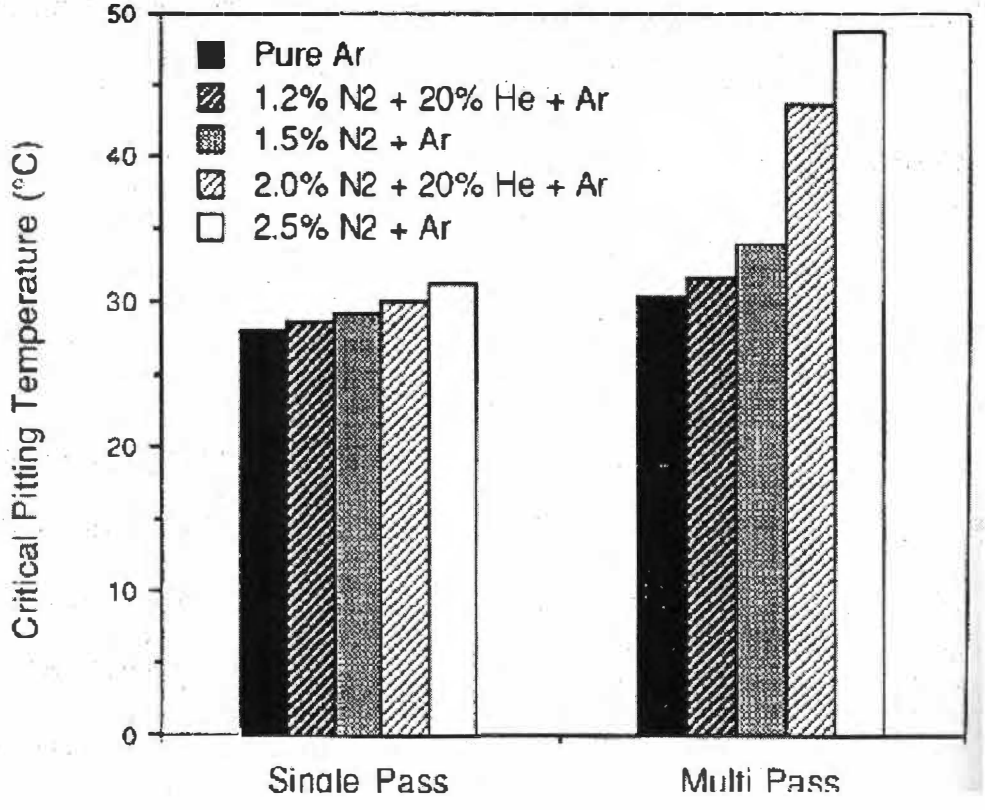


Figure 16. Effect of Shielding Gas Compositions on Pitting Corrosion Resistance of Duplex Stainless Steels (From Urmston et al. [102])

can lead to better weld penetration. However, as stated before, the addition of hydrogen can lead to cold cracking if ferrite levels are not controlled. Also, H_2 enhances nitrogen loss in the weld pool [81].

Shielding and backing gases in GMAW also require special attention when welding DSS [107-108]. Carbon dioxide and oxygen are additions commonly used to stabilize the arc. However, oxygen has been shown to lower weld metal toughness for DSS. Stenbacka et al. [107] concluded that standard gases such as Ar + 2 vol.% O_2 and Ar + 2 vol.% CO_2 are not suitable for GMAW of 2205 and 2507 DSS. Arcal 129 (Ar, 5% He, 2% CO_2 and 2% N_2) has been shown to produce good results and has not shown carbon pickup [108].

Other Welding Related Issues

The welding of DSS is a complex issue due to the fact that small variations in heat input may cause microstructural variation, which can cause changes in mechanical properties and corrosion resistance that cannot be defined by normal non-destructive tests [109-110]. A lack of specifications for DSS was pointed out by Warburton et al [110], it is suggested that Charpy impact tests, corrosion tests per ASTM G48, and microstructural examinations be conducted.

Energy input control is appropriate, the energy level and extent of control must be related to the alloy being welded and to the section thickness [123]. Fusari and Bertoni [109] stress the importance of informing personnel involved in DSS fabrication that

welding procedures must be followed. For example, an arc strike by the operator can cause very rapid cooling, which will produce localized microstructural problems [134].

Improper joint design has been shown to cause severe dilution, which can affect ferrite content and toughness, along with corrosion resistance [90]. As a general rule, the root gap and joint angle for DSS should be wider than for austenitic stainless steel [134]. For more information, readers should refer to manufacturer's guidelines and references for welding [95, 112-116, 134].

Cleaning of DSS joints before and after welding should follow the same practices documented for austenitic stainless steel. Use of a rotating brush for cleaning should be avoided because it may cause micro-crevices and decrease the corrosion resistance [134].

Casting Related Issues

There are a number of differences, listed by Niederau and Overbeck [119], between cast DSS and wrought DSS:

1.) The grain size in the casting is coarser than in a mechanically deformed wrought structure. Microsegregation, due to processing differences, is also well pronounced in the cast structure with attendant differences in corrosion behavior.

2.) It is more difficult to avoid the formation of intermetallic phases in castings as opposed to wrought products because castings may have a larger section size, which produces slower cooling rates in the center of the section.

3.) Nitrogen solubility in castings may be limited. Nitrogen amounts in excess of 0.28% can cause gas defects in the castings [75].

Casting Production

DSS is usually melted in electric arc of induction furnaces [75]. Control of the chemistry is of major importance during the production of DSS. Argon-Oxygen-Decarburization (AOD) refining is highly recommended [11]. Titanium, Zirconium , and aluminum have a strong affinity for nitrogen, for this reason, these elements should not be employed in deoxidation processes [75].

DSS is produced in both static and centrifugally casting [75]. Pouring temperature must be controlled to minimize grain size but the final decision on temperature depends on mold complexity and section size [120]. Casting technology and method design of cast components imposes that the primary grain size is already fixed after the end of solidification. Consequently, a grain refinement treatment or inoculation is for the foundry is of great interest [124]. It is known that the yield and ultimate tensile strengths increase with decreasing grain size according to the Hall-Petch relation [124]. Whenever possible a solution treatment after shakeout should be employed [75]. This treatment reduces the likelihood for cracking during subsequent processing [11].

IV. Experimental Procedures

ASTM E562 Ferrite Measurement Round Robin Study

Materials

A sample set of 5 samples was extracted from cast austenitic and DSS in order to have varying amounts of ferrite to be measured. Table 5correlates the sample code with the alloy type. Figures 17-21 show the microstructure of each of the samples.

Testing Method

Each sample was prepared on the measurement face by metallographic polishing and etching. The metallography was performed by UT to ensure that each participant received suitably polished and etched samples and to eliminate bias. Figures 17-21 show the microstructure of each sample used in the study, the darker phase is ferrite and the lighter phase is austenite. A circle was scribed on the measurement face and no measurements were to be taken outside of the cycle. This was to ensure that all participants measured the same areas on the samples.

Table 5. Round Robin Sample Set

Code	Alloy Type
A	CF8
E	ASTM A890-4A
F	ASTM A890-4A*
J	CD7MCuN*
K	CD7MCuN

* Indicates that the material was centrifugally cast as opposed to static cast

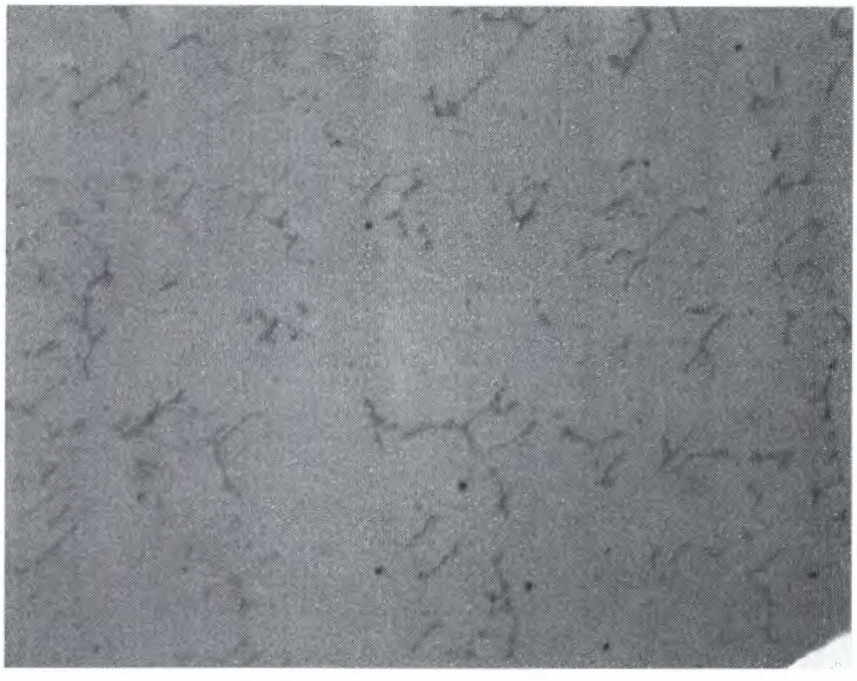


Figure 17. Microstructure of Round Robin Sample "A", NaOH, 100x.



Figure 18. Microstructure of Round Robin Sample "E", NaOH, 100x.

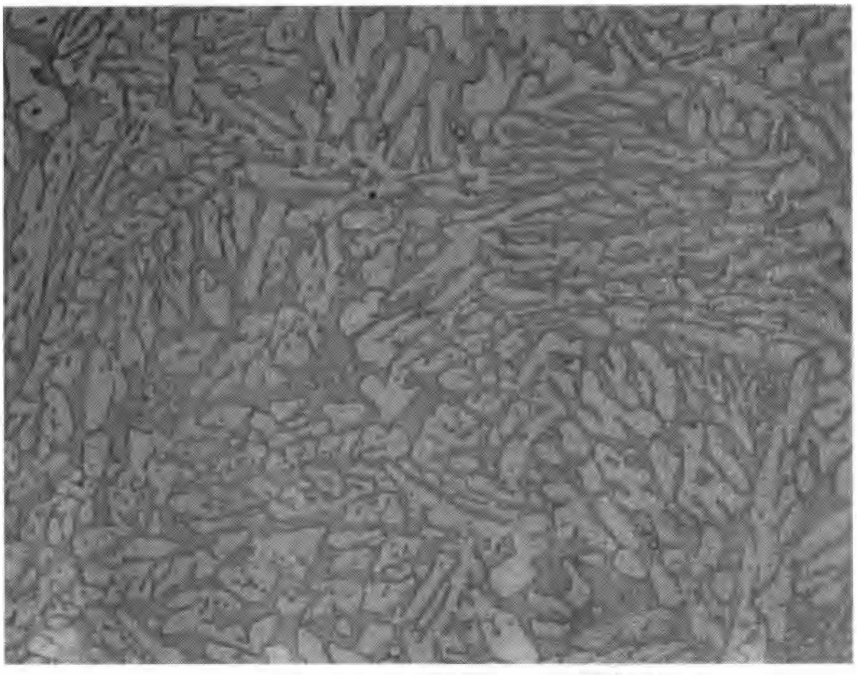


Figure 19. Microstructure of Round Robin Sample "F", NaOH, 100x.

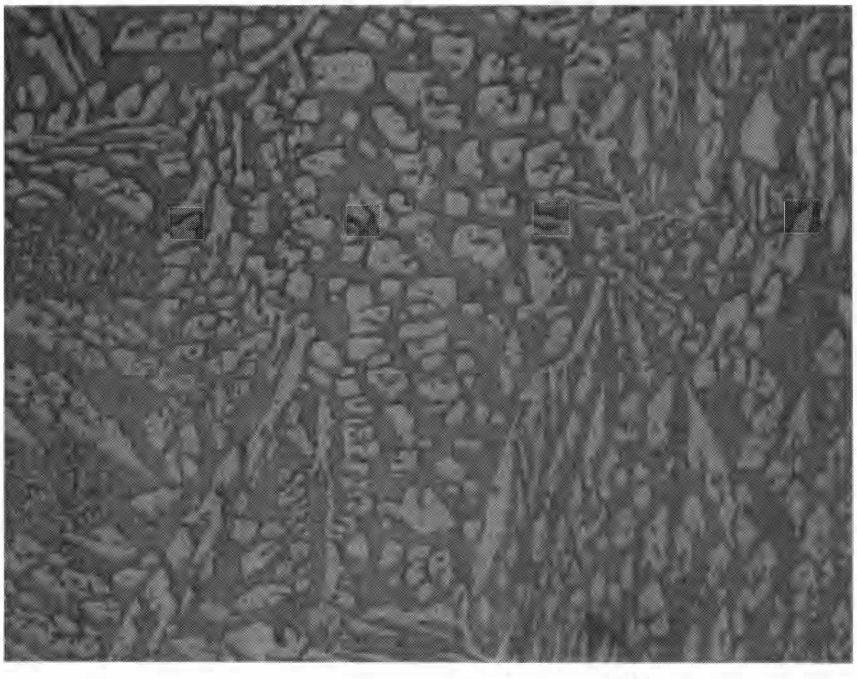


Figure 20. Microstructure of Round Robin Sample "J", NaOH, 100x.

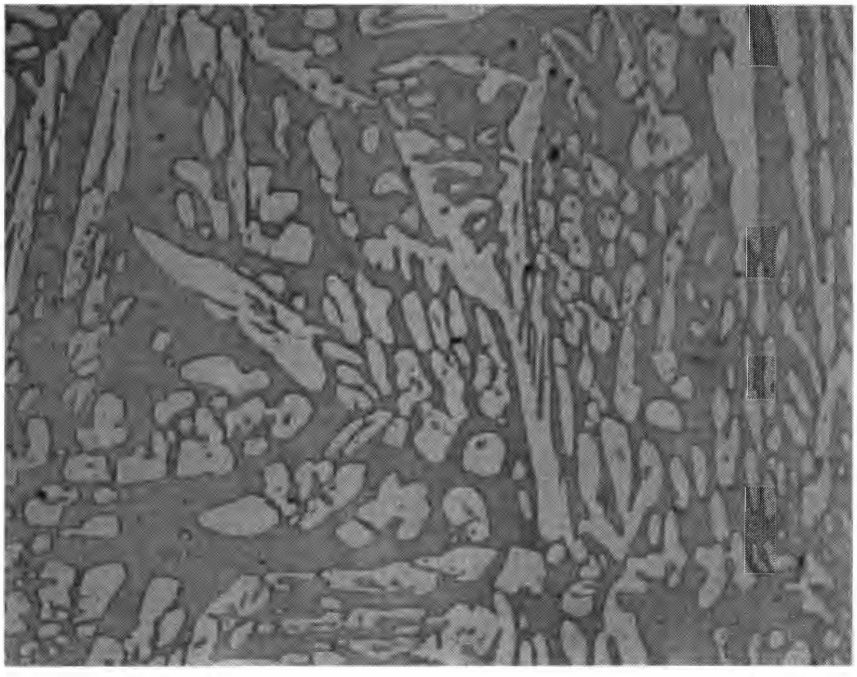


Figure 21. Microstructure of Round Robin Sample "K", NaOH, 100x.

Participants were asked to determine the ferrite content (volume fraction) on the sample set provided using manual point counting per ASTM E562. For the point counting, the procedure in ASTM E562 Annex 1 was to be followed. A visual estimate of area percent ferrite was determined. Using ASTM E562 Table 3, a grid size, P_T was selected based on a required relative accuracy of 20%. The grid was then superimposed upon the microscope viewing screen and magnification was selected such that the size of the ferrite pools was approximately one half of the spacing between grid points. Using ASTM E526 Table 3, the number of fields was determined based on 20% relative accuracy. The spacing between fields was determined in order to form a systematic (equally spaced) array covering a majority of the sample area (inside the scribed circle) without overlap. The number of turns required on the microscope stage translation knobs to move the stage from one field position to the next was determined. The image was not observed while translating in order to avoid bias in positioning the grid. The number of points, P_i, falling within the ferrite was then counted. Any points falling completely within the ferrite were counted as one. Any points falling on a phase boundary or any that were deemed questionable were counted as one half. Data was recorded and returned to UT, where results were tabulated. A sample data sheet is found in Appendix B, where:

P_T = total number of points in the test grid

P_i = point count to the i^{th} field

$P_P(i) = P_i / P_T \times 100$ = percentage of grid points in the ferrite on the i^{th} field

n = number of fields counted

$P_P = 1/n \sum P_P(i)$ = arithmetic average of $P_P(i)$

$s = [1/(n-1) \sum [P_P(i) - P_P]^2]^{1/2}$ = estimate of standard deviation (σ)

95% CI = $\pm$ ts/$\sqrt{n}$ = 95 % confidence interval

t = a multiplier related to the number of fields examined and used in conjunction with the standard deviation of the measurements to determine the 95% CI, see (Table 1 of ASTM E562).

$V_V = P_P \pm$ 95% CI = volume fraction of ferrite as a percentage

% RA = (95% CI / P_P) = % relative accuracy, a measure of statistical precision

The Suitability of ASTM A923 for Detecting the Presence of Intermetallic Phases in Duplex Stainless Steel Castings

Materials

The materials evaluated in this study were ASTM A890-4A (CD3MN), supplied in cast blocks from 2 different foundries and 1 plate of 2205 wrought material. Two of the foundry supplied castings were statically cast and 1 was centrifugally cast (denoted by CC). Each of the blocks was cut into 8 sections in order to have material for each heat treatment. Chemical composition of each lot is summarized in Table 6.

Table 6. Chemical Composition of Tested Materials

Material ID	C	Mn	Si	Cr	Ni	S	P	Mo	Cu	N
ASTM A890-4A (specified)	.03 max	1.50 max	1.00 max	21.0-23.5	4.5-6.5	.020 max	.04 max	2.3-3.5	1.00 max	.10-.30
41NCC	.02	.95	.56	22.3	5.5	.007	.016	3	.75	.2
42R	.026	.39	.74	22.19	6.17	.005	.033	2.83	.19	.24
CD3	.033	.51	.74	22.78	6.66	.01	.024	2.91	.07	.13
2205	.021	.52	.48	22.98	5.8	.007	.029	3.4	.12	.15

Heat Treatments

The heat treatment schedules were derived from the testing of wrought DSS to establish the A923 specification [117]. 8 heat treatment schedules were selected in order to produce a wide range of intermetallic phase precipitation, these heat treatments are shown in Table 7. The solution annealing temperature of 1950°F is lower than that utilized for cast DSS but it duplicates that used to establish A923. Thermocouples were welded to each section prior to heat treatment so that actual thermal history could be recorded. The time / temperature cycles are shown in Figure 22.

Testing Methods

Test Method B

This test method requires Charpy impact testing at -40°C as a method for the detection of intermetallic phases in DSS. Acceptance criteria for this test is a minimum of 40 ft-lbs @ -40°C for 2205 wrought base metal. The same acceptance criteria were used for the cast material.

2 - 3 Charpy impact samples were extracted from the material sections and notched in the orientation shown in Figure 23. Notch Geometry for the Charpy impact samples per ASTM A370 is shown in Figure 24. The Charpy impact test apparatus is shown in Figure 25. This apparatus is a pendulum type of rigid construction that is capable of providing enough impact energy to break a notched sample in one blow.

The samples were then tested as follows per ASTM E23. The samples were placed in an alcohol bath cooled with liquid nitrogen to maintain a temperature of –40°C for a

Table 7. Heat Treatment Schedule

Heat Treatment	Stage 1	Stage 2
A	Heat Sample to 1950°F, Hold 30 min., Water Quench	
B	Heat Sample to 1950°F, Hold 30 min., Water Quench	Heat sample to 1550°F, Water Quench
C	Heat Sample to 1950°F, Hold 30 min., Water Quench	Heat sample to 1550°F, Hold 5 min., Water Quench
D	Heat Sample to 1950°F, Hold 30 min., Water Quench	Heat sample to 1550°F, Hold 10 min., Water Quench
E	Heat Sample to 1950°F, Hold 30 min., Water Quench	Heat sample to 1550°F, Hold 15 min., Water Quench
F	Heat Sample to 1950°F, Hold 30 min., Water Quench	Heat sample to 1550°F, Hold 20 min., Water Quench
G	Heat Sample to 1950°F, Hold 30 min., Air Cool	
H	Heat Sample to 1950°F, Hold 30 min., Slow Cool	

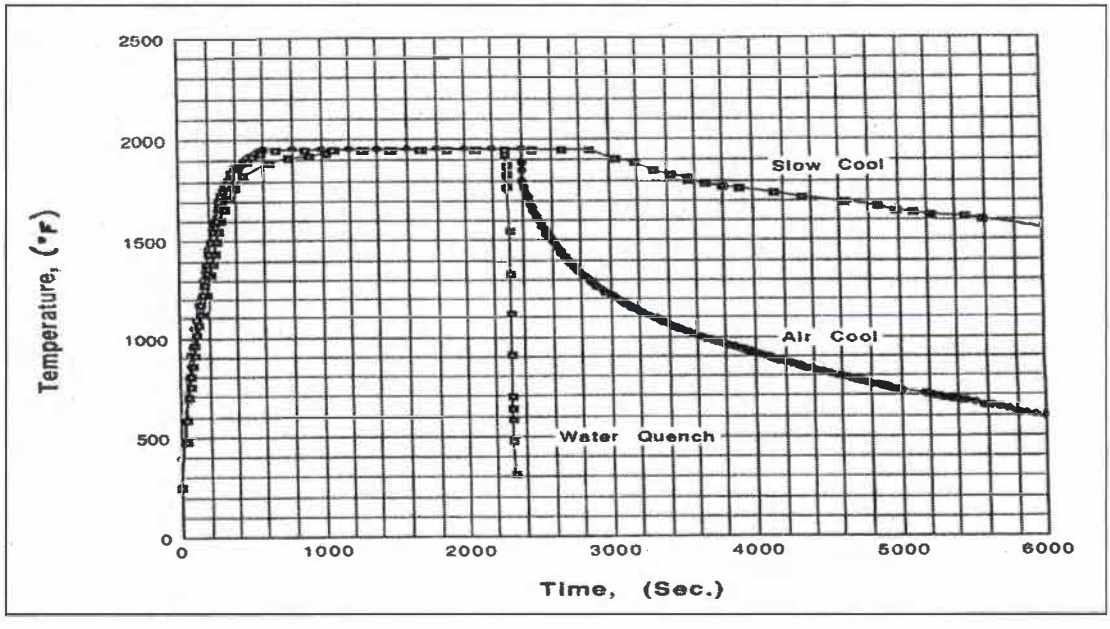


Figure 22. Actual Thermal History for Various Heat Treatments.

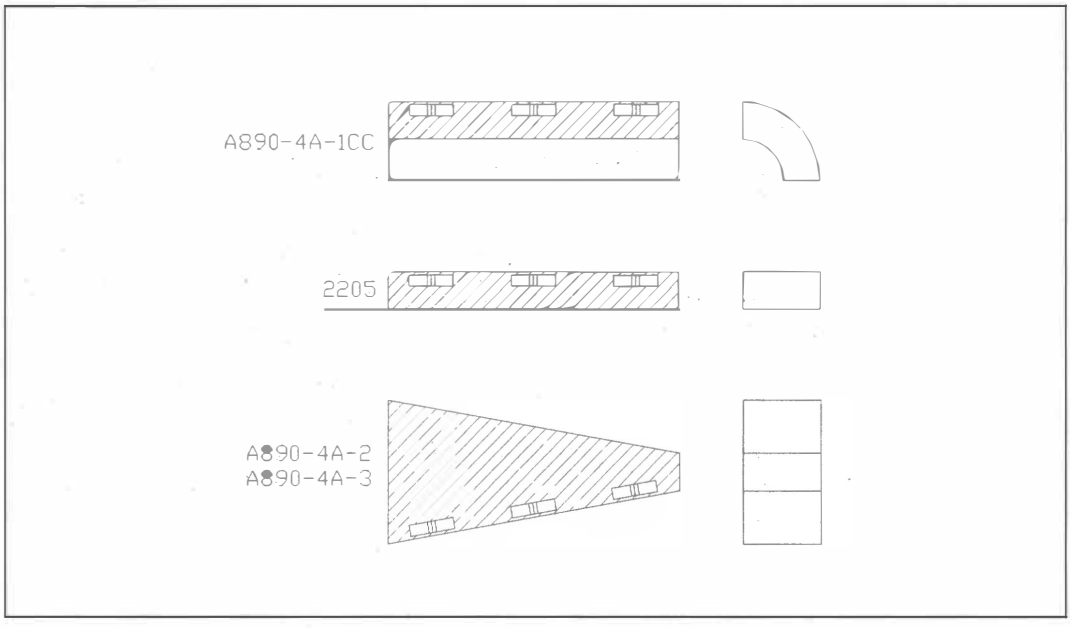


Figure 23. Charpy Impact Sample Extraction Location

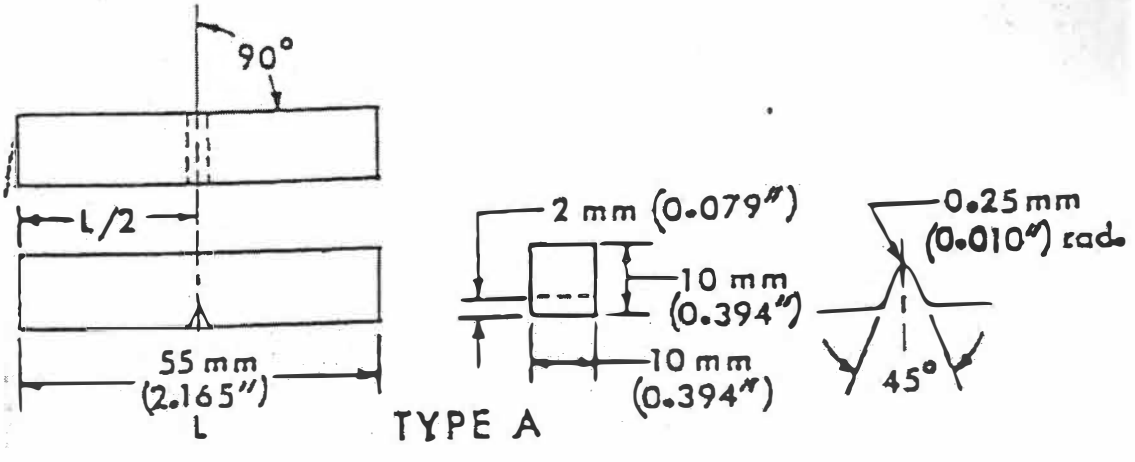


Figure 24. Charpy Impact Notch Geometry

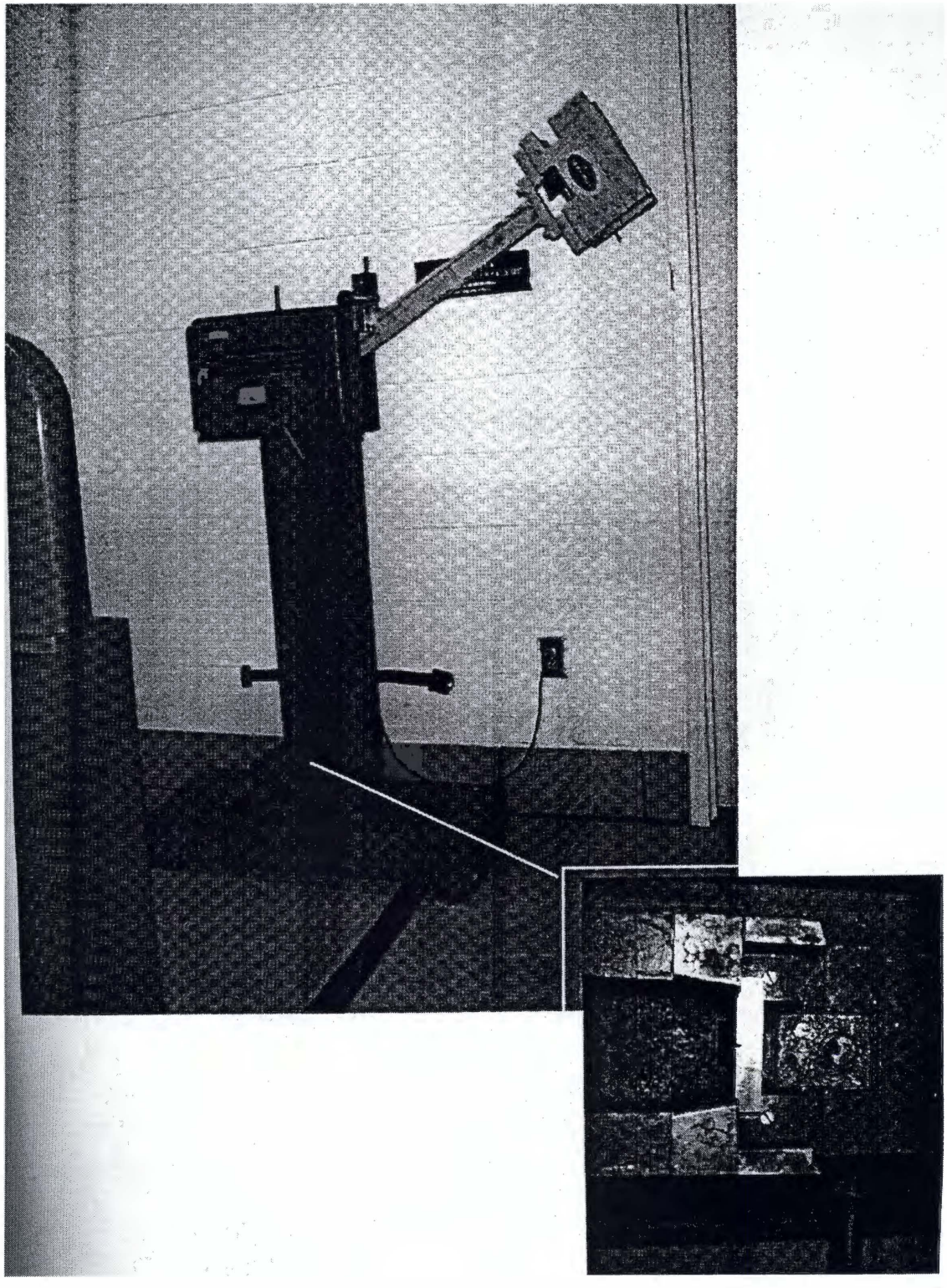


Figure 25. Charpy Impact Test Apparatus

sufficient time to normalize the bars at temperature. Self-centering tongs were used to remove the samples from the liquid nitrogen bath. The sample was placed in the proper orientation in the Charpy impact test apparatus and the pendulum was then released. (This step must take no longer than 5 seconds to perform due to the low temperature that is being used). After impact the broken specimen was placed in a room temperature acetone bath. Data was collected and the fractured samples were placed in individual packages for future examinations that may be required.

Test Method A

After completion of Method B, one half of a fractured Charpy sample from each lot and heat treatment was tested per Method A (sodium hydroxide etch test). The sodium hydroxide etch test may be used for the acceptance of material but not for rejection. This test method may be used with other evaluation tests to provide a rapid method for identifying those specimens that are free of detrimental intermetallic phases as measured in these tests.

On all samples, cross-sectional surfaces were prepared to a metallographic finish suitable for examination at 400x after etching. The etching solution was prepared by adding 40 g reagent grade sodium hydroxide (NaOH) to 100 g of distilled water. Samples were then electrolytically etched at 3 V dc for 15 seconds. Following etching, the specimens were rinsed thoroughly in hot water and in acetone, followed by air drying. The etched surfaces were examined at 400x and classified according to ASTM A923, which supplies photomicrographs of wrought material in order to classify the structure.

The cast material classification had to be determined from the wrought material photomicrographs supplied in A923, with the exception of the centerline structure classification, which would only be applicable to wrought material, see Figures 26-29. ASTM A923 requires that any material showing other than an unaffected structure must be Charpy impact tested per Method B. The following is used to define classify each microstructure:

1. Unaffected Structure (Figure 26) – The sample has been etched and the microstructure is without the revelation of any intermetallic phase. The austenite-ferrite boundaries are smooth.
2. Possibly Affected Structure (Figure 27) – The sample has been etched and isolated indications of possible intermetallic phase are noted. The austenite-ferrite boundaries show a fine waviness.
3. Affected Structure (Figure 28) – The indication of an intermetallic phase is readily revealed upon etching.
4. Centerline Structure (Figure 29) – The intermetallic phase is observed as a continuous or semi-continuous phase in the mid-thickness region of the sample, with or without the affected structure outside of the mid-thickness region, indicative of segregation. This structure is only applicable to wrought materials.

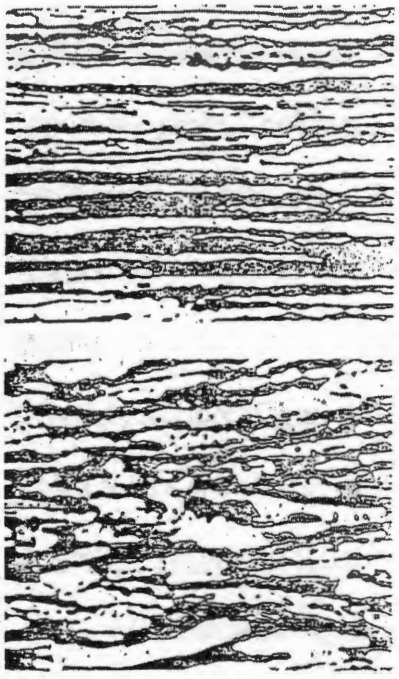


Figure 26. Unaffected
Structure from ASTM A923

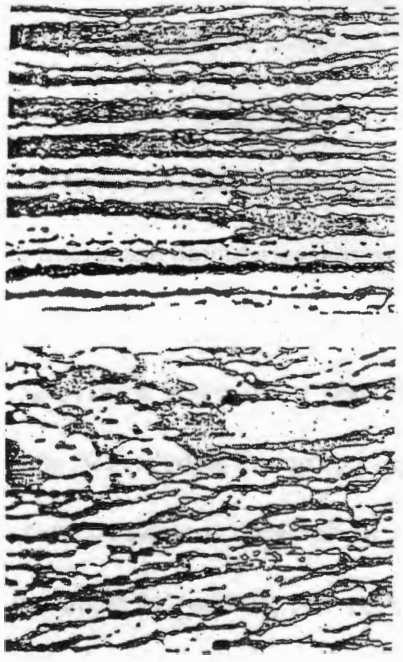


Figure 27. Possibly Affected
Structure from ASTM A923

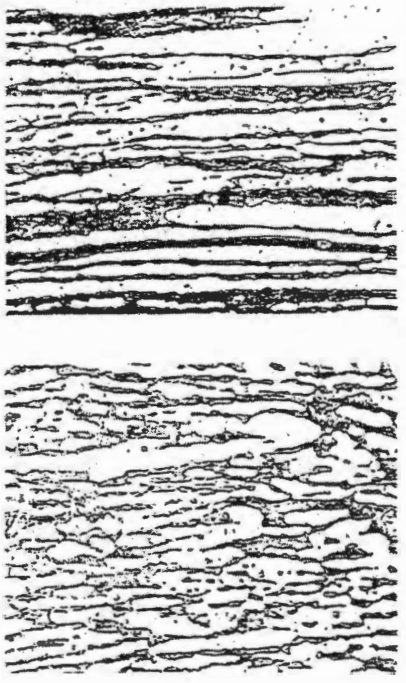


Figure 28. Affected
Structure from ASTM A923

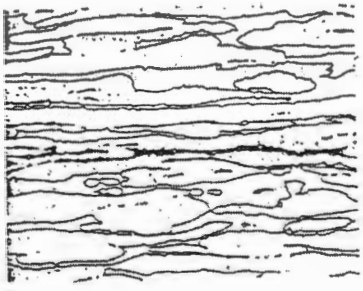


Figure 29. Centerline
Structure from ASTM A923

Test Method C

This test method is a ferric chloride corrosion test for detecting the presence of intermetallic phases in DSS. The presence or absence of corrosive attack in this test is not necessarily a measure of the performance of the material in other corrosive environments; in particular, it does not provide a basis for predicting resistance to forms of corrosion not associated with the precipitation of intermetallic phases.

One half of a fractured Charpy bar was used for this test. The bar was prepared by removing the fracture surface and grinding all surfaces to a 240-grit finish. Sharp edges of the specimen were rounded and care was taken to remove all burrs. Each specimen was labeled on the end by vibra-peening. Specimen weight was recorded to the 0.001 g or better. Exposed surface area on the specimen was calculated after measuring each face.

A test solution of 100 g reagent grade ferric chloride $FeCl_3$-$6H_2O$ was dissolved in 900 ml of distilled water (6% $FeCl_3$ by weight). The solution was filtered through filter paper to remove insoluble particles. The pH of the test solution was adjusted to approximately 1.3 prior to beginning the test by the addition of HCl or NaOH, as required. The test solution was then transferred to a 1000 ml, wide neck, glass beaker. The beaker was placed in a water bath as shown in Figure 30. Bath temperature was set at 25°C. After the test solution temperature reached the bath temperature the samples were placed in glass cradles and lowered into the solution. This test was performed at temperature for 24 hours. At the end of the 24 hour test period, the specimens were removed from the solution. Specimens were rinsed with water, scrubbed with a soft bristle brush under

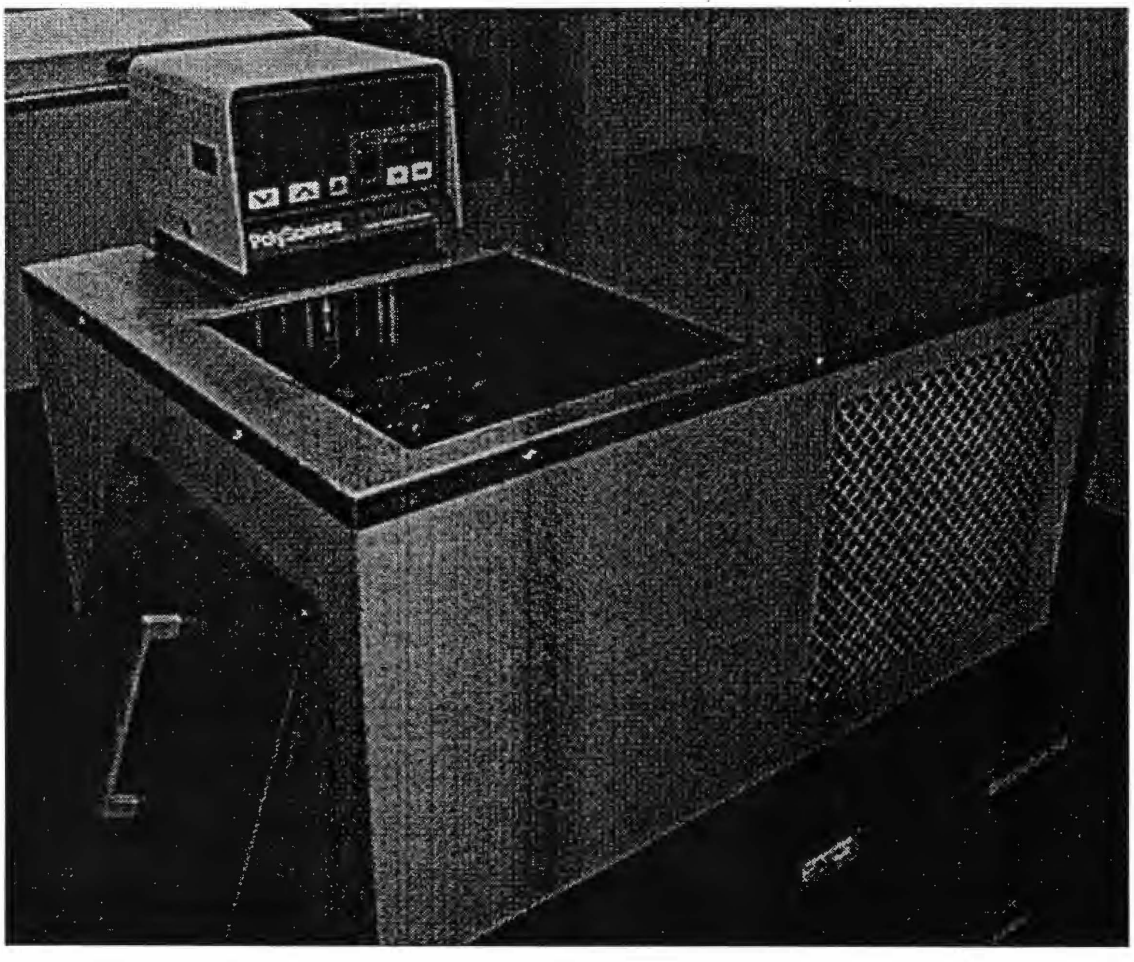


Figure 30. Temperature Controlled Water Bath

running water to remove corrosive products, dipped in acetone, and then dried in air. Specimens were then re-weighed to 0.001 g or better. The acceptance criterion for this test is that no specimen shall show a weight loss of more than 10 milligrams/decimeter/day (10 mdd), as calculated by:

Corrosion rate = weight loss (mg)/[specimen area (dm^2) x time (days)] Equation 8

ASTM A923 Method A & C Round Robin Study

This round robin study was used to correlate the data obtained from "The Suitability of ASTM A923 for Detecting the Presence of Intermetallic Phases in Duplex Stainless Steel Castings" and the data obtained from numerous different laboratories.

Materials

One half of a fractured Charpy sample from each lot and heat treatment used in "The Suitability of ASTM A923 for Detecting the Presence of Intermetallic Phases in Duplex Stainless Steel Castings" was tested per ASTM A923 Method A and the other half of the Charpy sample was tested per ASTM A923 Method C.

Method A samples were mounted in epoxy and ground to120-grit finish. Identification was vibra-peened on the side of the mount.

Method C samples were prepared by removing the Charpy fracture surface and grinding all surfaces to a 240-grit finish. Sharp edges of the specimen were rounded and

care was taken to remove all burrs. Each specimen was labeled on the end by vibra-peening.

Testing Methods

Both groups of samples were shipped to the first laboratory in the previously described condition. Testing procedures for the laboratory were identical to those used in "The Suitability of ASTM A923 for Detecting the Presence of Intermetallic Phases in Duplex Stainless Steel Castings". After testing, the samples were returned to UT, restored to their previous untested condition, and shipped to the next participant.

ASTM A923 Study of the Effectiveness of Existing Foundry Solution Annealing Procedures for Producing Cast DSS Without Intermetallic Phases

Materials

The materials evaluated in this study were 10 heats of ASTM A890-4A (CD3MN) cast keel blocks all supplied from the same foundry. Table 8 summarizes the chemical composition of each heat.

Heat Treatment

All 10 heats of material for this study were solution annealed by the same schedule. Table 9 shows the foundry solution anneal schedule. Table 10 shows the volume percent ferrite values for each heat treatment, calculated using Equation 1, from the measured extended ferrite numbers (EFN) using the Feritscope®.

Table 8. Chemical Composition of Foundry Solution Annealed Materials

Material ID	C	Mn	Si	Cr	Ni	S	P	Mo	Cu	N
ASTM 890-4A (specified)	.03 max	1.50 max	1.00 max	21.0-23.5	4.5-6.5	.020 max	.04 max	2.3-3.5	1.00 max	.10-.30
4A-SA-1	.025	.777	.739	21.00	5.460	.007	.008	2.983	.116	.170
4A-SA-2	.023	.740	.656	22.000	5.215	.007	.008	3.004	.165	.173
4A-SA-3	.026	.812	.663	22.104	5.435	.007	.014	2.908	.152	.170
4A-SA-4	.030	.755	.724	21.895	4.995	.007	.017	2.975	.186	.173
4A-SA-6	.019	.710	.708	21.885	4.990	.007	.028	2.990	.162	.167
4A-SA-7	.018	.756	.707	22.340	5.010	.008	.021	2.984	.194	.175
4A-SA-8	.018	.760	.663	22.700	4.905	.008	.020	2.935	.184	.175
4A-SA-9	.021	.764	.658	22.660	4.910	.009	.020	2.990	.179	.185
4A-SA-10	.020	.757	.681	22.545	4.985	.007	.021	2.982	.180	.185
4A-SA-11	.019	.764	.689	22.720	4.955	.007	.022	2.977	.172	.190

Table 9. Foundry Solution Anneal Heat Treatment Schedule

Foundry Solution Anneal Procedure
Heat to 2100°F
Hold at 2100°F for 2 hours
Water Quench

Table 10. Volume Percent Ferrite

Material ID	Volume Percent Ferrite (Calculated from EFN measured on Feritscope® using Equation 1)
4A-SA-1	50.6
4A-SA-2	53.2
4A-SA-3	50.8
4A-SA-4	51.9
4A-SA-6	55.8
4A-SA-7	56.7
4A-SA-8	61.8
4A-SA-9	57.0
4A-SA-10	58.3
4A-SA-11	60.8

Test Methods

Testing procedures for this study were identical to those used in "The Suitability of ASTM A923 for Detecting the Presence of Intermetallic Phases in Duplex Stainless Steel Castings".

V. Results and Discussion

ASTM E562 Ferrite Measurement Round Robin Study

Table 11 shows the average volume fraction of ferrite in the cast DSS samples, as determined per ASTM E562, ranges from 6.2 – 54.7. Figure 31 shows the comparison between volume fraction of ferrite from the Feritescope® (Equation 7) and volume fraction of ferrite per ASTM E562. Volume fraction of ferrite measurements, converted from FN measured by the Feritescope® (Equation 7), fall within the 95% confidence limits for volume fraction of ferrite measurements per ASTM E562,except for sample A, where the Feritescope® measurement falls below the limit.

Ruprecht [135] identified a standard deviation of less than 14% as being sufficient interlaboratory reproducibility for cast DSS ferrite measurement using the Feritescope®. The standard deviation for the cast DSS samples measured per ASTM E562 ranges from 2.2% - 5.5%, which indicates that ferrite measurement per ASTM E562, in cast DSS, is more reproducible that measurements using the Feritescope®.

Several factors that can affect the accuracy of ASTM E562 with respect to ferrite determination in DSS castings are as follows:

1.) Specimen preparation: Surfaces defects or abnormalities due polishing or etching can lead to difficulty in distinguishing between phases. Also the sample must be properly etched so that there is a definitive difference between phases to be counted.

2.) Grid preparation: Thicknesses of grid lines can cause difficulty in determining if a phase actually lies at the intersection or not.

Table 11. ASTM E562 Results

Sample ID	Participant	Volume Fraction of Ferrite	Average Volume Fraction	Standard Deviation	95% Confidence Limit	Ferrite Number (Feritescope®)	Average Volume Fraction per Feritescope® (Calculated from Eq. 7)
A	1	4.72	6.18	2.21	4.33 – 8.03	2.5	2.5
	2	6.91					
	3	6.45					
	4	8.30					
	5	9.65					
	6	5.79					
	7	5.10					
	8	2.48					
E	1	39.27	40.47	3.91	37.71-44.24	54.9	40.80
	2	40.00					
	3	37.92					
	4	45.60					
	5	35.50					
	6	38.92					
	7	45.92					
	8	44.68					
F	1	38.06	40.63	5.46	37.14-46.27	61.5	44.43
	2	36.46					
	3	38.13					
	4	52.60					
	5	38.67					
	6	44.50					
	7	45.58					
	8	39.61					
J	1	52.60	53.61	4.05	52.12-58.89	75.1	51.91
	2	49.48					
	3	59.06					
	4	58.70					
	5	50.33					
	6	58.95					
	7	58.16					
	8	56.76					
K	1	51.67	54.71	5.53	49.27-58.52	81.4	55.37
	2	47.19					
	3	49.06					
	4	62.50					
	5	48.57					
	6	57.70					
	7	58.16					
	8	56.33					

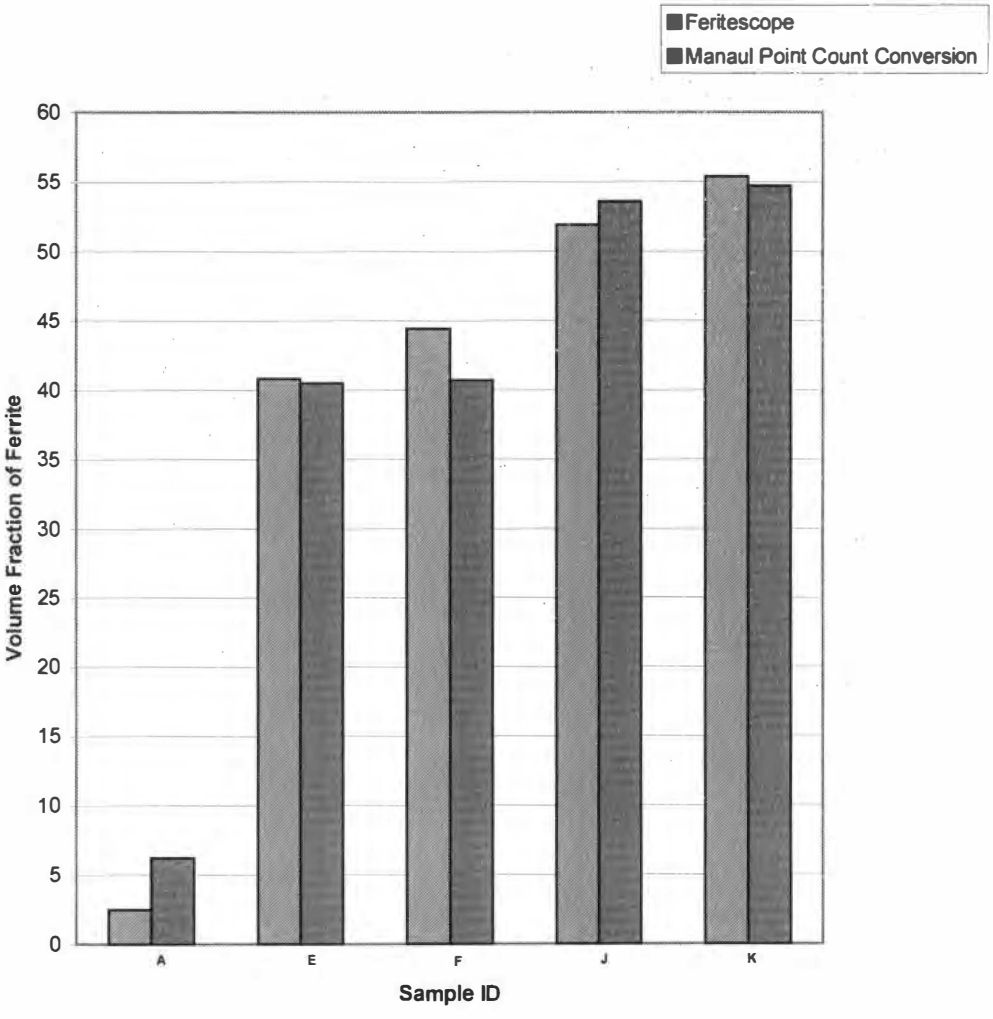


Figure 31. Comparison of Volume Fraction of Ferrite per Feritescope® and ASTM E562 Manual Point Count

3.) Operator bias

It can be concluded from the results that either method of ferrite determination would produce similar results but ASTM E562 would be the most reliable method. However, the Feritescope® would be the preferred method for ferrite determination since it is non-destructive, much faster, and can eliminate operator bias with respect to ASTM E562 and ASTM E562 Manual Point Count

The Suitability of ASTM A923 for Detecting the Presence of Intermetallic Phases in Duplex Stainless Steel Castings

Test Method B

Table 12 shows the Charpy impact energy of each sample tested. Figure 32 shows a graphical view of the average Charpy impact toughness for each lot and heat treatment.

Test Method A

Table 13 summarizes the classification of the etch structure as determined from Method A. Figures 33-64 show the microstructure for each material.

Test Method C

Table 14 summarizes the corrosion rates of each lot and heat treatment per Method C. Figure 65 shows a graphical view of the results.

Table 12. Charpy Impact Toughness at –40°C (-40°F)

Heat Treatment	Absorbed Energy (ft lbs)			
	2205	**41NCC**	**42R**	**CD3**
A Heat to 1950°F, Hold 30 min., Water Quench	1 - 107.5 2 - 102.0 3 - 104.0	1 – 41.0 2 – 90.5 3 – 120.0	1 – 149.0 2 – 123.0	1 – 109.0 2 – 109.0 3 – 100.0
B Heat to 1950°F, Hold 30 min., Water Quench, Heat to 1550°F, Water Quench	1 - 38.0 2 - 34.0	1 – 49.0 2 – 46.0 3 – 45.0	1 – 37.0 2 – 31.5 3 – 32.5	1 – 87.0 2 – 86.5 3 – 77.0
C Heat to 1950°F, Hold 30 min., Water Quench, Heat to 1550°F, Hold 5 min., Water Quench	1 - 17.5 2 - 15.0 3 - 16.0	1 – 20.0 2 – 19.0 3 – 16.0	1 – 38.0 2 – 39.0 3 – 40.0	1 – 65.0 2 – 53.0
D Heat to 1950°F, Hold 30 min., Water Quench, Heat to 1550°F, Hold 10 min., Water Quench	1 - 7.5 2 - 6.0	1 – 16.5 2 – 14.0 3 – 14.0	1 – 28.0 2 – 23.0	1 – 37.0 2 – 35.0
E Heat to 1950°F, Hold 30 min., Water Quench, Heat to 1550°F, Hold 15 min., Water Quench	1 - 16.0 2 – 12.0 3 – 16.5	1 – 9.5 2 – 11.2 3 – 7.5	1 – 35.0 2 – 33.0 3 – 38.0	1 – 32.5 2 – 12.5 3 – 32.5
F Heat to 1950°F, Hold 30 min., Water Quench, Heat to 1550°F, Hold 20 min., Water Quench	1 –6.0 2 – 5.5	1 – 10.0 2 – 11.0 3 – 8.5	1 – 14.0 2 – 21.0 3 – 14.5	1 – 38.5 2 – 20.0 3 – 21.0
G Heat to 1950°F, Hold 30 min., Air Cool	1 – 11.5 2 – 10.0	1 – 16.0 2 – 19.0 3 – 31.0	1 – 28.0 2 – 25.0 3 – 23.0	1 – 47.0 2 – 52.0
H Heat to 1950°F, Hold 30 min., Slow Cool	1 – 2.0 2 – 3.0 3 – 2.0	1 – 4.0 2 – 3.5 3 – 3.5	1 – 5.0 2 – 5.0	1 – 7.0 2 – 8.0 3 – 9.0

Figure 32. Charpy Impact Toughness at –40°C (-40°F)

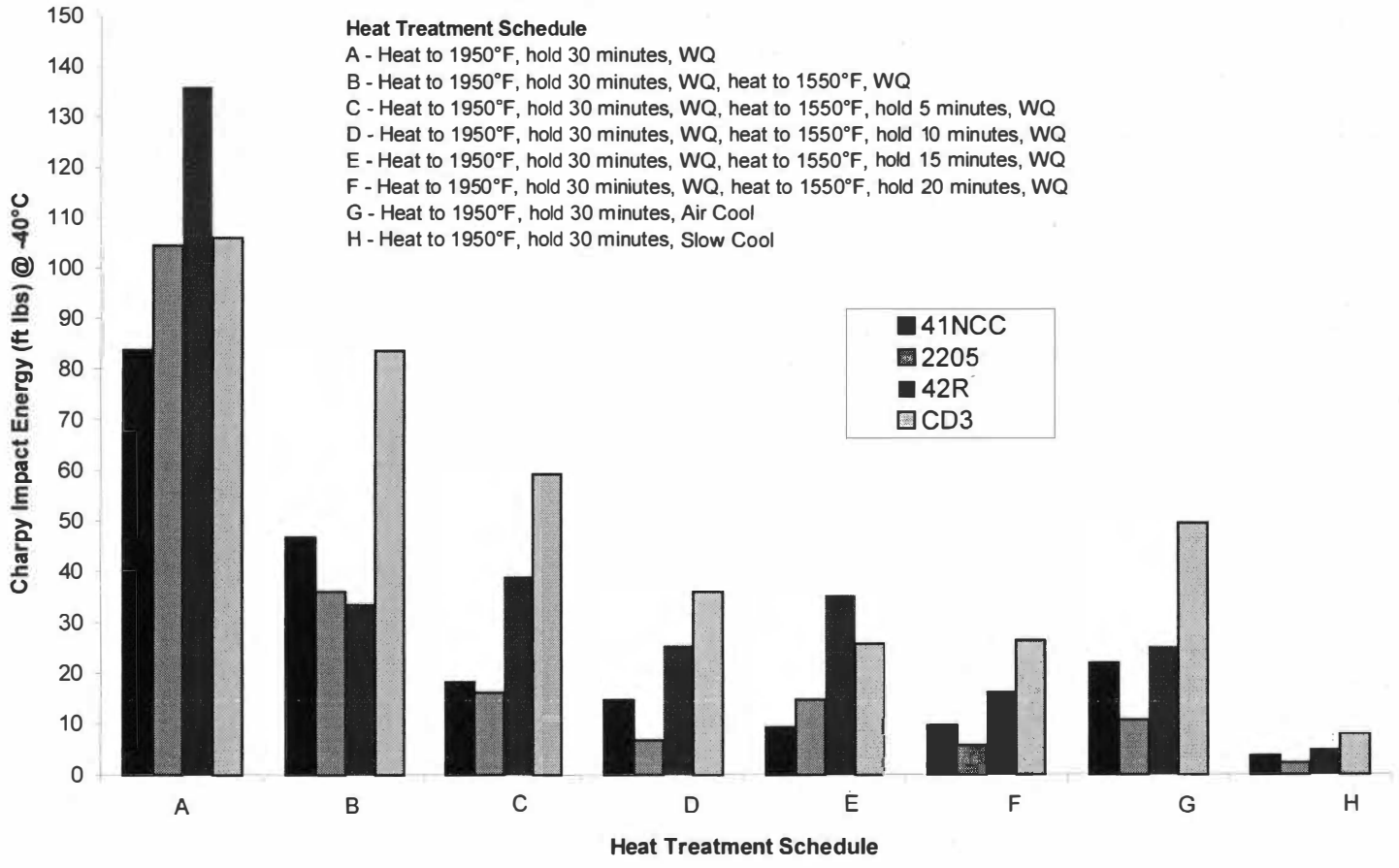


Table 13. Classification of Etch Structure

Heat Treatment	Classification of Etch Structure			
	2205	41NCC	42R	CD3
A Heat to 1950°F, Hold 30 min., Water Quench	Unaffected Structure	Unaffected Structure	Unaffected Structure	Unaffected Structure
B Heat to 1950°F, Hold 30 min., Water Quench, Heat to 1550°F, Water Quench	Possibly Affected Structure	Possibly Affected Structure	Possibly Affected Structure	Possibly Affected Structure
C Heat to 1950°F, Hold 30 min., Water Quench, Heat to 1550°F, Hold 5 min., Water Quench	Possibly Affected Structure	Affected Structure	Possibly Affected Structure	Affected Structure
D Heat to 1950°F, Hold 30 min., Water Quench, Heat to 1550°F, Hold 10 min., Water Quench	Possibly Affected Structure	Affected Structure	Affected Structure	Affected Structure
E Heat to 1950°F, Hold 30 min., Water Quench, Heat to 1550°F, Hold 15 min., Water Quench	Possibly Affected Structure	Affected Structure	Affected Structure	Affected Structure
F Heat to 1950°F, Hold 30 min., Water Quench, Heat to 1550°F, Hold 20 min., Water Quench	Affected Structure	Affected Structure	Affected Structure	Affected Structure
G Heat to 1950°F, Hold 30 min., Air Cool	Unaffected Structure	Unaffected Structure	Unaffected Structure	Unaffected Structure
H Heat to 1950°F, Hold 30 min., Slow Cool	Affected Structure	Affected Structure	Affected Structure	Affected Structure

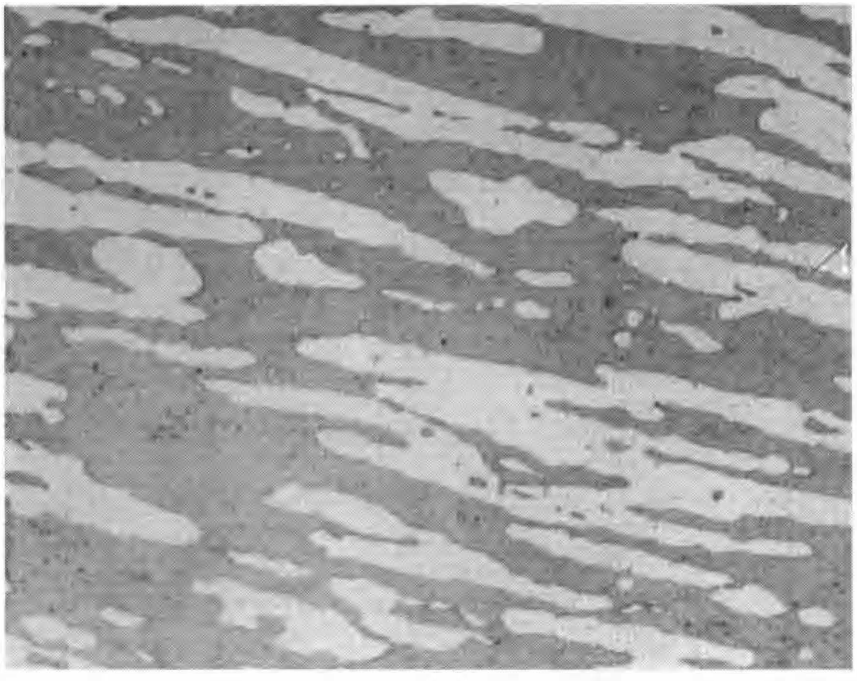


Figure 33. Microstructure of 2205-A-3, NaOH, 400x

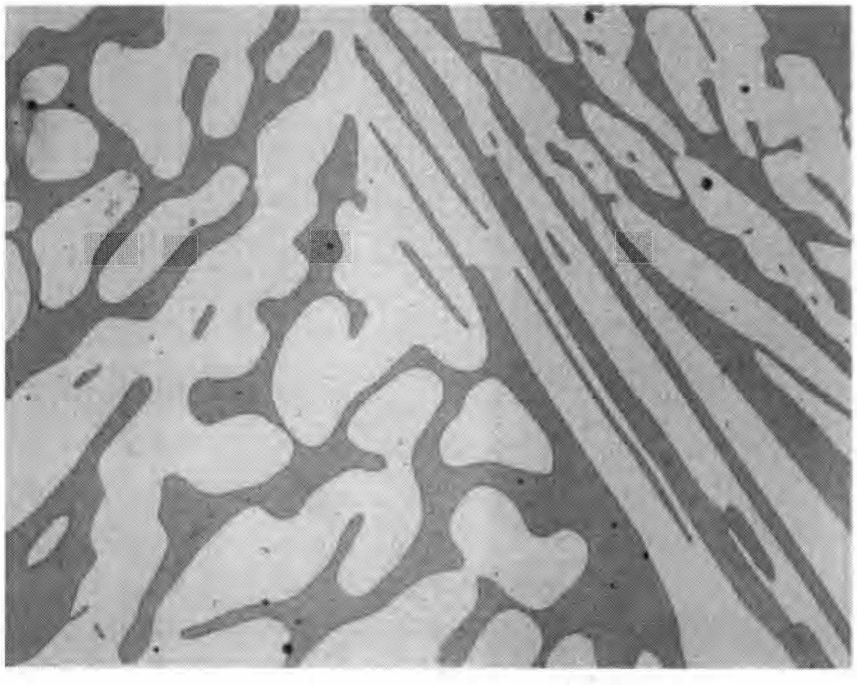


Figure 34. Microstructure of 41NCC-A-1, NaOH, 400x

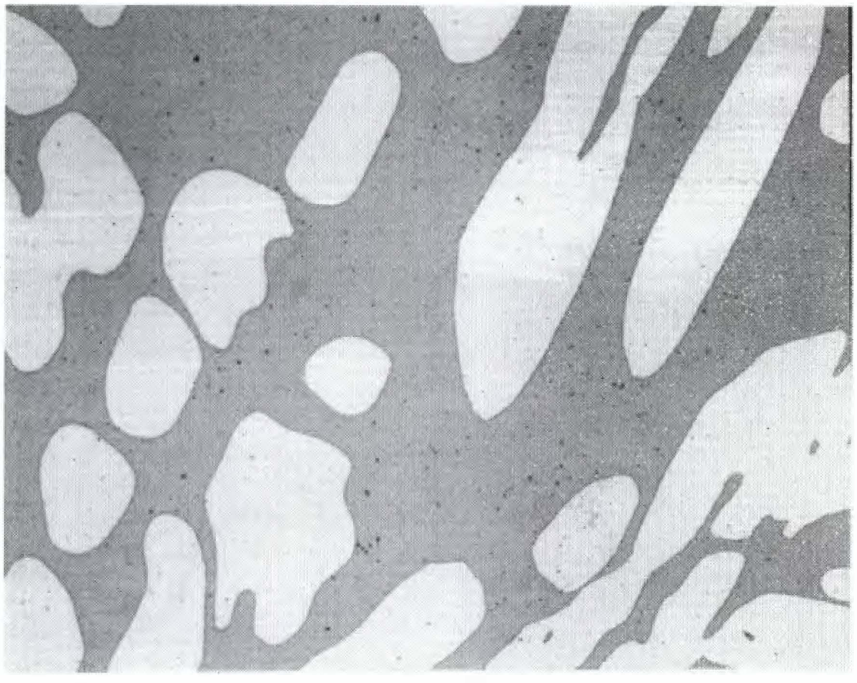


Figure 35. Microstructure of 42R-A-1, NaOH, 400x

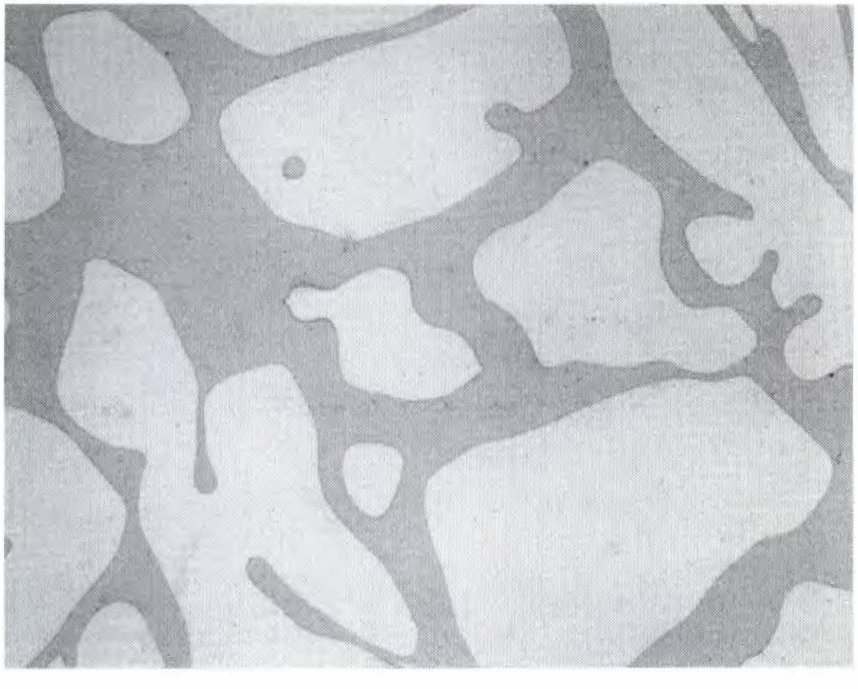


Figure 36. Microstructure of CD3-A-2, NaOH, 400x

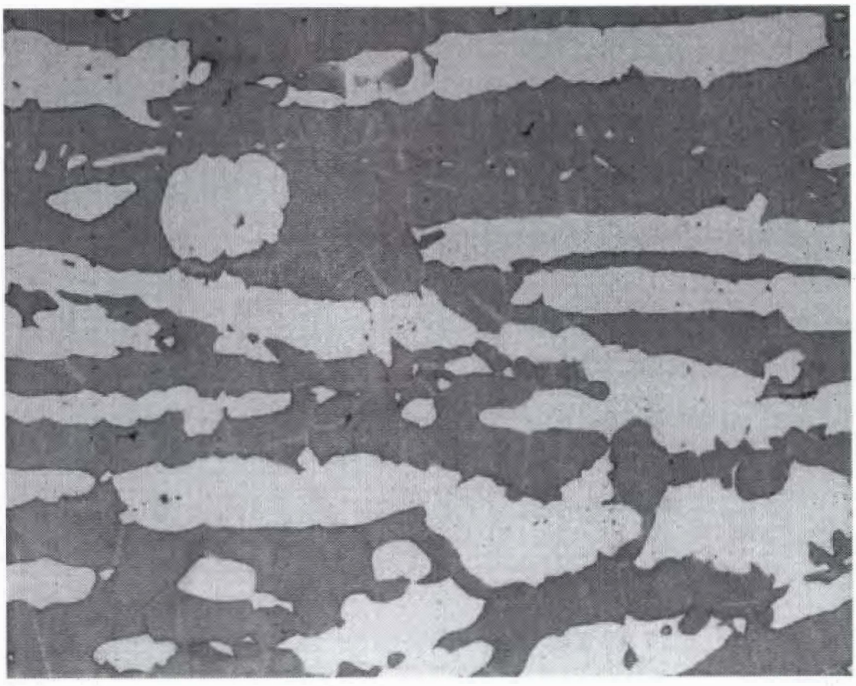


Figure 37. Microstructure of 2205-B-2, NaOH, 400x

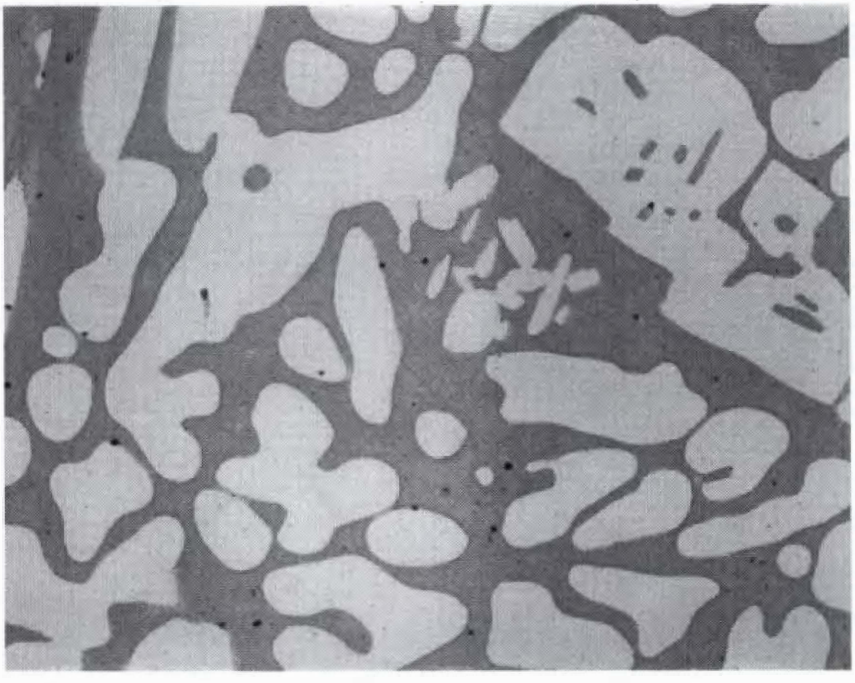


Figure 38. Microstructure of 41NCC-B-2, NaOH, 400x

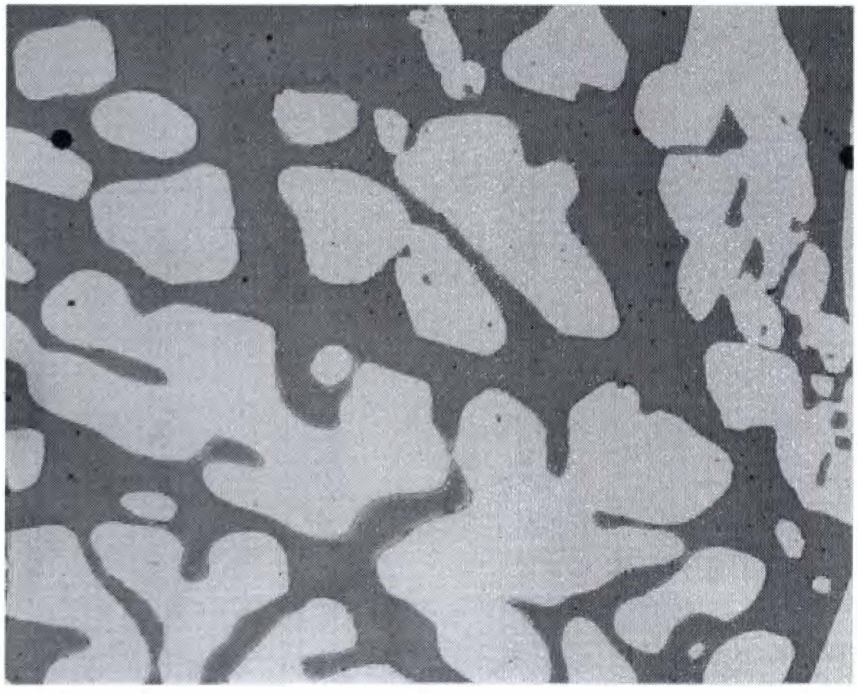


Figure 39. Microstructure of 42R-B-1, NaOH, 400x

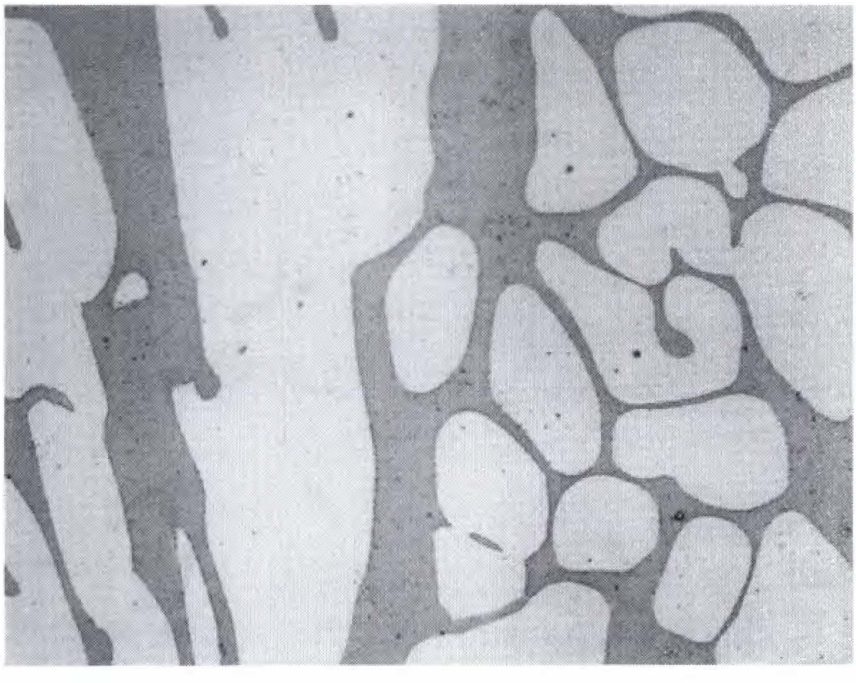


Figure 40. Microstructure of CD3-B-1, NaOH, 400x

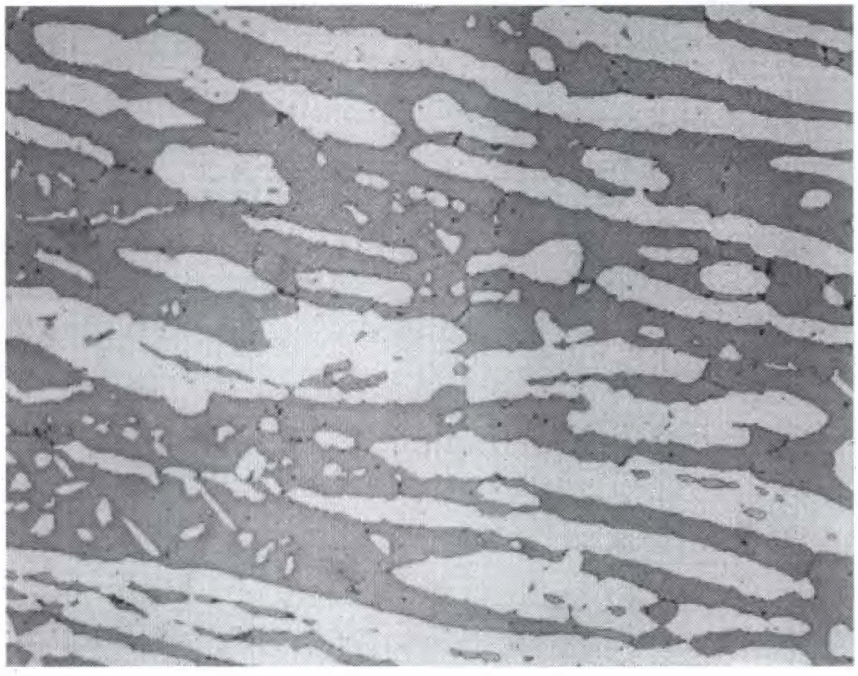


Figure 41. Microstructure of 2205-C-1, NaOH, 400x

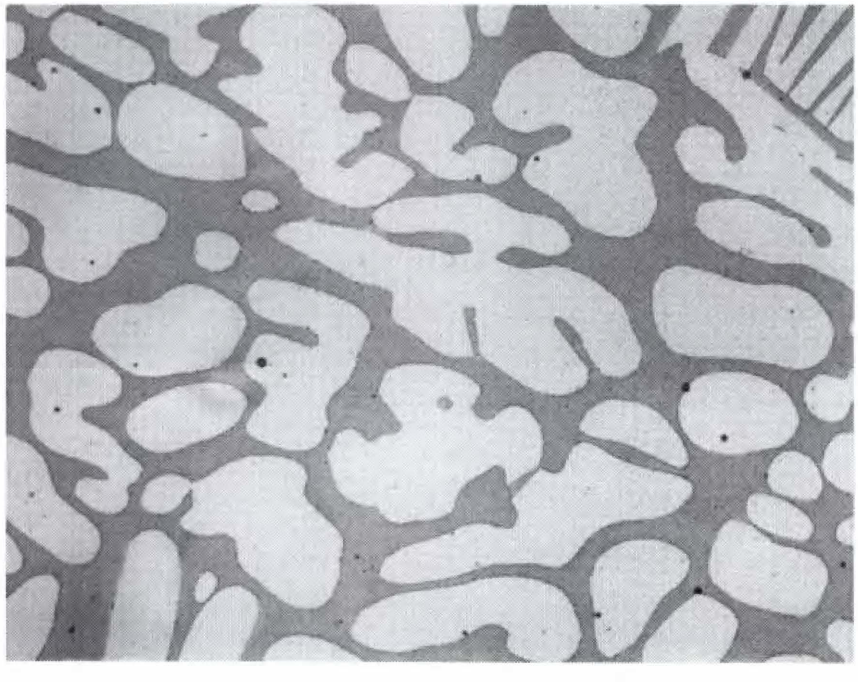


Figure 42. Microstructure of 41NCC-C-1, NaOH, 400x

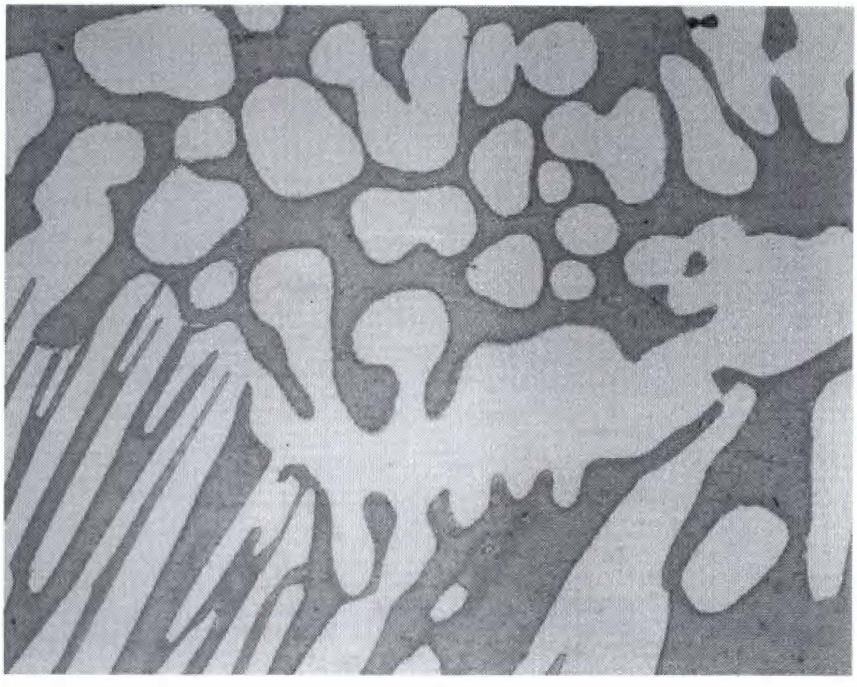


Figure 43. Microstructure of 42R-C-1, NaOH, 400x

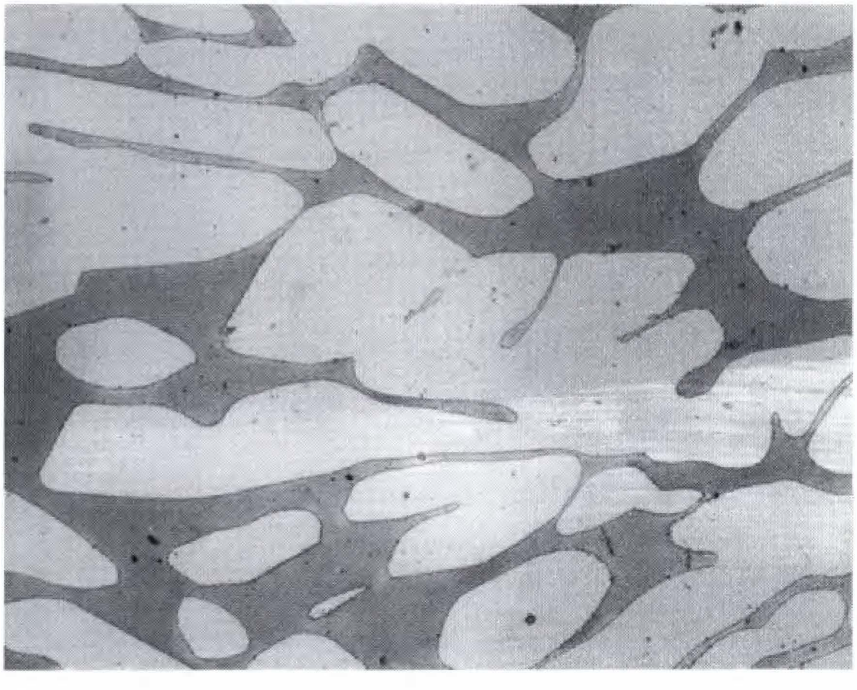


Figure 44. Microstructure of CD3-C-2, NaOH, 400x

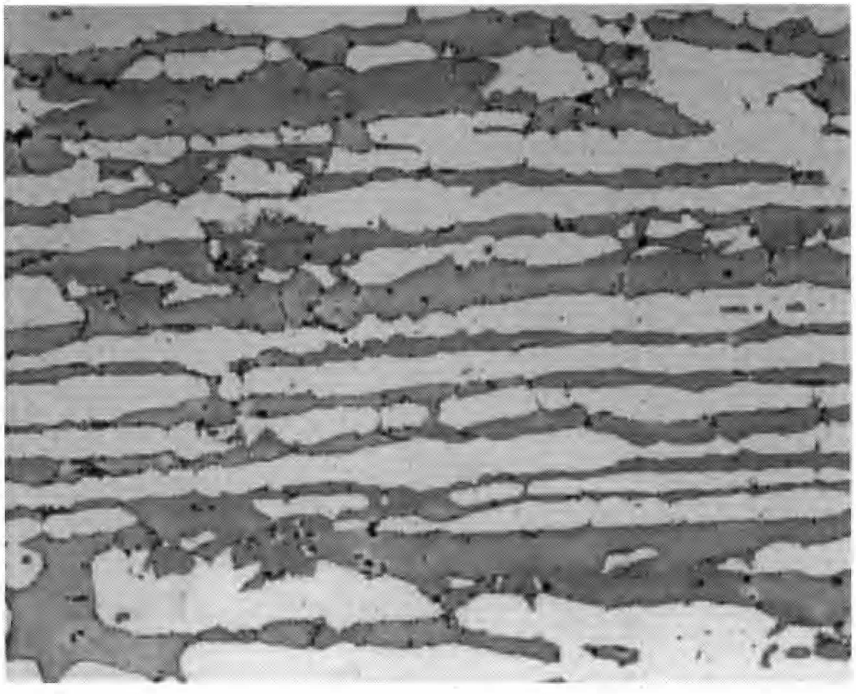


Figure 45. Microstructure of 2205-D-1, NaOH, 400x

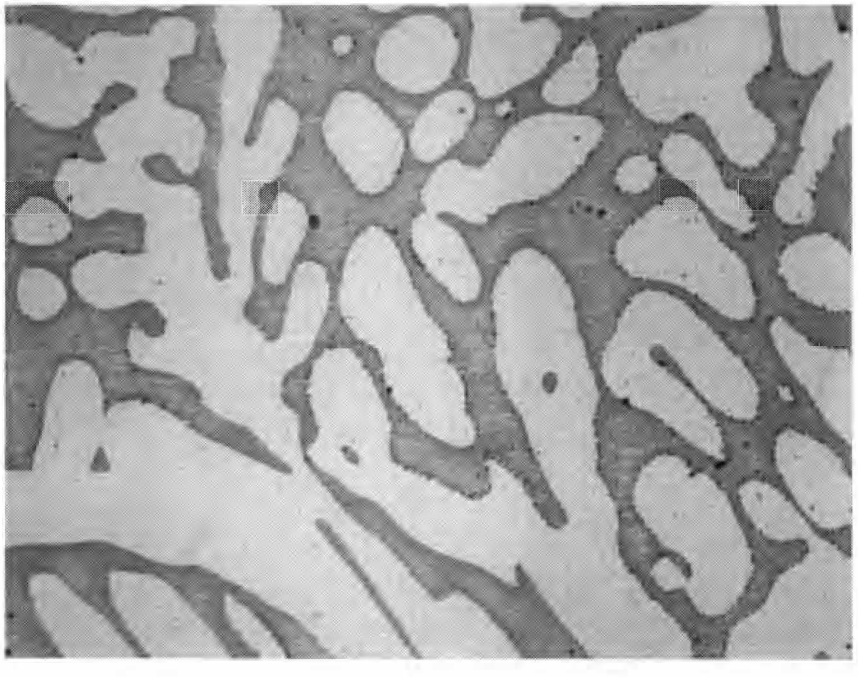


Figure 46. Microstructure of 41NCC-D-2, NaOH, 400x

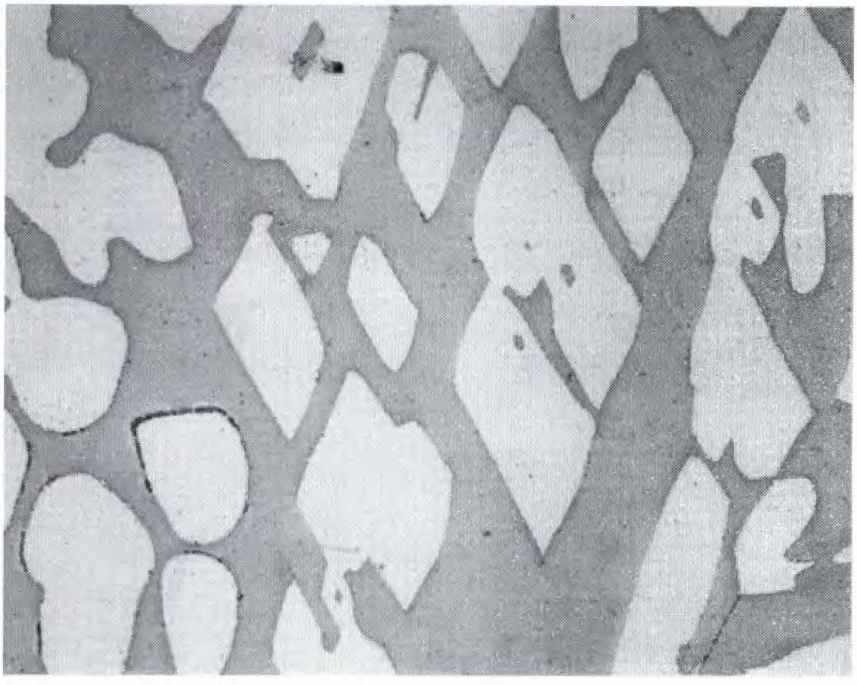


Figure 47. Microstructure of 42R-D-1, NaOH, 400x

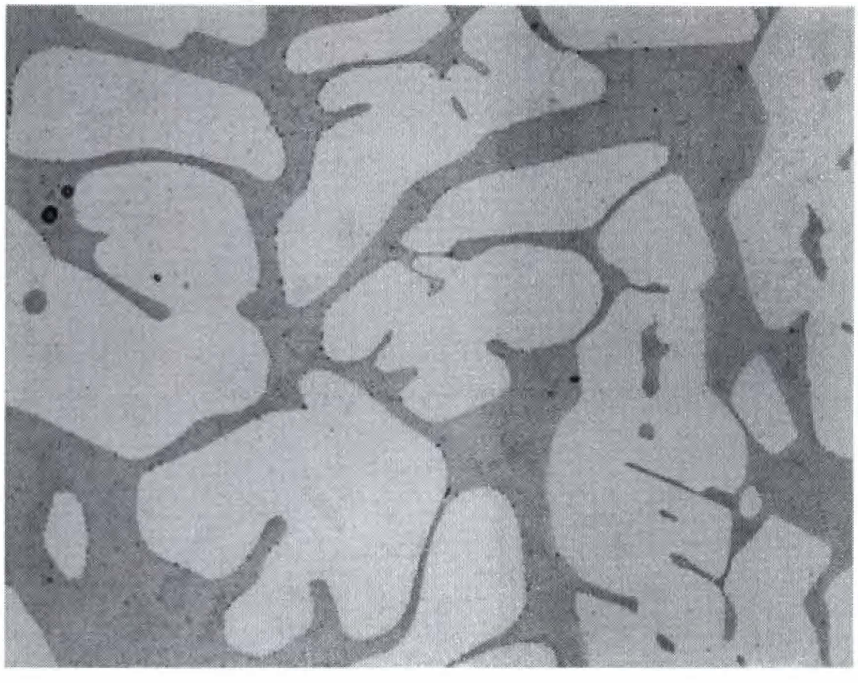


Figure 48. Microstructure of CD3-D-2, NaOH, 400x

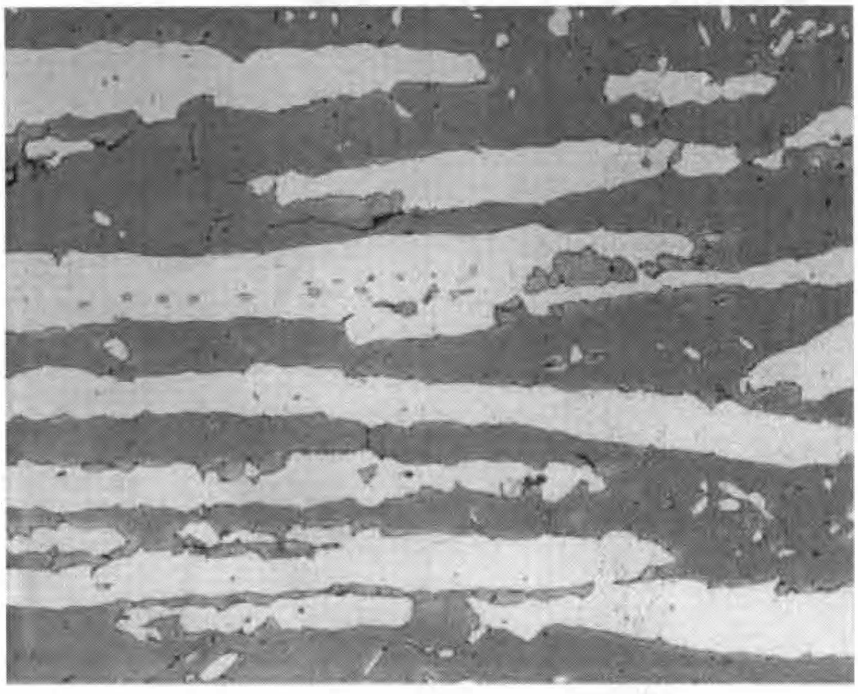


Figure 49. Microstructure of 2205-E-1, NaOH, 400x

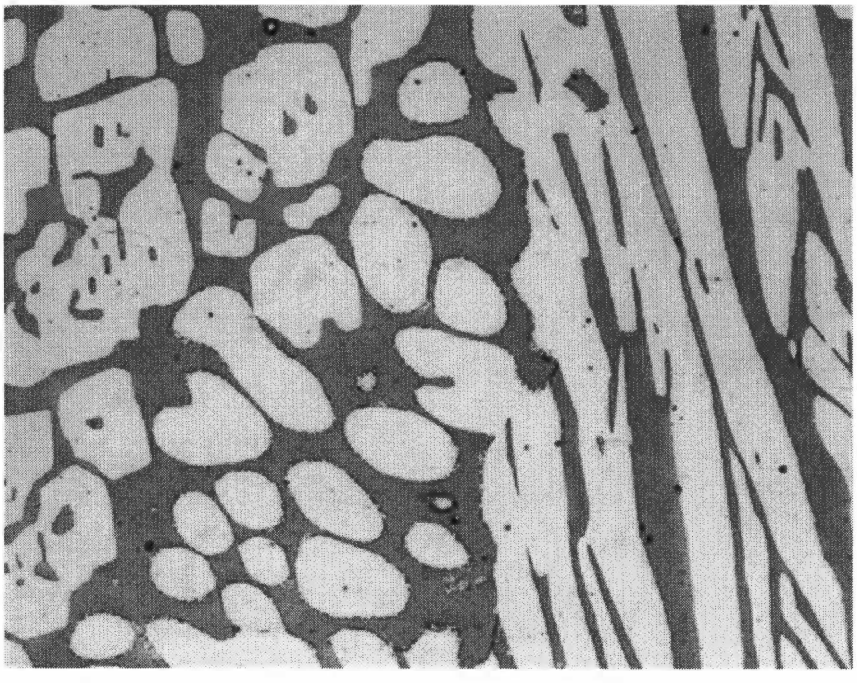


Figure 50. Microstructure of 41NCC-E-1, NaOH, 400x

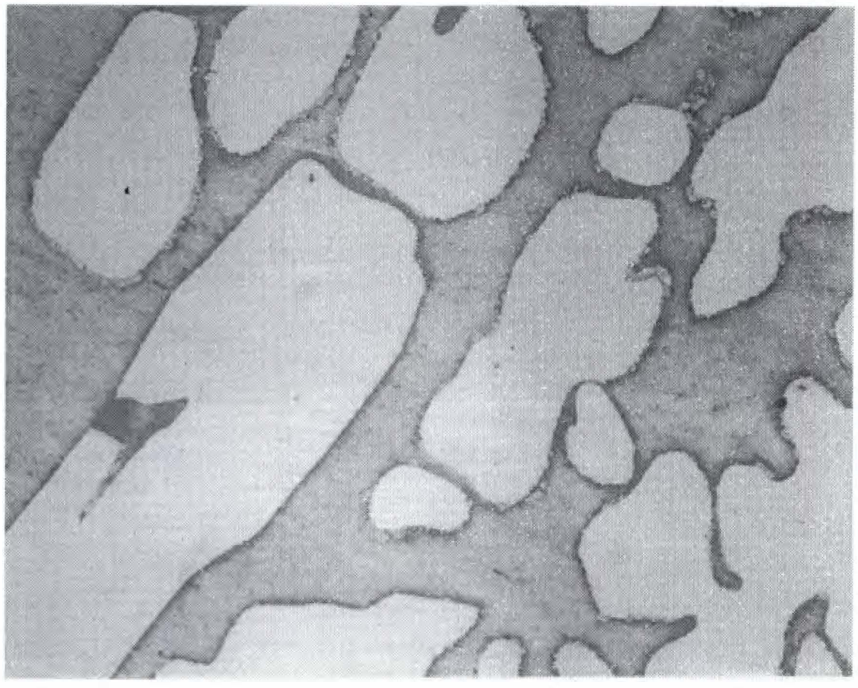


Figure 51. Microstructure of 42R-E-1, NaOH, 400x

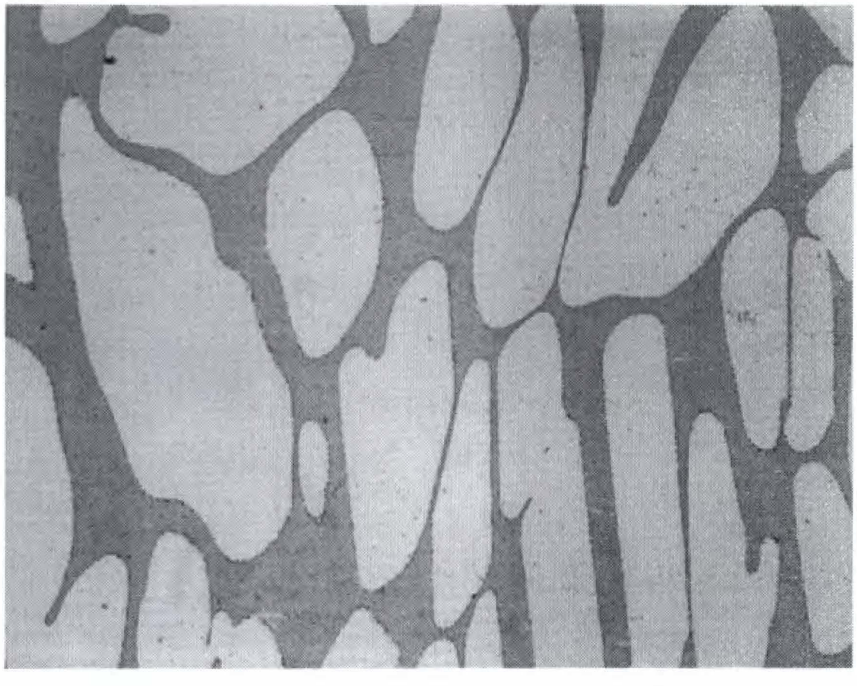


Figure 52. Microstructure of CD3-E-3, NaOH, 400x

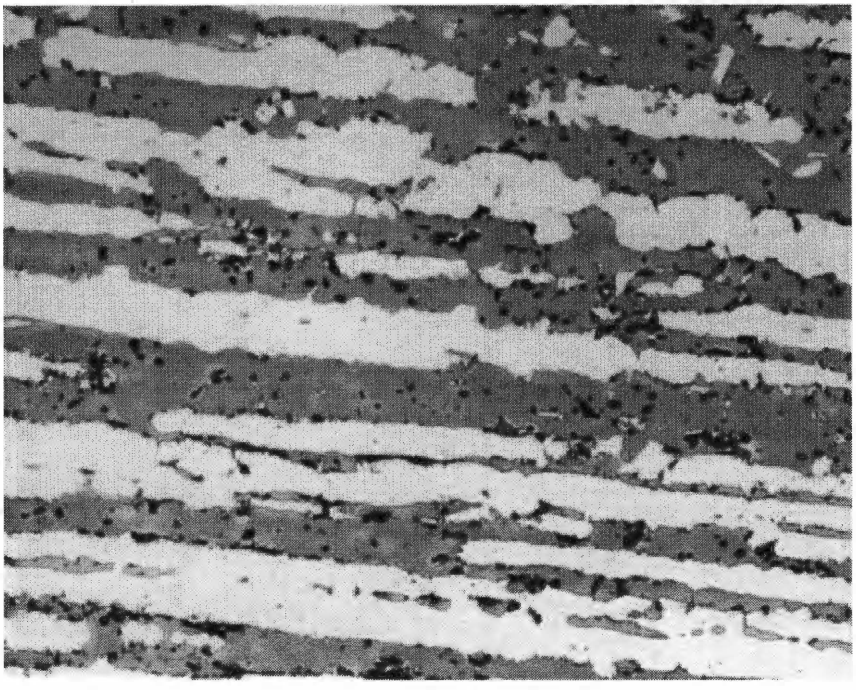


Figure 53. Microstructure of 2205-F-3, NaOH, 400x

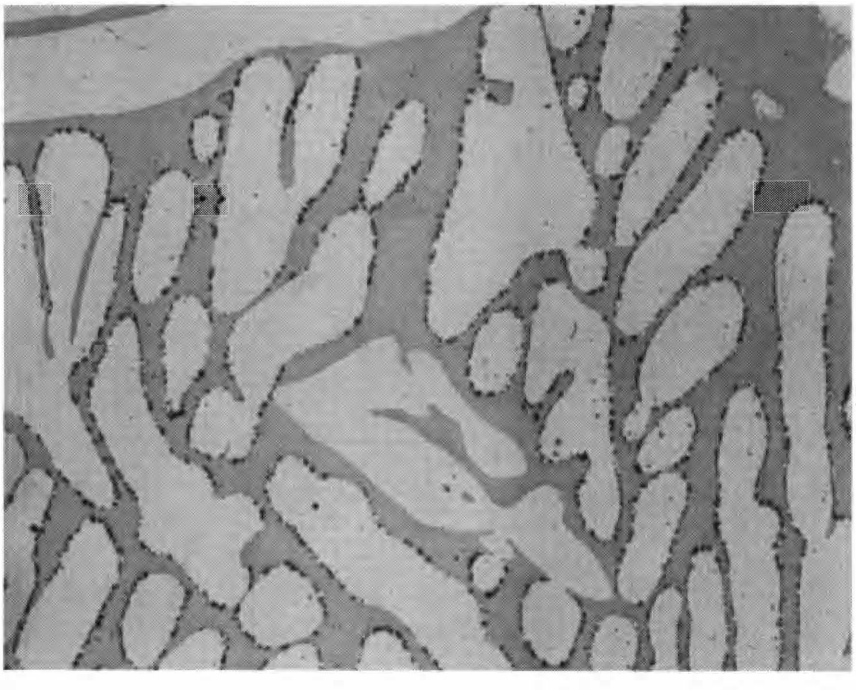


Figure 54. Microstructure of 41NCC-F-2, NaOH, 400x

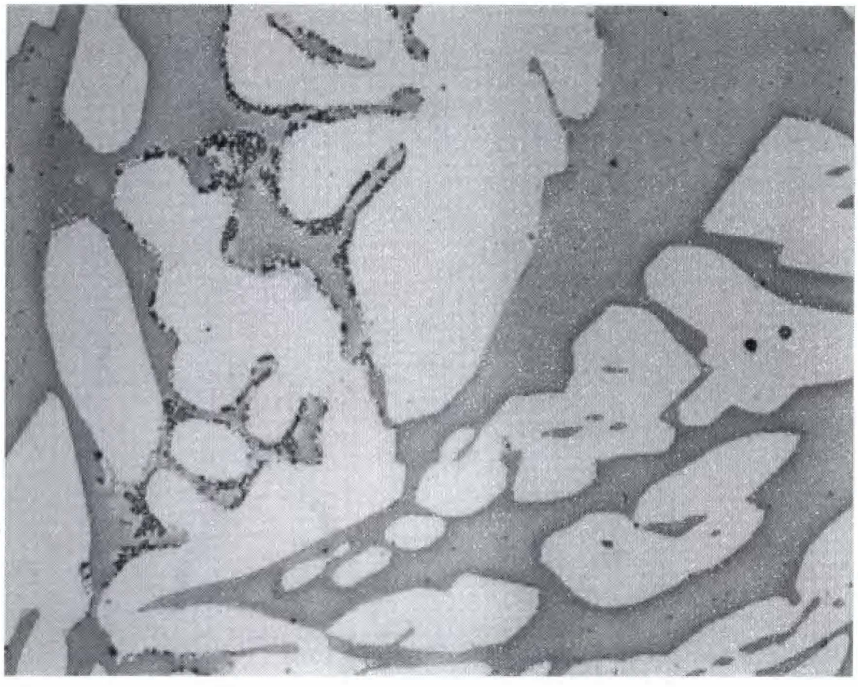


Figure 55. Microstructure of 42R-F-3, NaOH, 400x

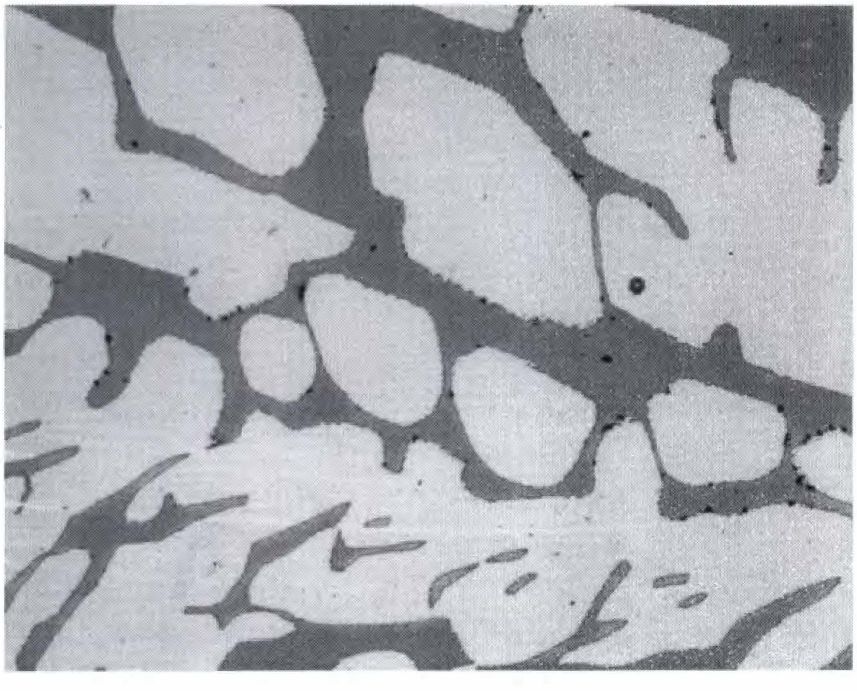


Figure 56. Microstructure of CD3-F-2, NaOH, 400x

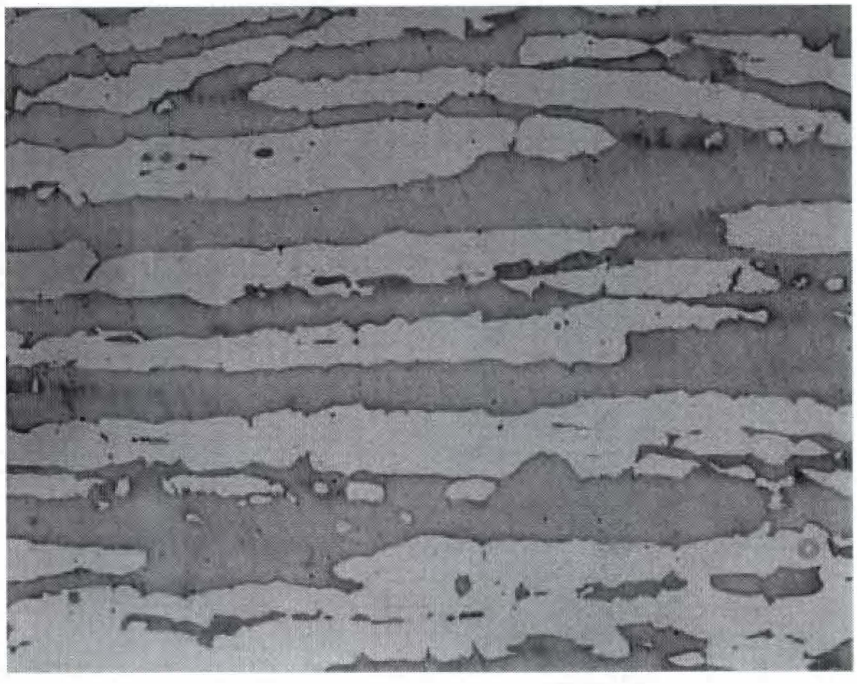


Figure 57. Microstructure of 2205-G-2, NaOH, 400x

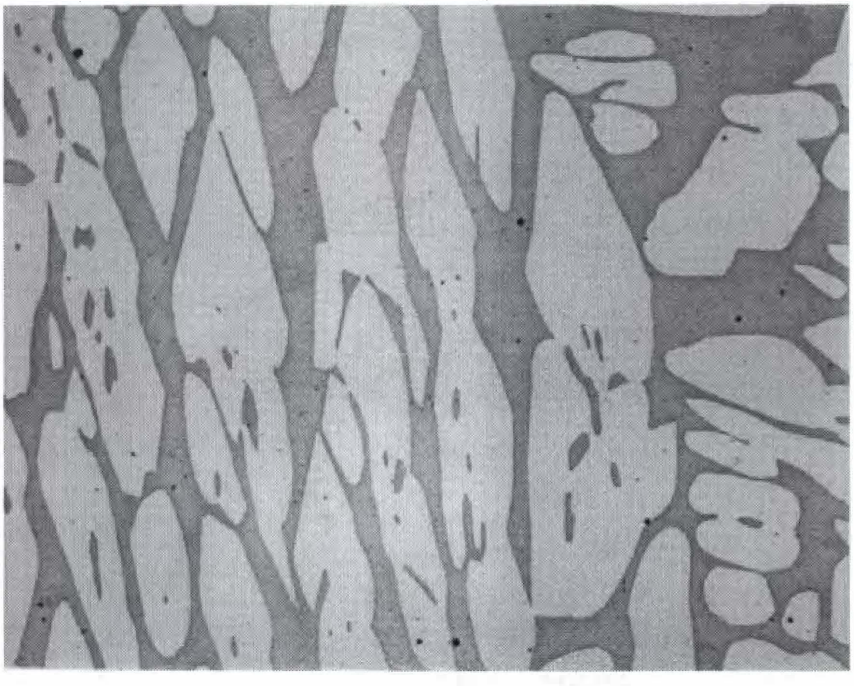


Figure 58. Microstructure of 41NCC-G-3, NaOH, 400x

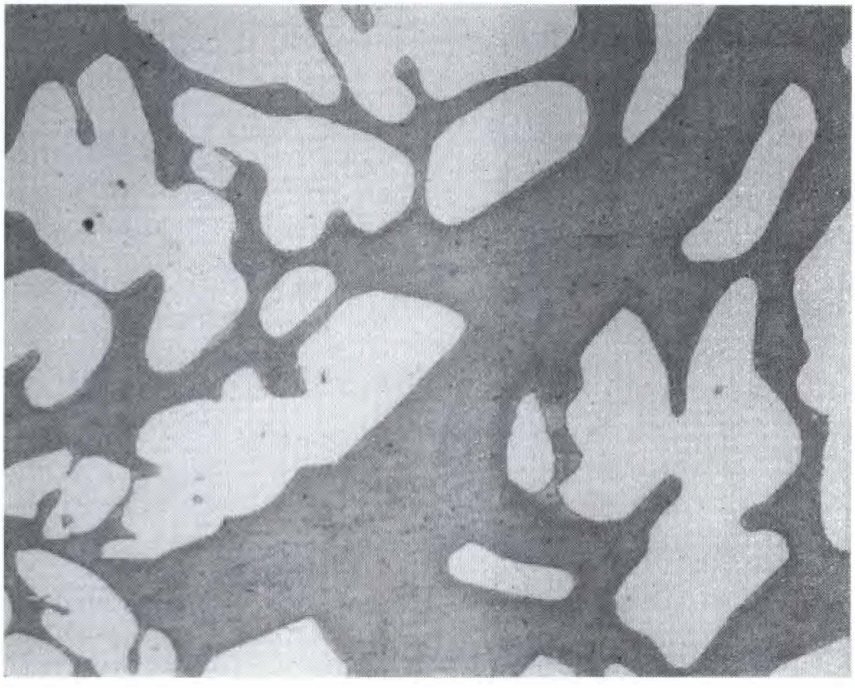


Figure 59. Microstructure of 42R-G-2, NaOH, 400x

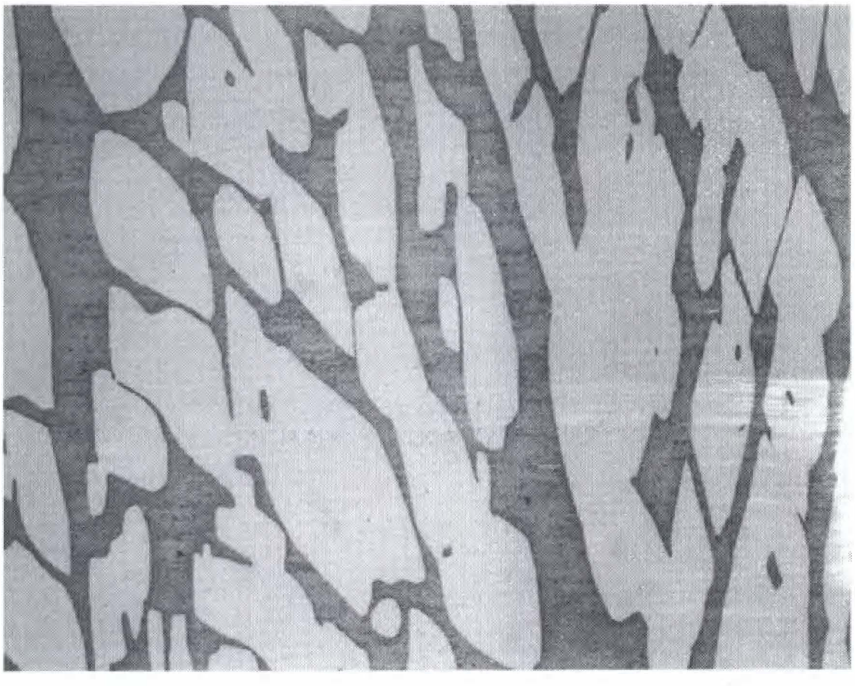


Figure 60. Microstructure of CD3-G-2, NaOH, 400x

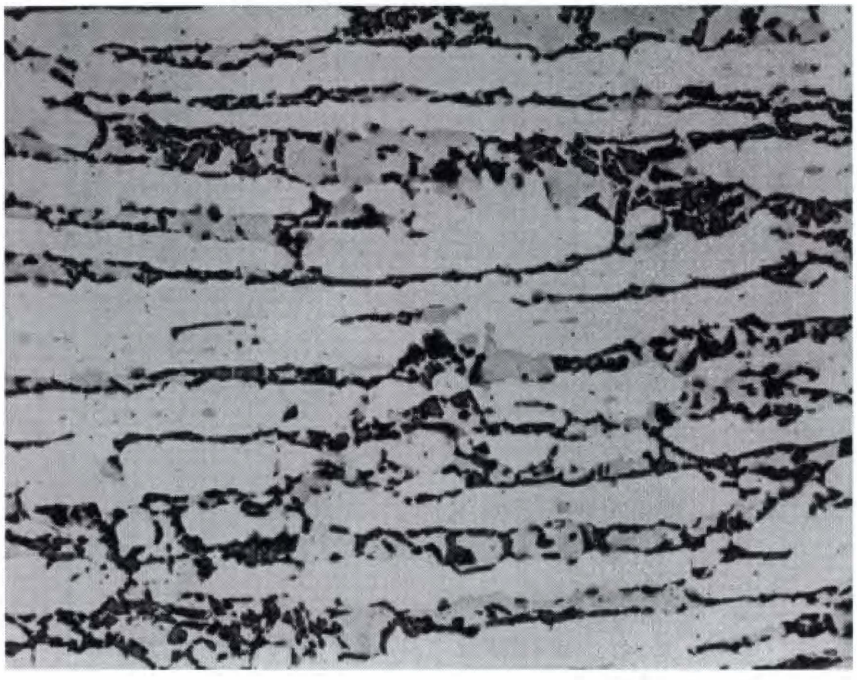


Figure 61. Microstructure of 2205-H-2, NaOH, 400x

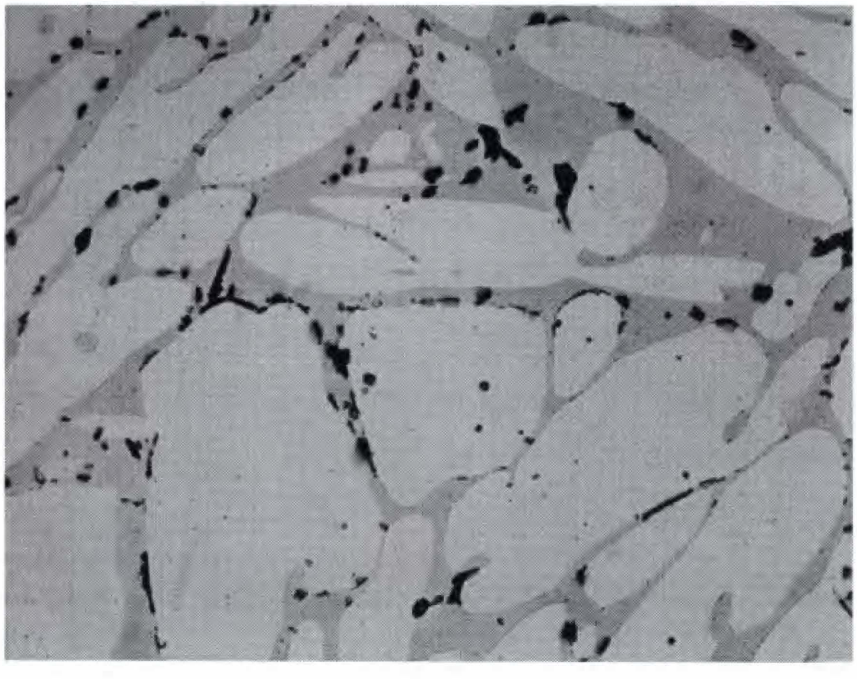


Figure 62. Microstructure of 41N-H-3, NaOH, 400x

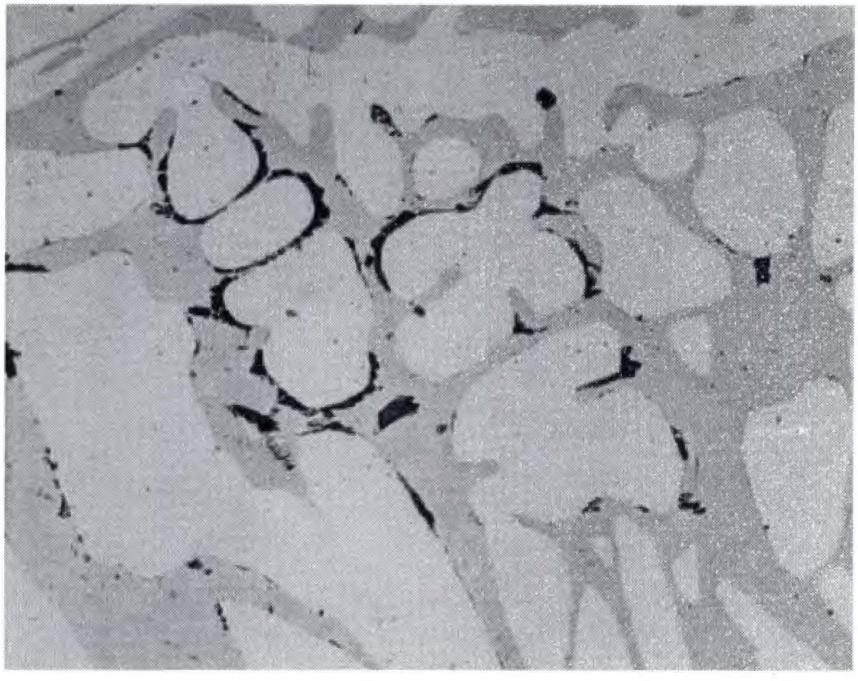


Figure 63. Microstructure of 42R-H-1, NaOH, 400x

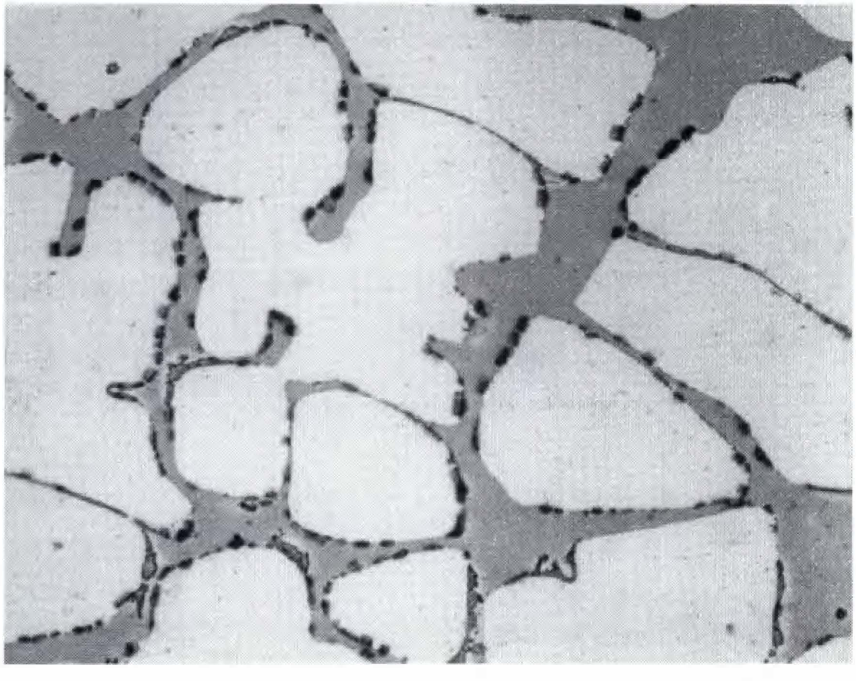


Figure 64. Microstructure of CD3-H-1, NaOH, 400x

Table 14. Corrosion Rates for ASTM A923 Study

Heat Treatment	Corrosion Rates (mdd)			
	2205	41NCC	42R	CD3
A Heat to 1950°F, Hold 30 min., Water Quench	0.0	0.0	0.0	1.9
B Heat to 1950°F, Hold 30 min., Water Quench, Heat to 1550°F, Water Quench	10.0	0.0	4.0	15.2
C Heat to 1950°F, Hold 30 min., Water Quench, Heat to 1550°F, Hold 5 min., Water Quench	6.5	0.0	0.0	7.2
D Heat to 1950°F, Hold 30 min., Water Quench, Heat to 1550°F, Hold 10 min., Water Quench	30.4	8.5	3.8	2.6
E Heat to 1950°F, Hold 30 min., Water Quench, Heat to 1550°F, Hold 15 min., Water Quench	5.9	23.7	2.0	45.8
F Heat to 1950°F, Hold 30 min., Water Quench, Heat to 1550°F, Hold 20 min., Water Quench	39.5	58.8	3.9	28.2
G Heat to 1950°F, Hold 30 min., Air Cool	1.0	6.9	0.0	5.1
H Heat to 1950°F, Hold 30 min., Slow Cool	3510.5	1438.5	176.9	566.5

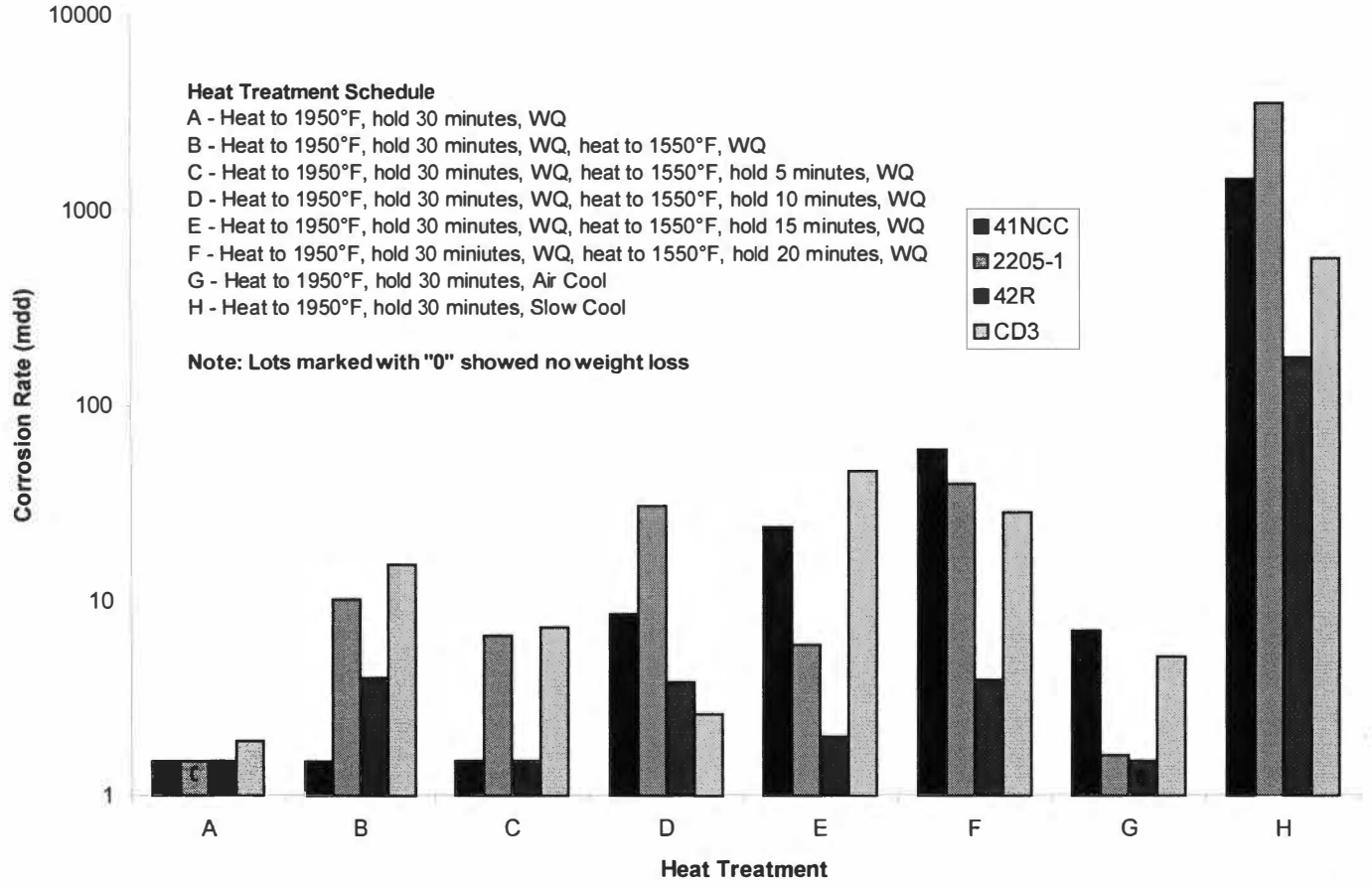


Figure 65. Corrosion Rates for ASTM A923 Study

The impact toughness of cast and wrought DSS materials subjected to the 2-stage heat treatments (solution anneal @ 1950°F + hold @ 1550°F) and other than rapid quenching (air cool & slow cool from 1950°F) was dramatically reduced. The 2-stage heat treatment, "B" (figures 8-11), shows a very fine waviness along the austenite/ferrite boundaries, which is identified as a possibly affected structure. The toughness of the material subjected to this heat treatment shows a sharp drop in impact toughness. This indicates that toughness of the material is affected even with the slightest amount of intermetallic phase precipitation. Figures 8-27, for the 2 stage heat treatments, show that the intermetallic phase precipitation increases as a function of hold time at 1550°F, which leads to further decrease in impact toughness of the materials. From the results it can be concluded that ASTM A923 Method B impact testing is the most sensitive of the 3 ASTM A923 methods for detecting the presence of intermetallic phases. Method B is readily reproducible within the accuracy required for the detection of intermetallic phases [1], however it is the most costly and time-consuming method to perform due to the precise machining required for impact test specimens.

ASTM A923 Method A etch testing is adequate for detection of the presence of intermetallic phases, however this method introduces operator bias as it requires greater skill to interpret the results. Method A etch testing does not easily distinguish between an unaffected structure (no intermetallic phases present) and a partially affected structure (slight traces of intermetallic phases present), whereas Method B impact testing detects the slightest formation of intermetallic phases with a marked decrease in impact toughness. As intermetallic phase precipitation increased, there was not a predictable

trend in ASTM A923 Method C weight loss. However, large differences in intermetallic phase precipitation, such as the difference between heat treatment "A" (figures 4-7) and "H" (figures 32-35) produced a significant difference in weight loss. It can be concluded that the weight loss of the materials was not as severely affected and was not as predictable with respect to intermetallic phase precipitation as the impact toughness. ASTM A923 Methods A and C cannot be recommended as a stand-alone test for the detection of intermetallic phases, leading to property degradation.

Heat Treatment "G" (figures 28-31) showed no presence of intermetallic phase or loss of corrosion performance per ASTM A923 Methods A and C. However, the Charpy impact toughness, as measured per ASTM A923 Method B, was dramatically lower than other heat treatments that showed no presence of intermetallic phase or loss of corrosion performance, such as heat treatment "A". This may indicate that other factors influence the loss in impact toughness or that the impact toughness test detects the earliest formation of intermetallic phases.

ASTM A923 Method A & C Round Robin Study

Test Method A

Table 15 summarizes the classification of the etch structure. Figures 66-105 show the microstructure examined, as supplied by each participant.

Test Method C

Table 16 shows the results from the ferric chloride weight loss test.

Table 15. Classification of Etch Structure

Material ID	Participant	Figure #	Classification of Etch Structure
41NCC-A-1	1	66	Unaffected
	2	67	Unaffected
	3	68	Unaffected
	4	69	Possibly Affected
	5	70	Unaffected
41NCC-B-3	1	71	Unaffected
	2	72	Unaffected
	3	73	Unaffected
	4	74	Possibly Affected
	5	75	Unaffected
41NCC-C-2	1	76	Affected
	2	77	Affected
	3	78	Possibly Affected
	4	79	Possibly Affected
	5	80	Possibly Affected
41NCC-D-1	1	81	Affected
	2	82	Affected
	3	83	Affected
	4	84	Affected
	5	85	Affected
41NCC-E-2	1	86	Affected
	2	87	Affected
	3	88	Affected
	4	89	Affected
	5	90	Affected
41NCCF-1	1	91	Affected
	2	92	Affected
	3	93	Affected
	4	94	Affected
	5	95	Affected
41NCC-G-1	1	96	Unaffected
	2	97	Unaffected
	3	98	Unaffected
	4	99	Unaffected
	5	100	Unaffected
41NCC-H-1	1	101	Affected
	2	102	Affected
	3	103	Affected
	4	104	Affected
	5	105	Affected

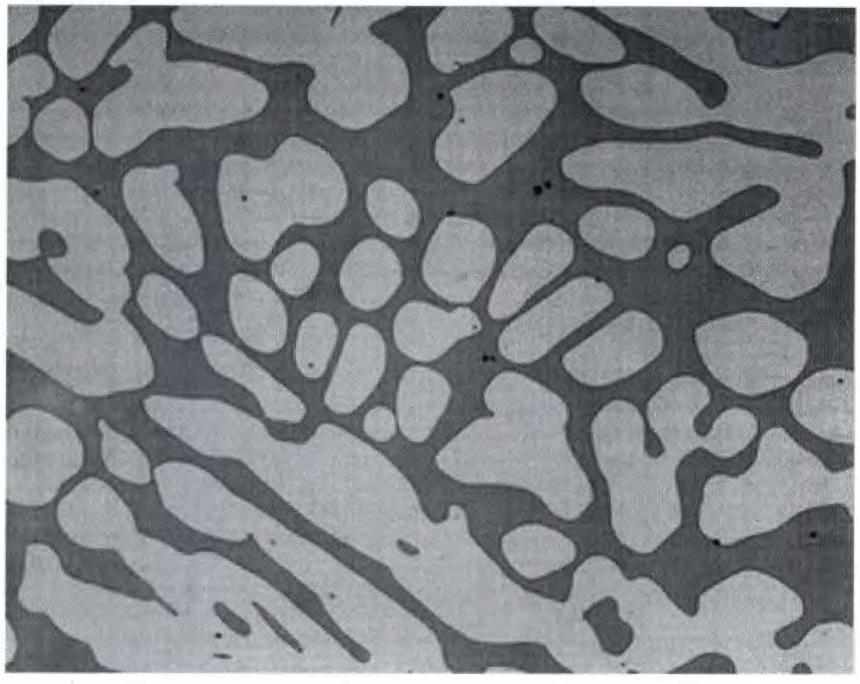


Figure 66. Microstructure of 41NCC-A-1, NaOH, 400x, Participant 1



Figure 67. Microstructure of 41NCC-A-1, NaOH, 400x, Participant 2

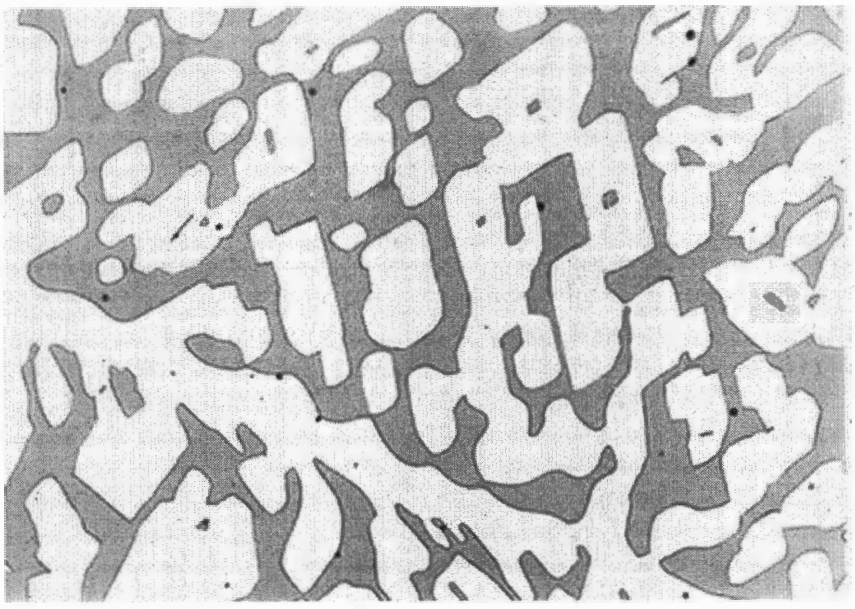


Figure 68. Microstructure of 41NCC-A-1, NaOH, 500x, Participant 3

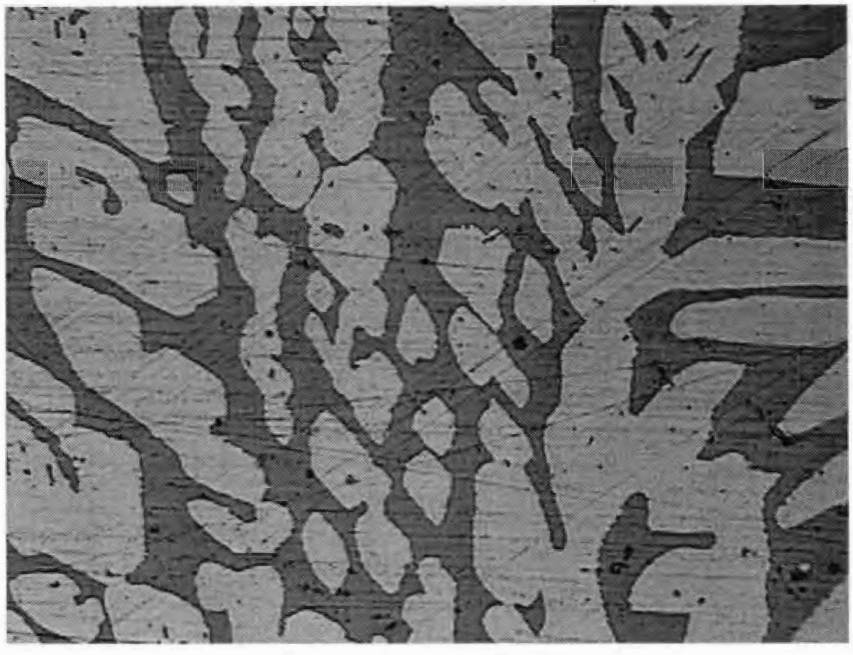


Figure 69. Microstructure of 41NCC-A-1, NaOH, 500x, Participant 4



Figure 70. Microstructure of 41NCC-A-1, NaOH, 400x, Participant 5

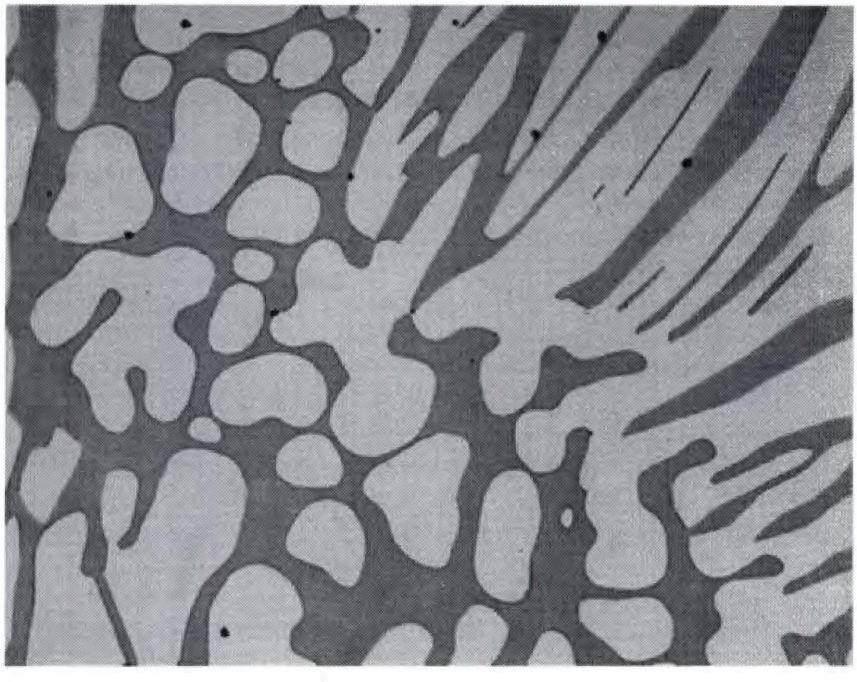


Figure 71. Microstructure of 41NCC-B-3, NaOH, 400x, Participant 1

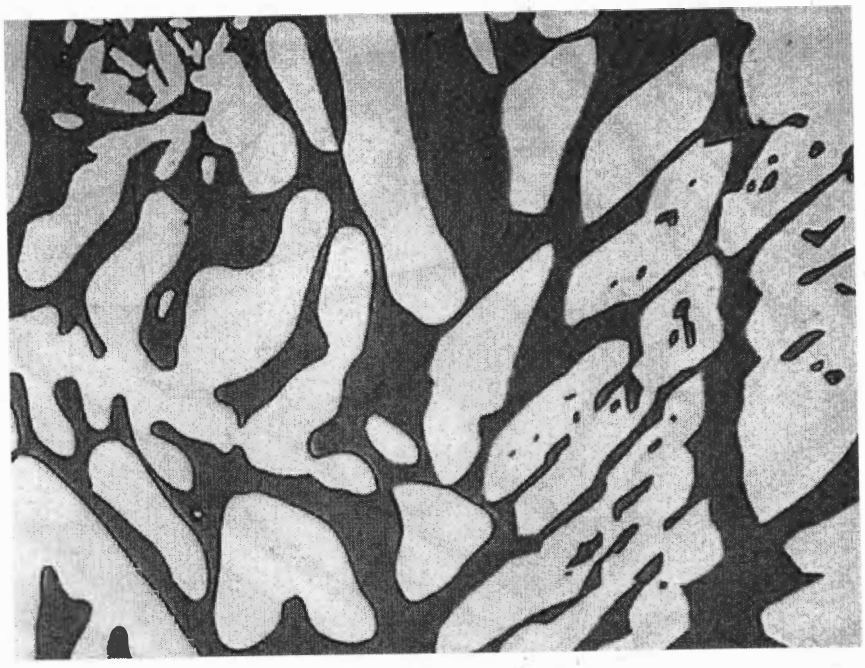


Figure 72. Microstructure of 41NCC-B-3, NaOH, 400x, Participant 2

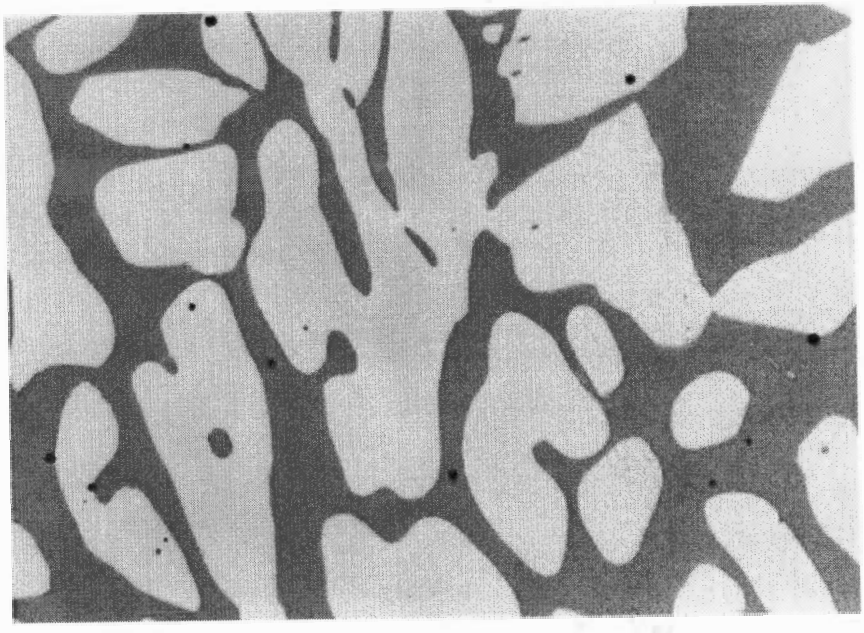


Figure 73. Microstructure of 41NCC-B-3, NaOH, 500x, Participant 3

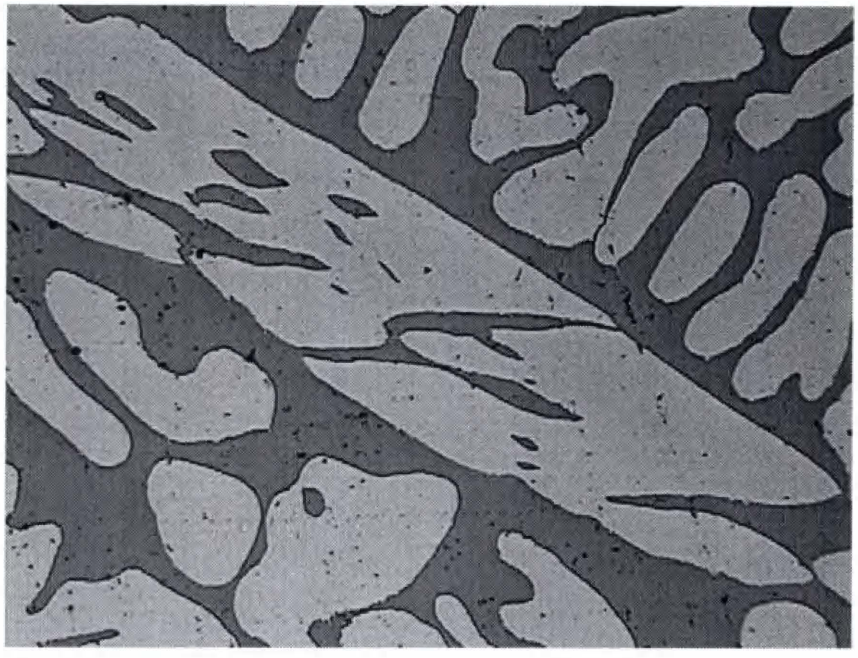


Figure 74. Microstructure of 41NCC-B-3, NaOH, 500x, Participant 4

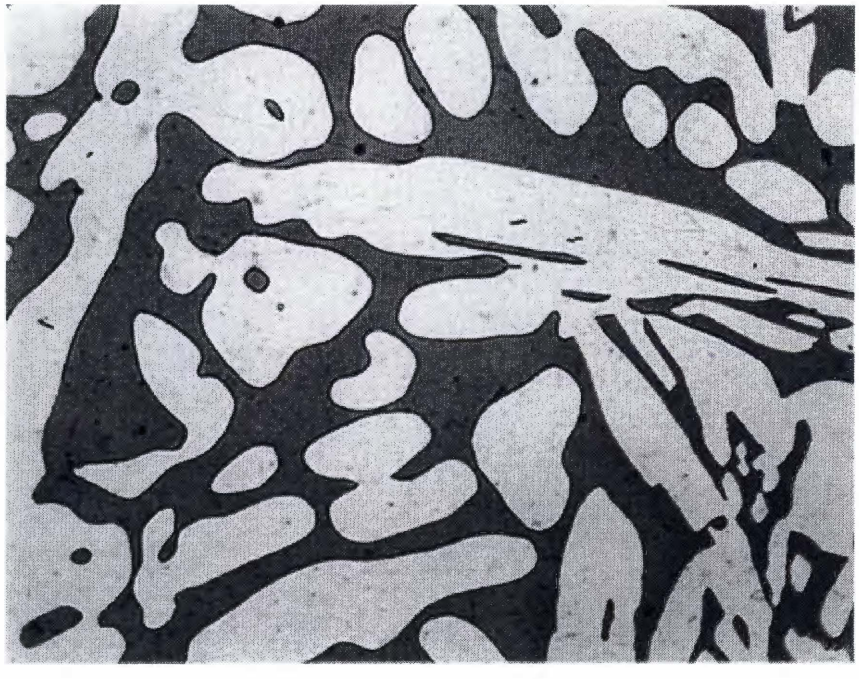


Figure 75. Microstructure of 41NCC-B-3, NaOH, 400x, Participant 5

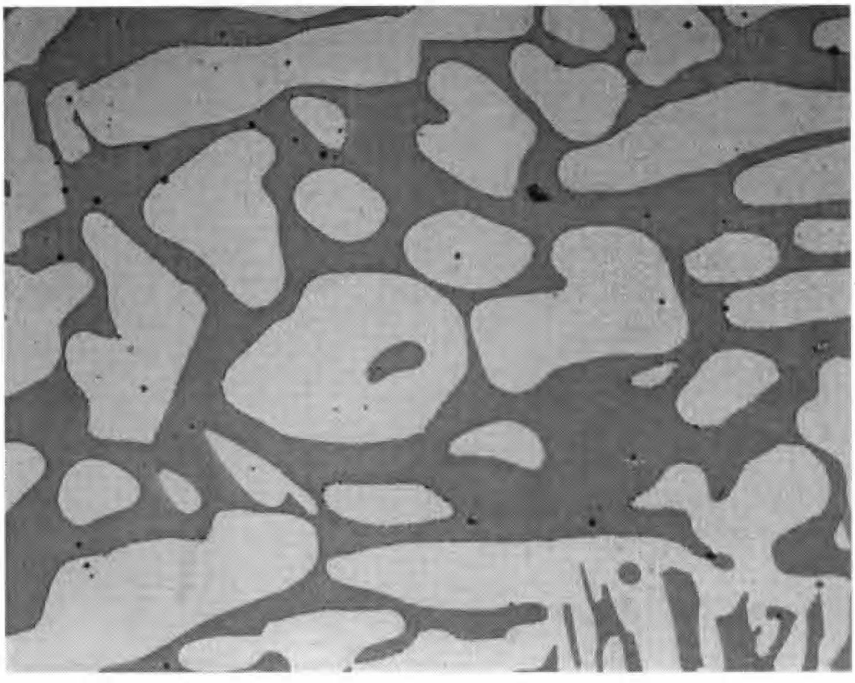


Figure 76. Microstructure of 41NCC-C-2, NaOH, 400x, Participant 1

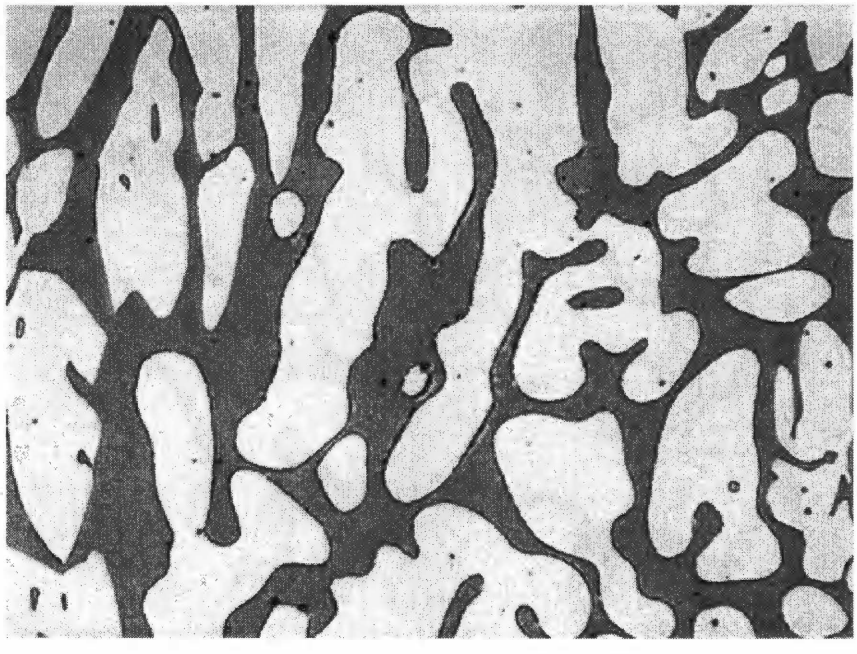


Figure 77. Microstructure of 41NCC-C-2, NaOH, 400x, Participant 2

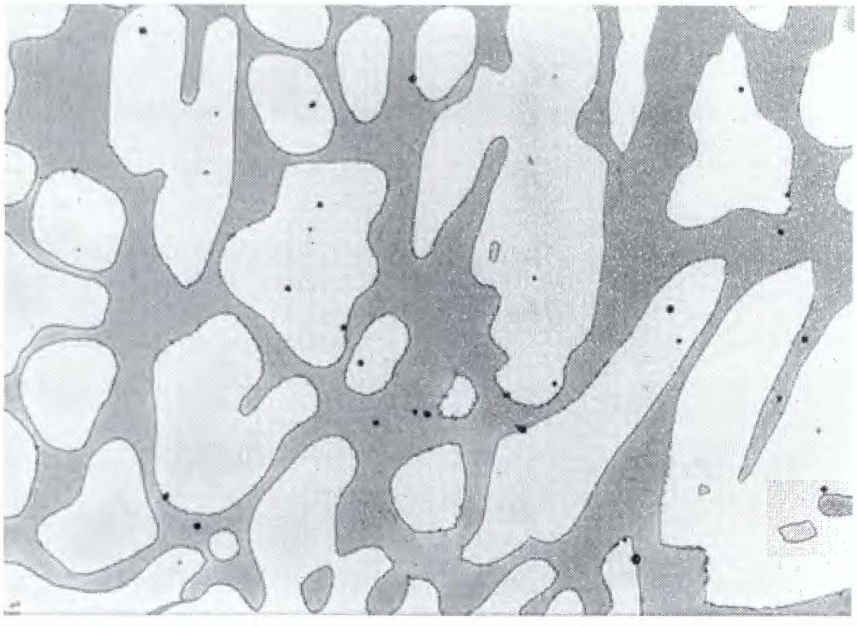


Figure 78. Microstructure of 41NCC-C-2, NaOH, 500x, Participant 3

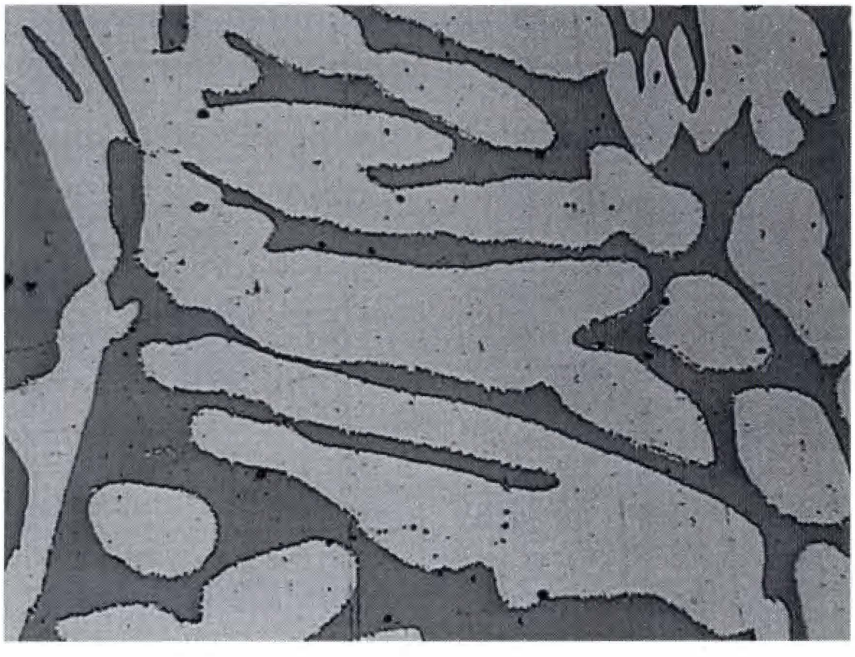


Figure 79. Microstructure of 41NCC-C-2, NaOH, 500x, Participant 4

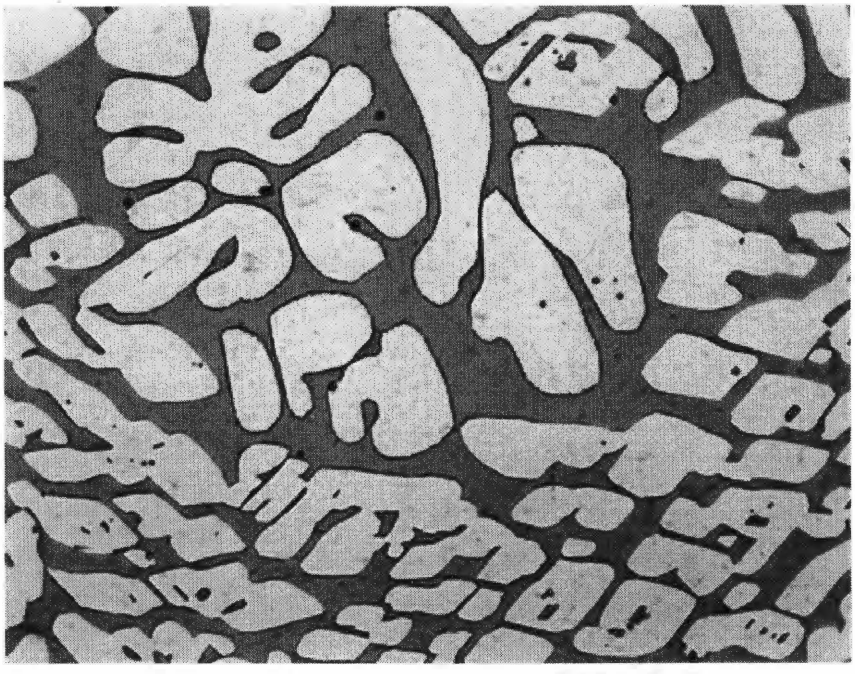


Figure 80. Microstructure of 41NCC-C-2, NaOH, 400x, Participant 5

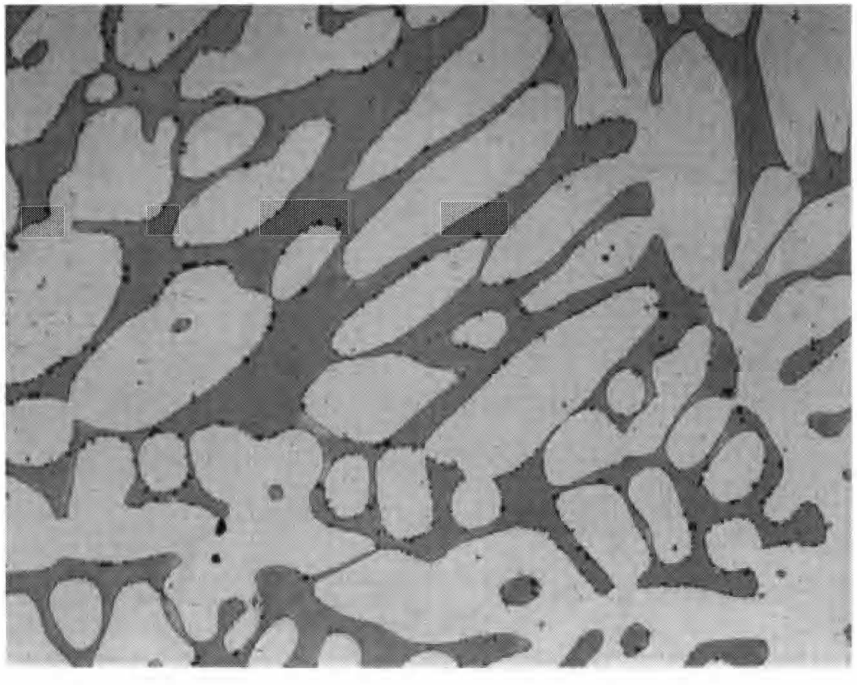


Figure 81. Microstructure of 41NCC-D-1, NaOH, 400x, Participant 1

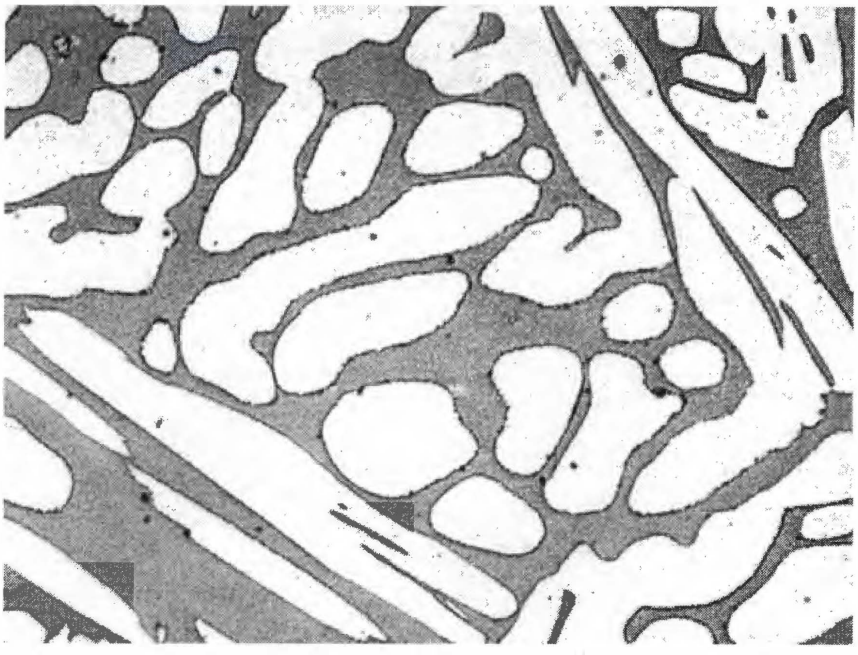


Figure 82. Microstructure of 41NCC-D-1, NaOH, 400x, Participant 2

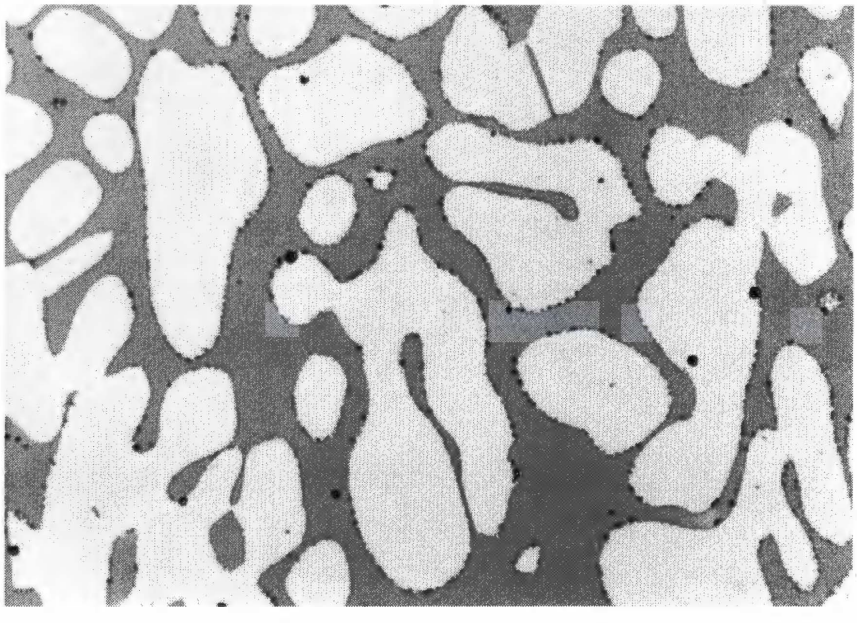


Figure 83. Microstructure of 41NCC-D-1, NaOH, 500x, Participant 3

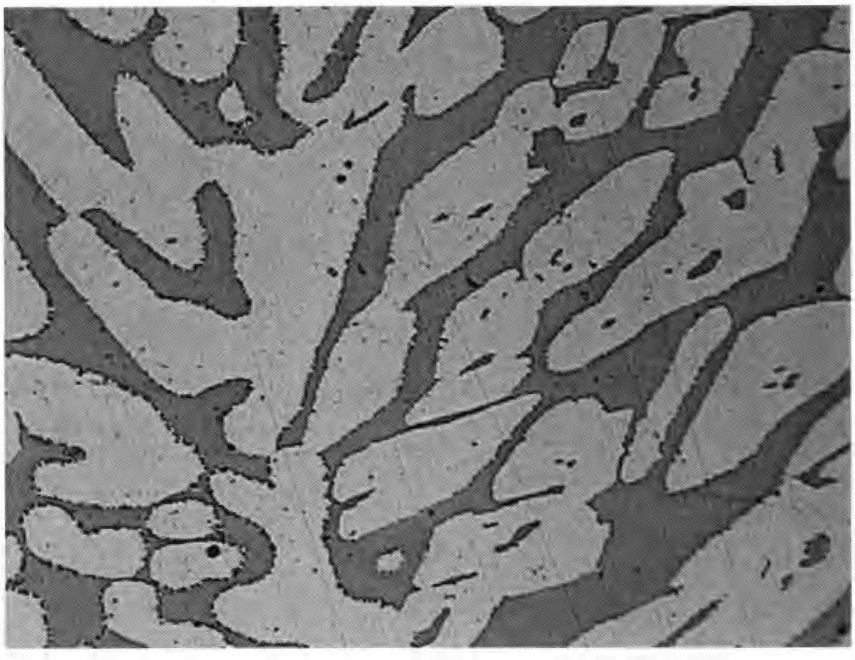


Figure 84. Microstructure of 41NCC-D-1, NaOH, 500x, Participant 4

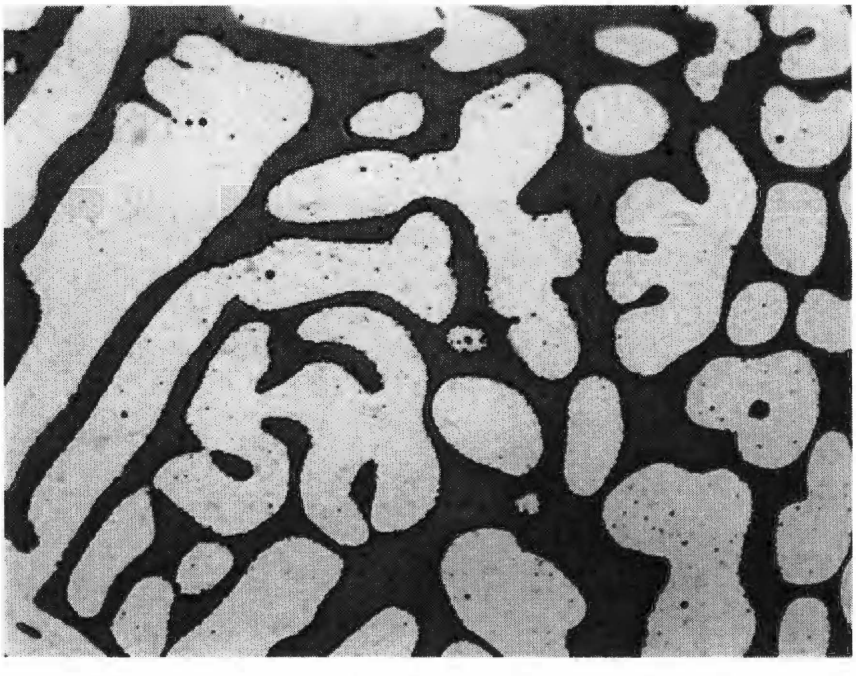


Figure 85. Microstructure of 41NCC-D-1, NaOH, 400x, Participant 5

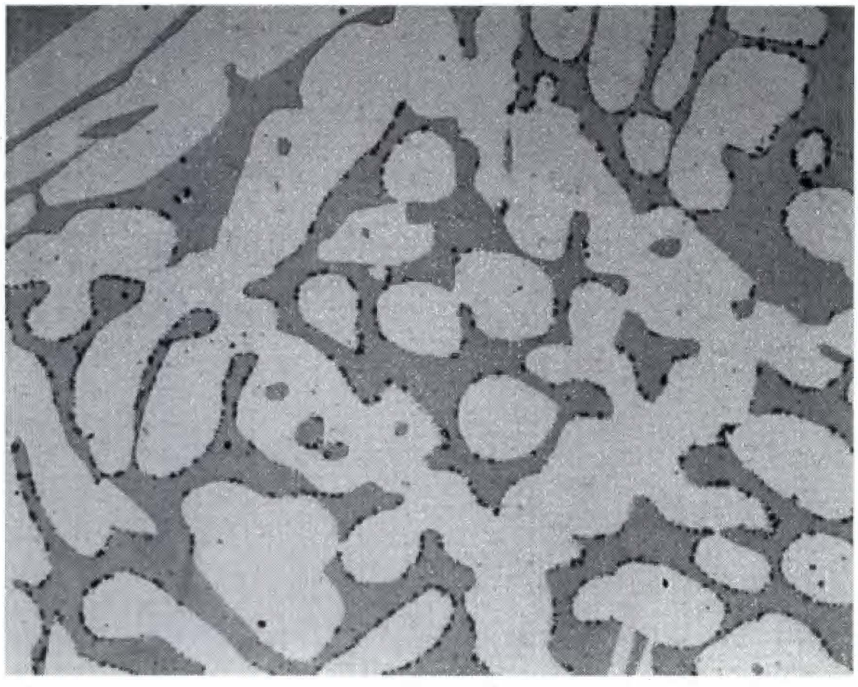


Figure 86. Microstructure of 41NCC-E-2, NaOH, 400x, Participant 1

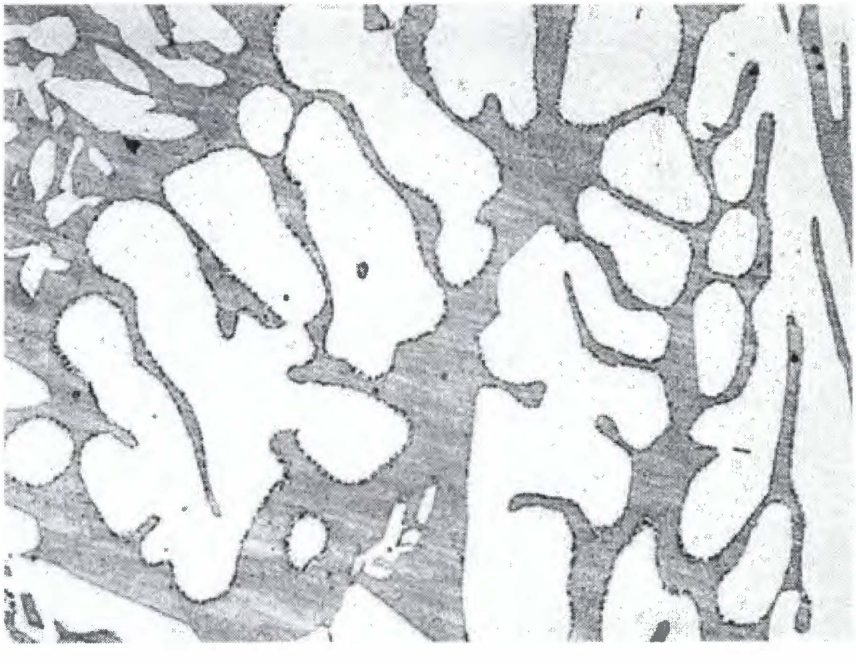


Figure 87. Microstructure of 41NCC-E-2, NaOH, 400x, Participant 2

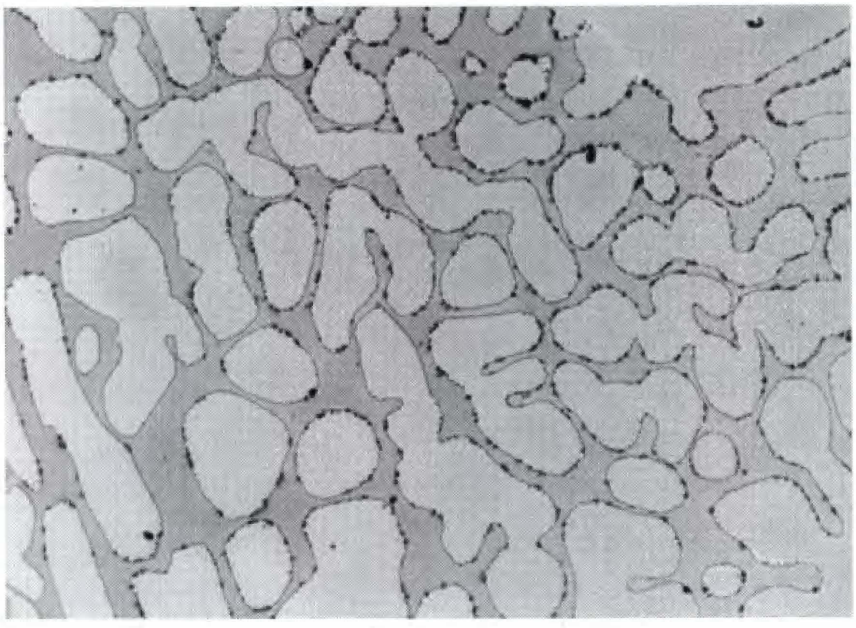


Figure 88. Microstructure of 41NCC-E-2, NaOH, 500x, Participant 3

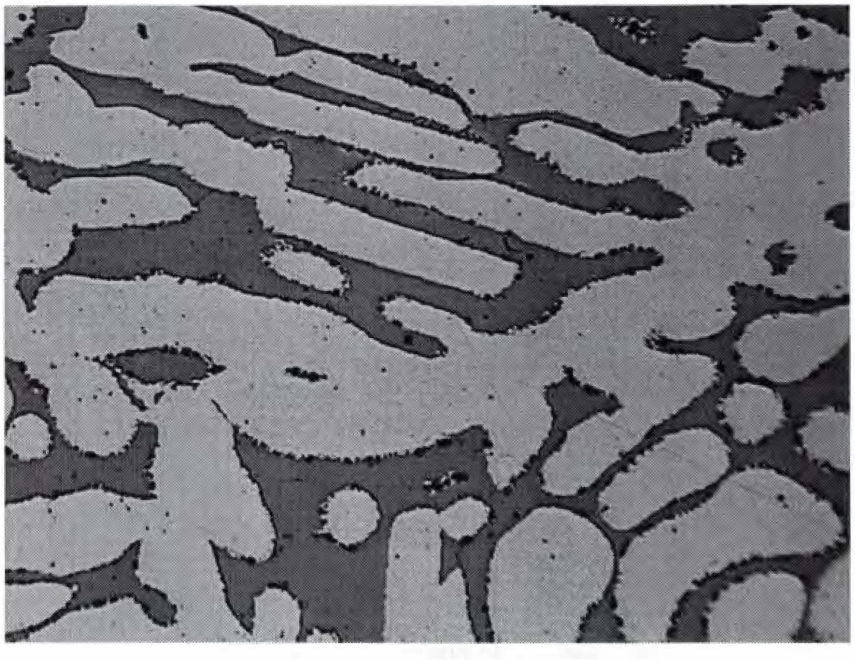


Figure 89. Microstructure of 41NCC-E-2, NaOH, 500x, Participant 4



Figure 90. Microstructure of 41NCC-E-2, NaOH, 400x, Participant 5

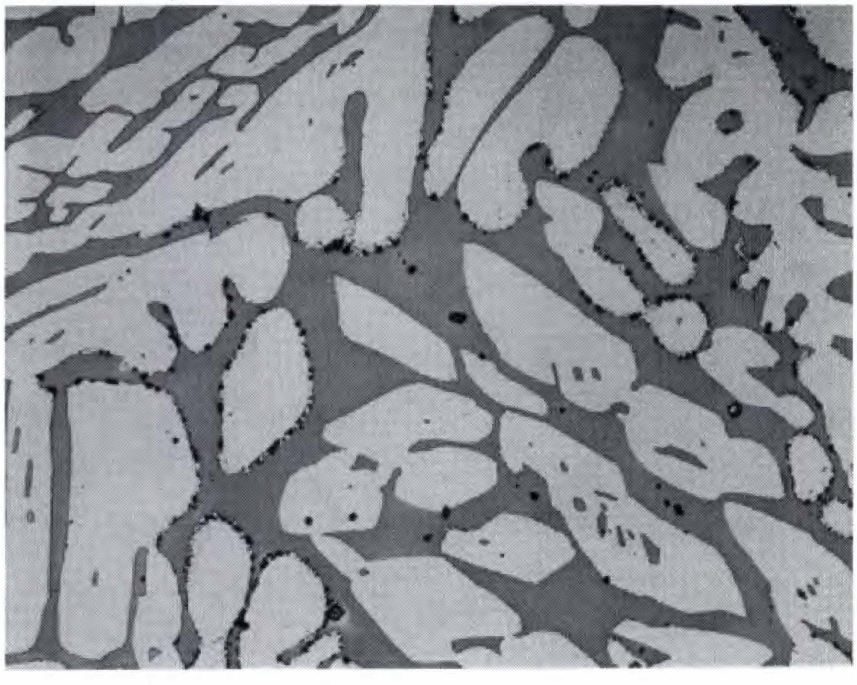


Figure 91. Microstructure of 41NCC-F-1, NaOH, 400x, Participant 1

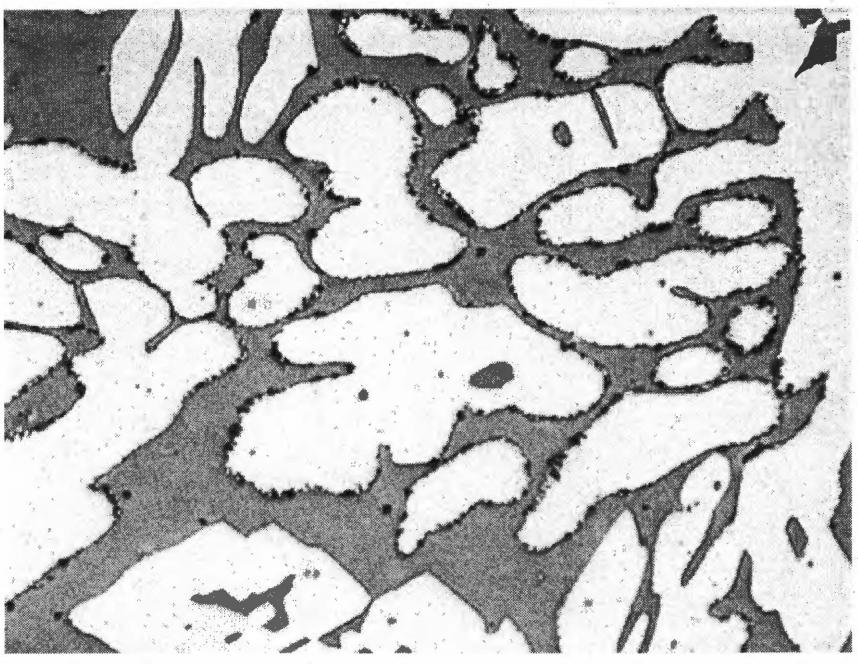


Figure 92. Microstructure of 41NCC-F-1, NaOH, 400x, Participant 2

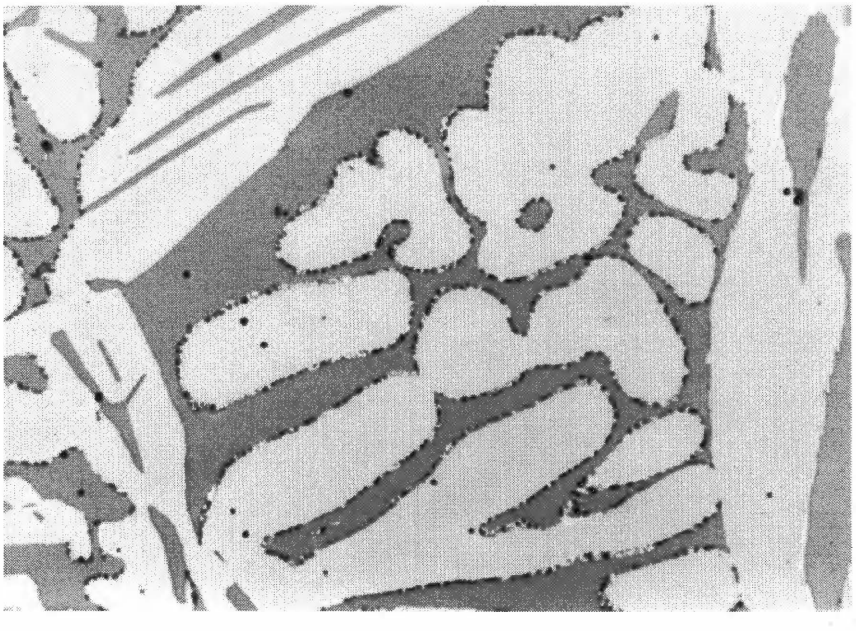


Figure 93. Microstructure of 41NCC-F-1, NaOH, 500x, Participant 3



Figure 94. Microstructure of 41NCC-F-1, NaOH, 500x, Participant 4



Figure 95. Microstructure of 41NCC-F-1, NaOH, 400x, Participant 5

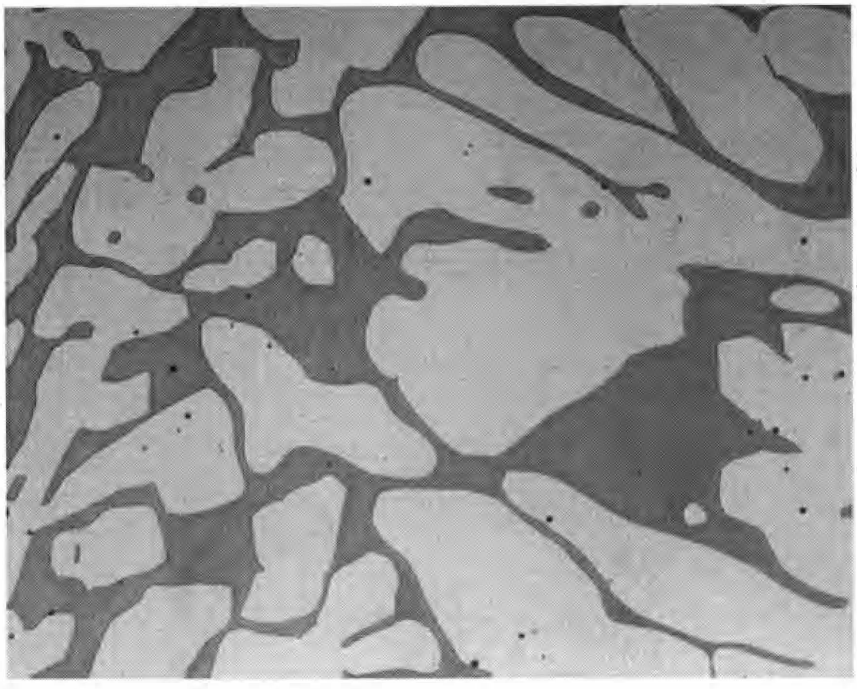


Figure 96. Microstructure of 41NCC-G-1, NaOH, 400x, Participant 1

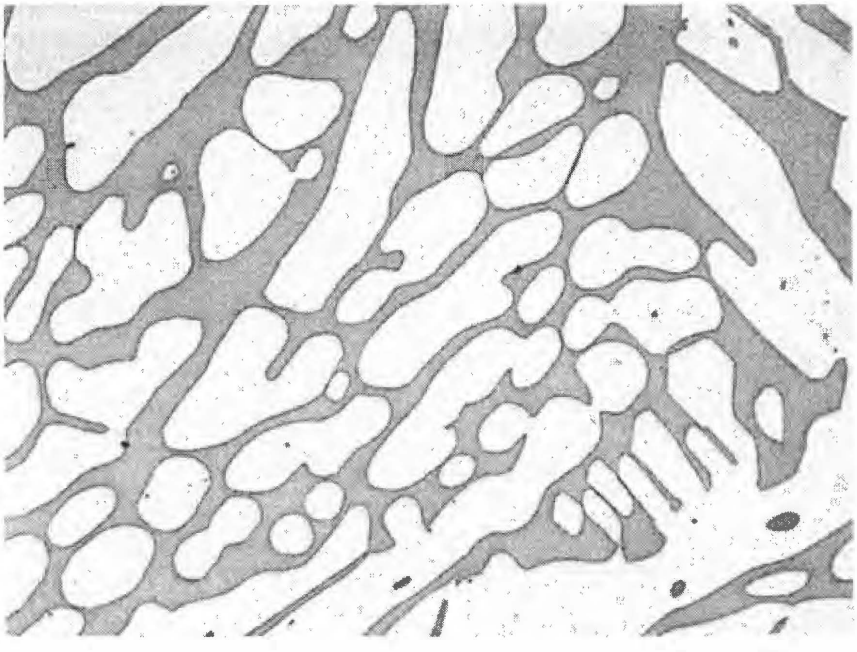


Figure 97. Microstructure of 41NCC-G-1, NaOH, 400x, Participant 2

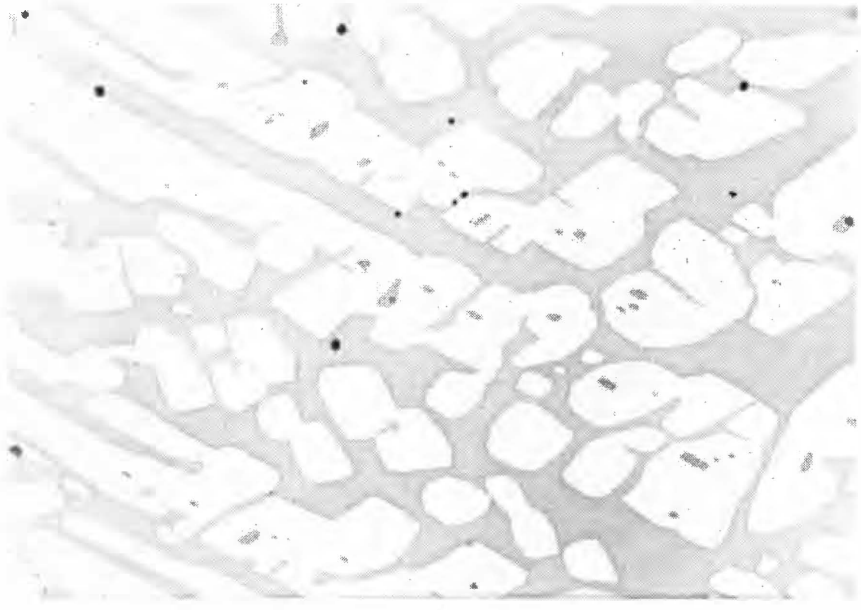


Figure 98. Microstructure of 41NCC-G-1, NaOH, 500x, Participant 3

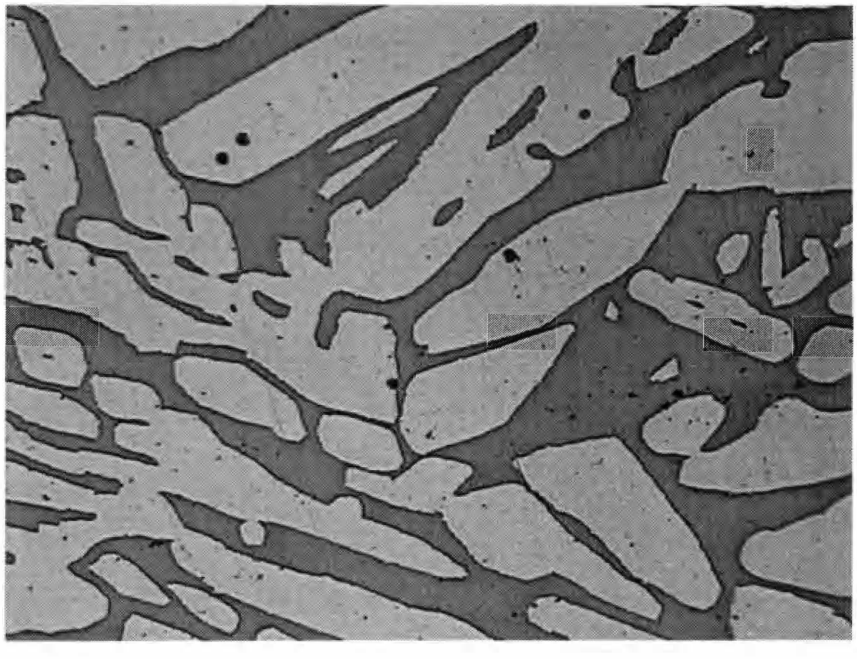


Figure 99. Microstructure of 41NCC-G-1, NaOH, 500x, Participant 4



Figure 100. Microstructure of 41NCC-G-1, NaOH, 400x, Participant 5

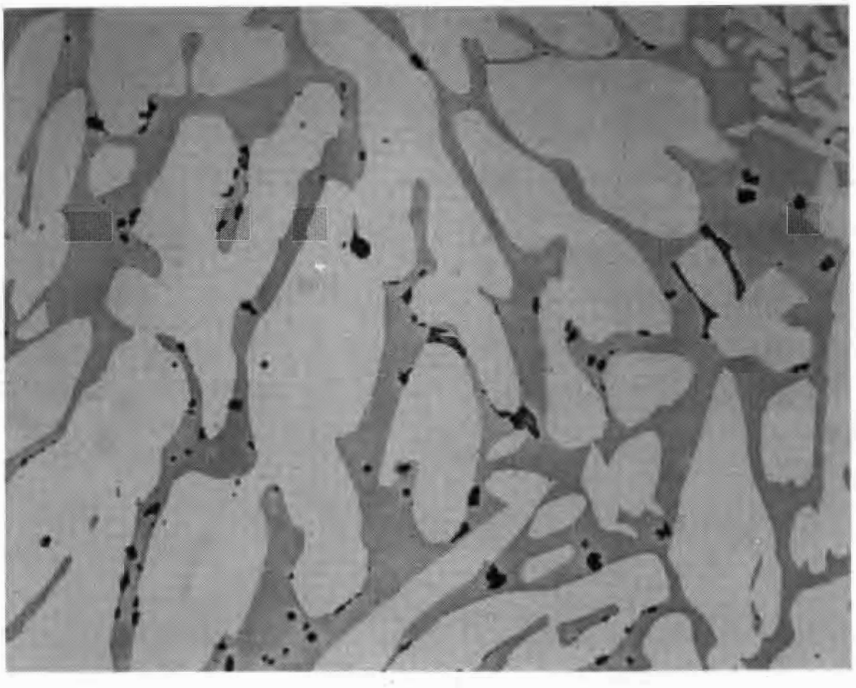


Figure 101. Microstructure of 41NCC-H-1, NaOH, 400x, Participant 1

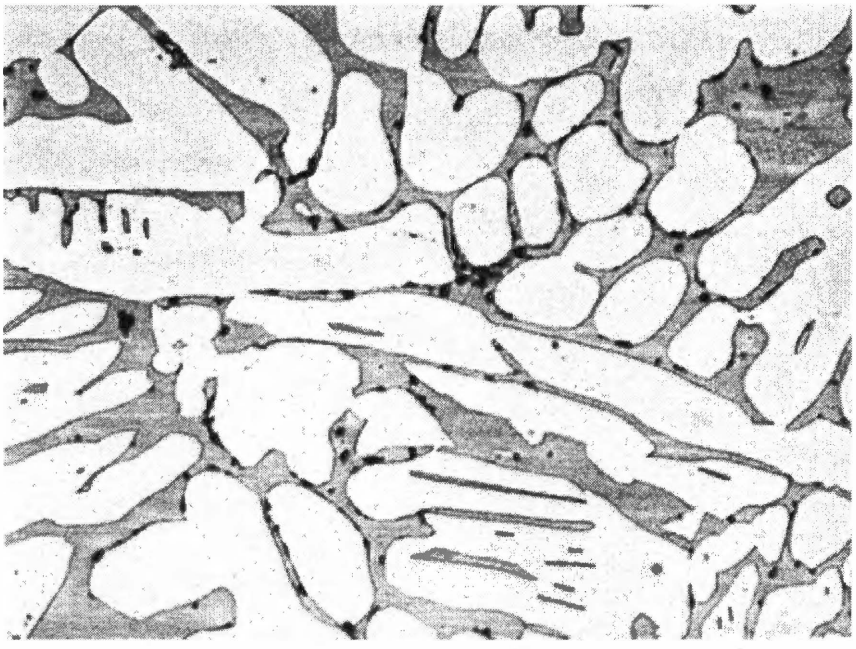


Figure 102. Microstructure of 41NCC-H-1, NaOH, 400x, Participant 2



Figure 103. Microstructure of 41NCC-H-1, NaOH, 500x, Participant 3

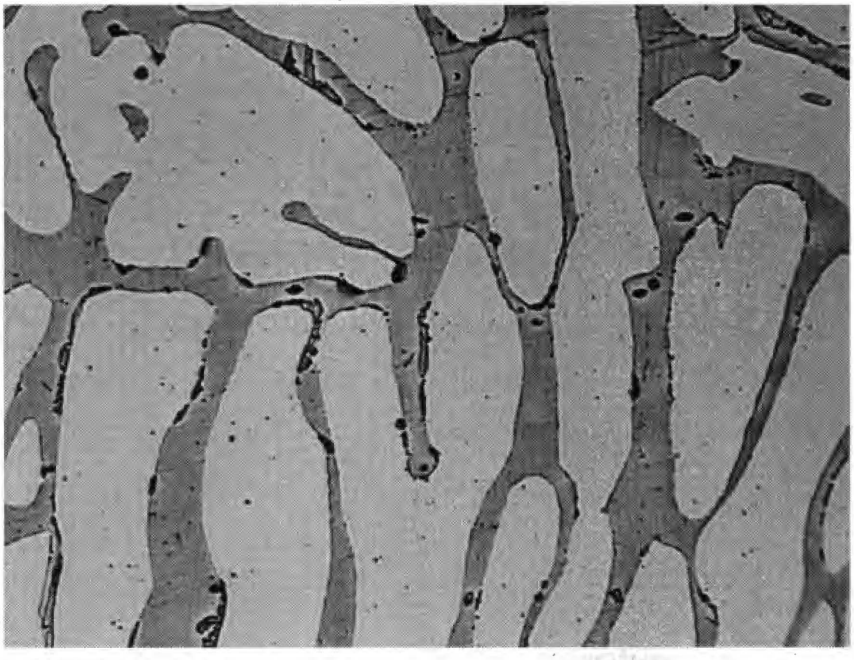


Figure 104. Microstructure of 41NCC-H-1, NaOH, 500x, Participant 4

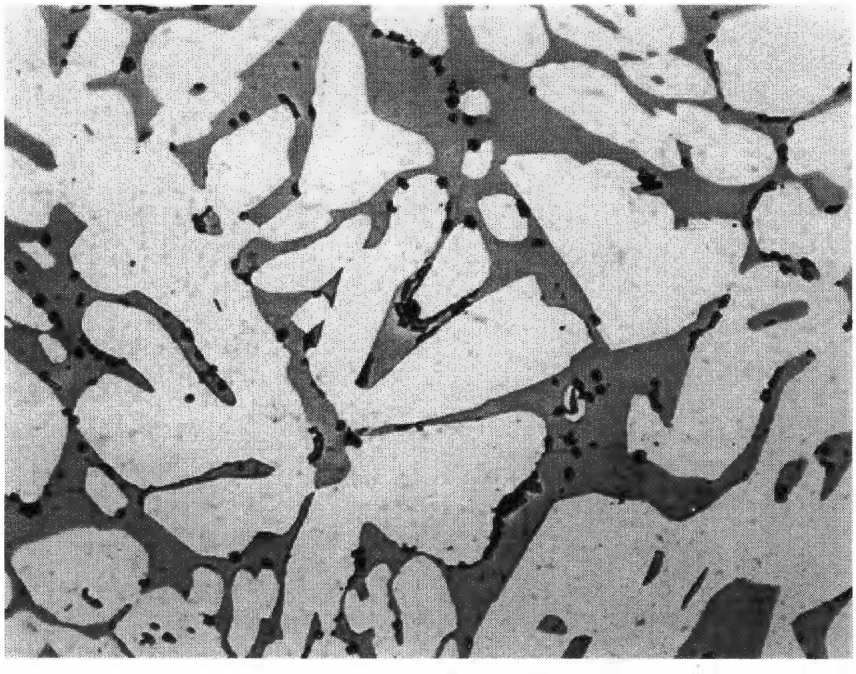


Figure 105. Microstructure of 41NCC-H-1, NaOH, 400x, Participant 5

Table 16. Corrosion Rates for ASTM A923 Round Robin Study

Material ID	Participant	Corrosion Rate (mdd)	Standard Deviation	95% Confidence Limit	Pass/Fail per ASTM A923 Criteria
41NCC-A	1	4.28			Pass
	2	0.00			Pass
	3	1.04	1.84	0.00-3.87	Pass
	4	0.00			Pass
	5	2.60			Pass
41NCC-B	1	1.06			Pass
	2	0.00			Pass
	3	0.00	1.79	0.00-3.66	Pass
	4	4.34			Pass
	5	1.77			Pass
41NCC-C	1	0.00			Pass
	2	1.03			Pass
	3	1.45	1.48	0.00-3.05	Pass
	4	0.00			Pass
	5	3.60			Pass
41NCC-D	1	4.13			Pass
	2	1.01			Pass
	3	2.02	1.53	0.00-3.68	Pass
	4	0.00			Pass
	5	1.77			Pass
41NCC-E	1	1.05			Pass
	2	3.07			Pass
	3	2.06	.737	1.01-2.84	Pass
	4	1.71			Pass
	5	1.74			Pass
41NCC-F	1	20.78			Fail
	2	18.17			Fail
	3	9.24	4.30	10.46-21.13	Pass
	4	15.21			Fail
	5	15.58			Fail
41NCC-G	1	0.00			Pass
	2	0.00			Pass
	3	2.05	.904	0.00-1.71	Pass
	4	0.00			Pass
	5	0.89			Pass
41NCC-H	1	541.54			Fail
	2	1055.72			Fail
	3	10.36	389	0.00-954.3	Fail
	4	259.48			Fail
	5	491.74			Fail

All participants identified the microstructure of 41NCC-A-1 and 41NCC-B-3 as "unaffected" except for participant 4 who identified the microstructure as "possibly affected". The microstructure 41NCC-C-2 was identified, by participants 1 and 2, as "affected", participants 3, 4, and 5 identified the microstructure as "possibly affected". The microstructures of 41NCC-D-1, 41NCC-E-2, 41NCC-F-1, and 41NCC-H-1 were identified by all participants as "affected". The microstructure of 41NCC-G-1 was identified by all participants as "unaffected". All materials identified as "possibly affected" or "affected" would have to pass ASTM A923 method B and method C in order to be qualified as acceptable. There is difficulty in determining the difference between an "unaffected" structure and "possibly affected" structure in cast DSS. However, it is no more difficult than distinguishing between an "unaffected" structure and "possibly affected" structure in wrought DSS.

41NCC-A, 41NCC-B, 41NCC-C, 41NCC-D, 41NCC-E, and 41NCC-G passed ASTM A923 method C per each participant. Participants 1, 2, 4, and 5 reported failure per method C for 41NCC-F, and passing per participant 3. All participants reported failure per method C for 41NCC-H. The standard deviation of less than 6% of the mean for each material by 5 participants shows that lab-to-lab results are predictable unless "high" amounts of intermetallic phases are present, such as in heat treatment H. ASTM A923 is sufficient for predicting corrosion performance of cast DSS because all microstructures listed as "unaffected" passed method C testing.

The results of this round robin study indicate that lab-to-lab reproducibility of cast DSS etch structures and corrosion performance is possible. ASTM A923 is sufficient to

detect the presence of detrimental intermetallic phases in cast DSS. The following photomicrographs, Figures 106 -109 are recommended for addition to ASTM A923 Method A for the classification of etch structures in cast DSS.

ASTM A923 Study of the Effectiveness of Existing Foundry Solution Annealing Procedures for Producing Cast DSS Without Intermetallic Phases

Test Method A

Table 17 summarizes the classification of the etch structure as determined from Method A. Figures 110-119 shows the microstructure for each lot.

Test Method B

Results of the impact toughness for a number of Charpy bars from heat of the foundry solution annealed castings are shown in Table 18 and average impact toughness for each heat is shown in Figure 120.

Test Method C

The corrosion rates per Method C are summarized in Table 19.

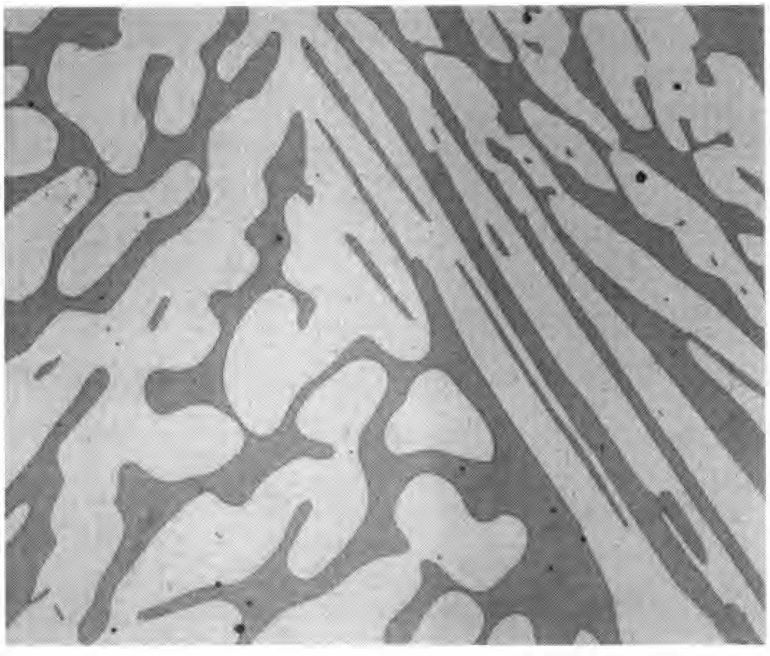


Fig. 106 Unaffected Structure, No Evidence of Intermetallic Phase, NaOH, 400x

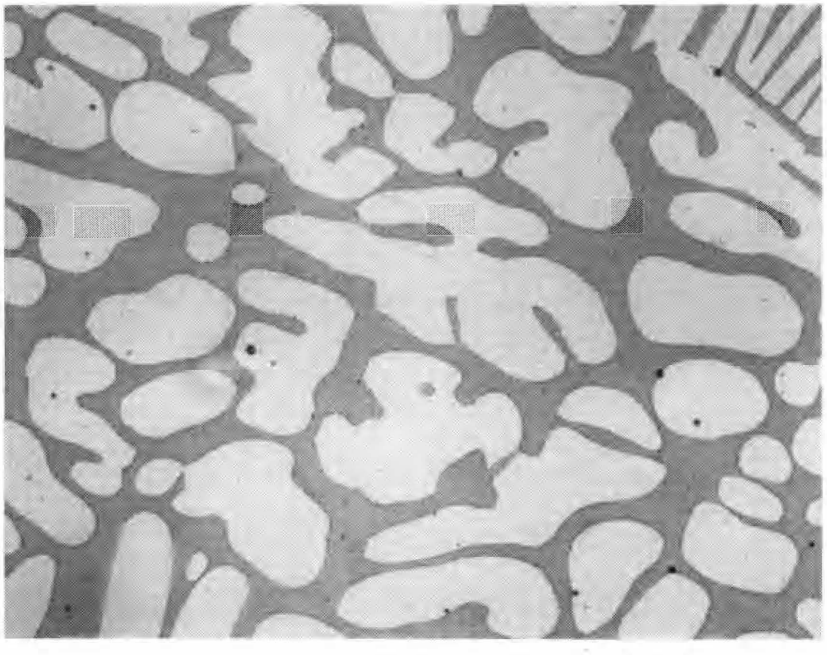


Fig. 107 Possibly Affected Structure, Interphase Boundaries Show Fine Waviness, NaOH, 400x

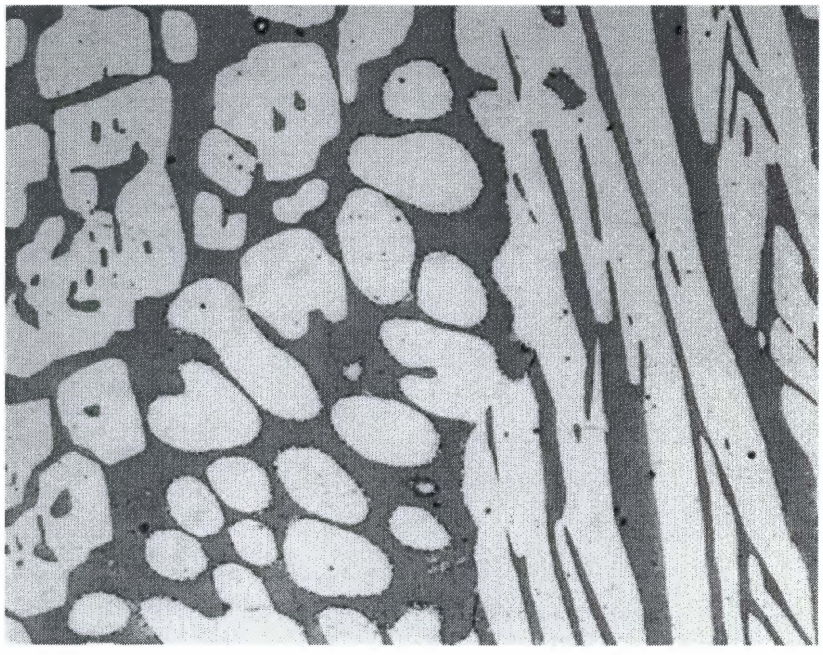


Fig. 108. Affected Structure 1, Intermetallic Phase is Evident, NaOH 400x

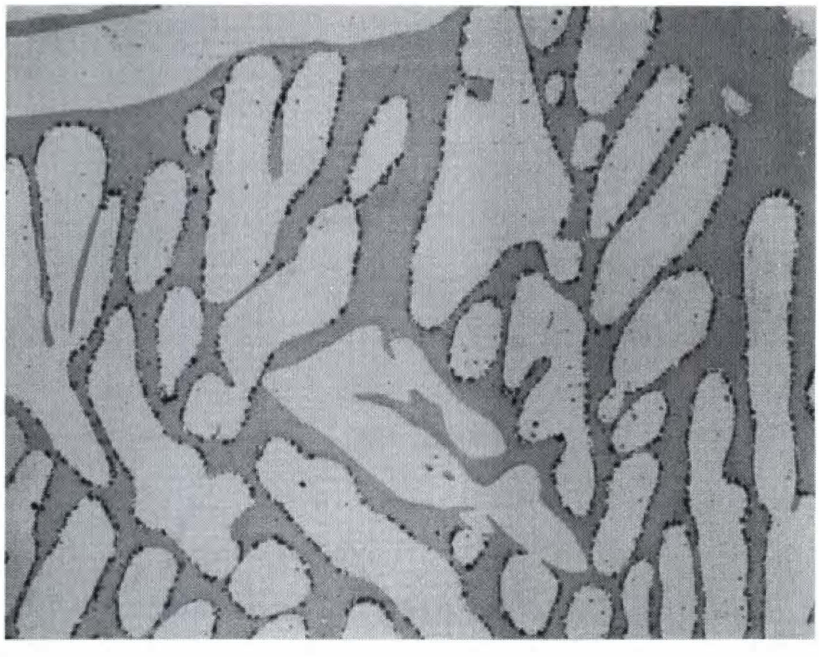


Fig 109. Affected Structure 2, Intermetallic Phase is Evident, NaOH, 400x

Table 17. Classification of Etch Structure for Foundry Solution Anneal Study

Material ID	Classification of Etch Structure
4A-SA-1	Unaffected Structure
4A-SA-2	Unaffected Structure
4A-SA-3	Unaffected Structure
4A-SA-4	Unaffected Structure
4A-SA-6	Unaffected Structure
4A-SA-7	Unaffected Structure
4A-SA-8	Unaffected Structure
4A-SA-9	Unaffected Structure
4A-SA-10	Unaffected Structure
4A-SA-11	Unaffected Structure

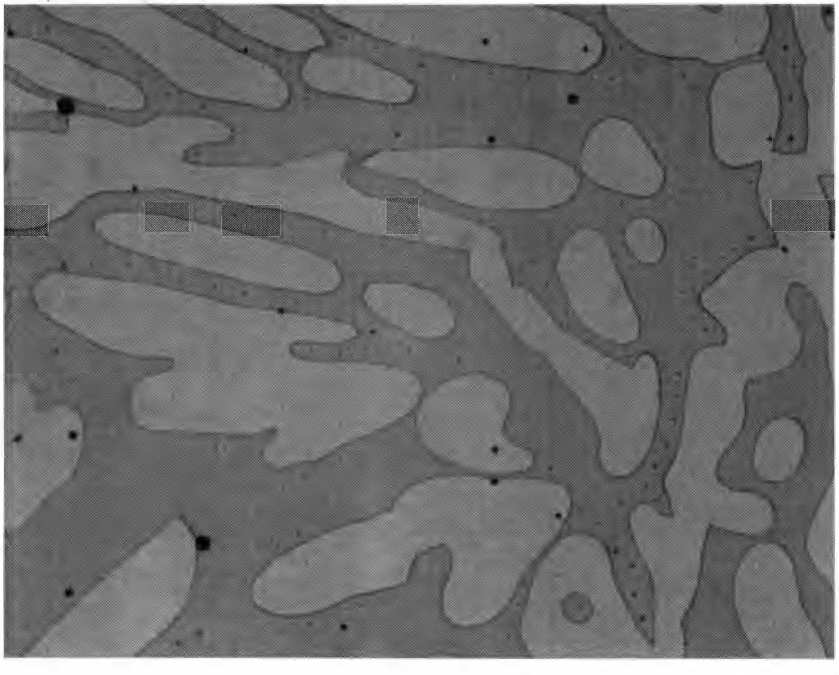


Figure 110. Microstructure of 4A-SA-1, NaOH, 400x

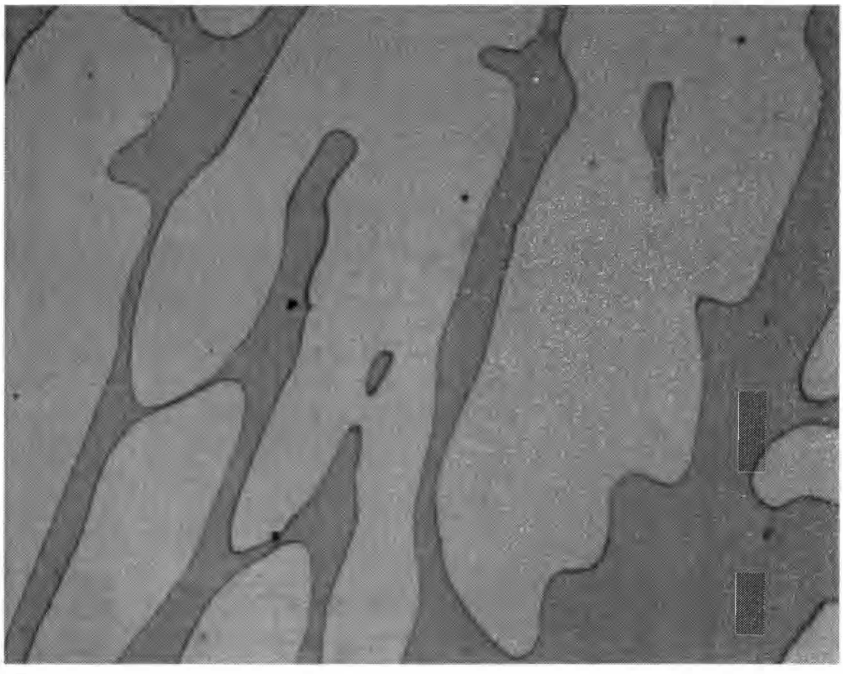


Figure 111. Microstructure of 4A-SA-2, NaOH, 400x

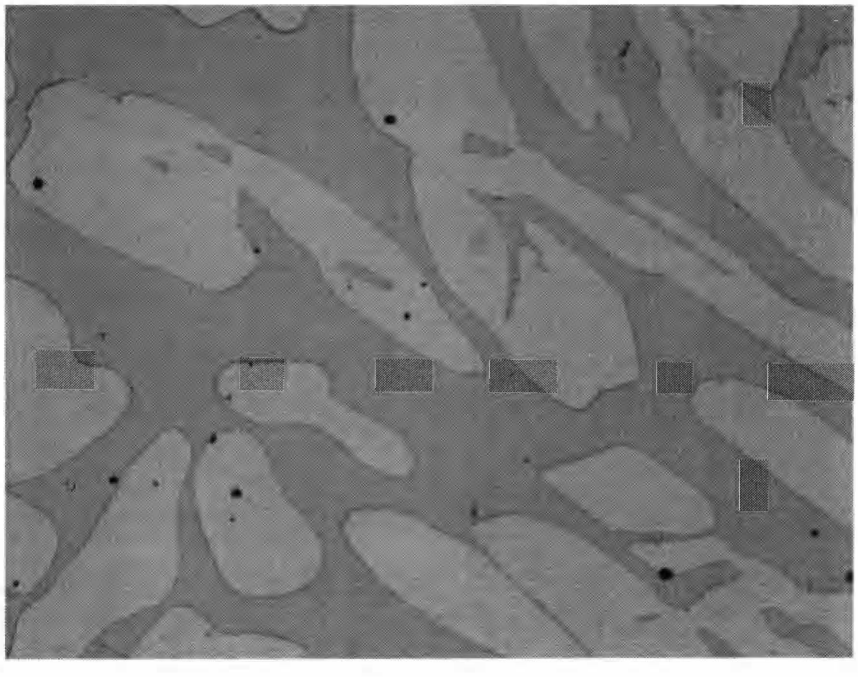


Figure 112. Microstructure of 4A-SA-3, NaOH, 400x

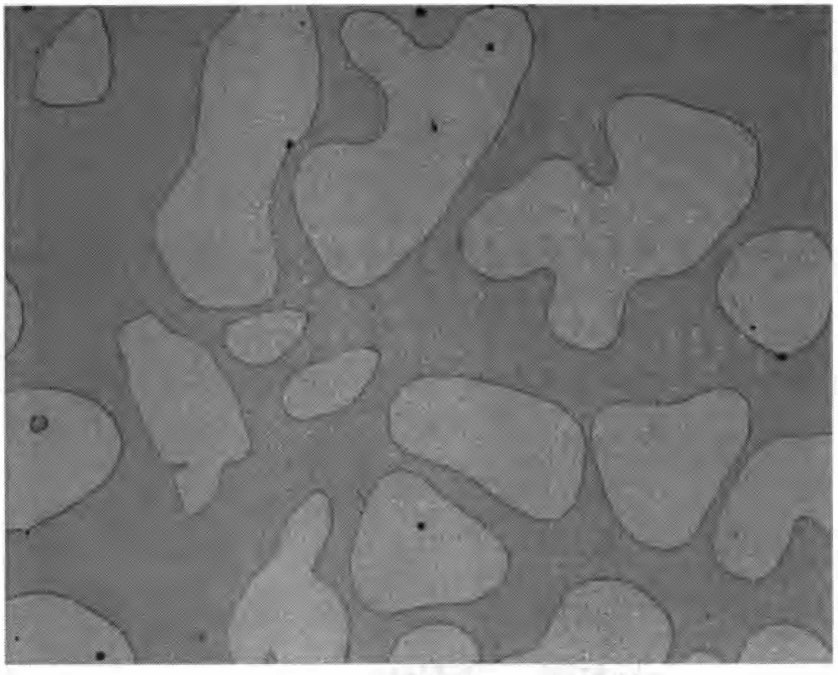


Figure 113. Microstructure of 4A-SA-4, NaOH, 400x

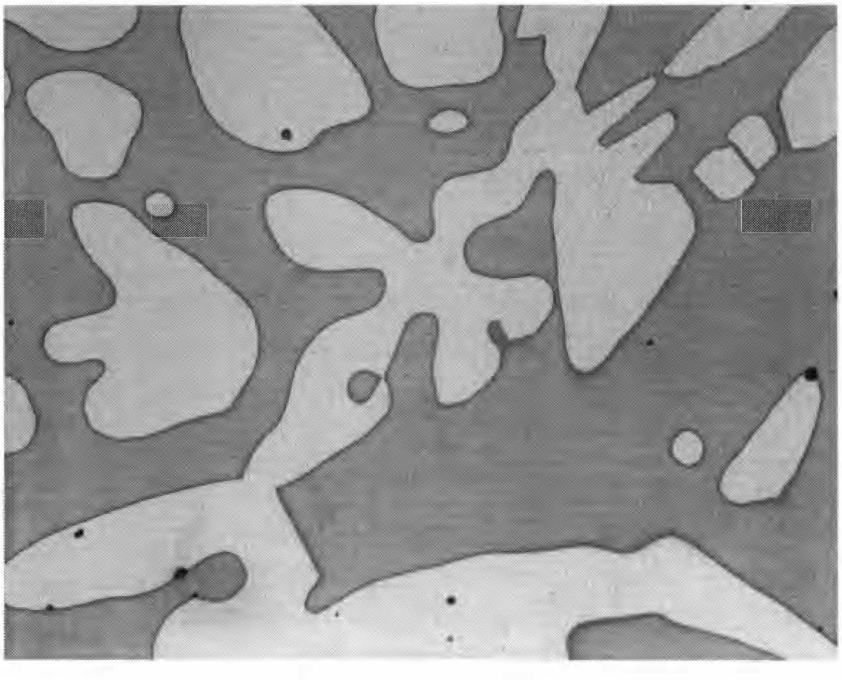


Figure 114. Microstructure of 4A-SA-6, NaOH, 400x

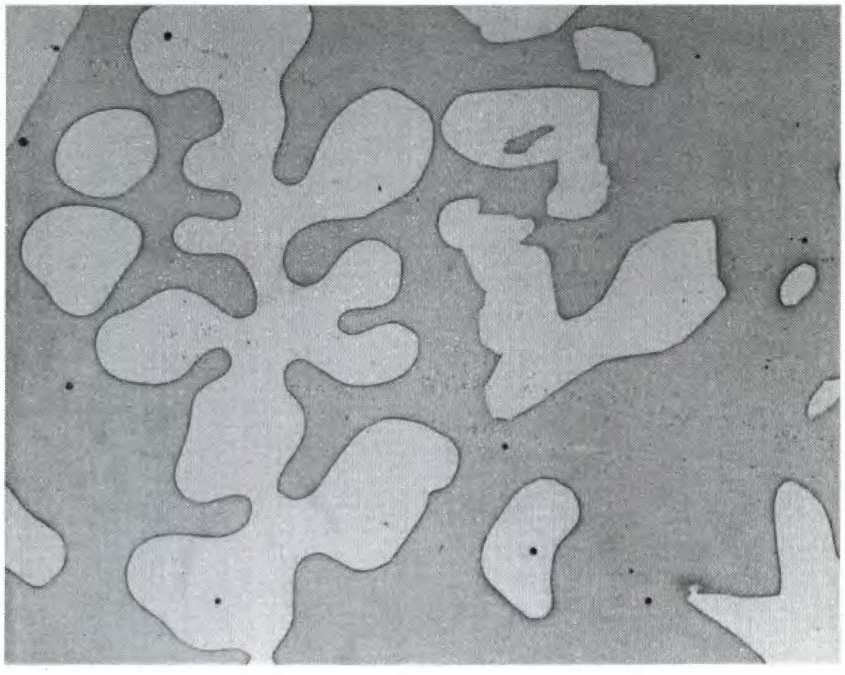


Figure 115. Microstructure of 4A-SA-7, NaOH, 400x

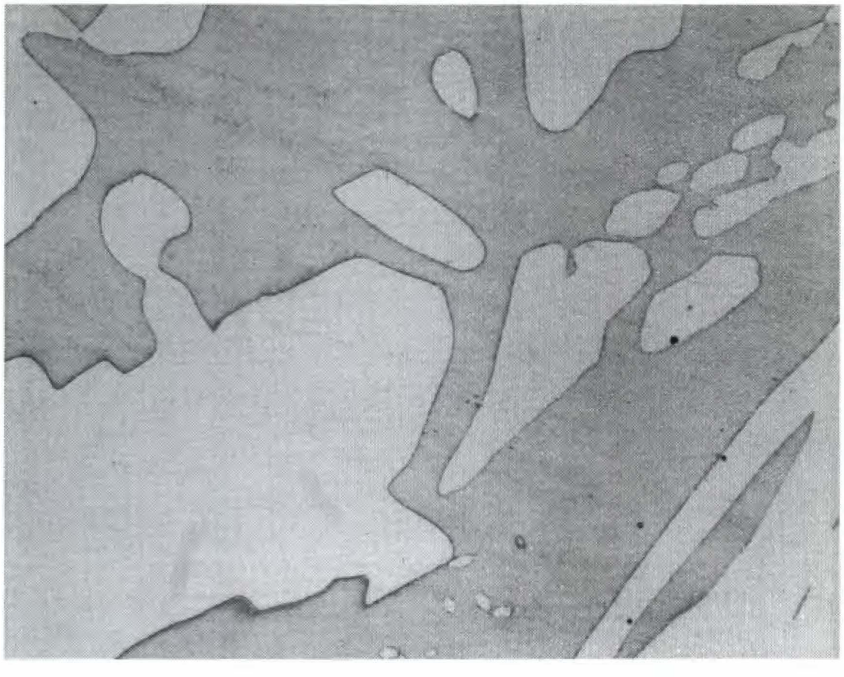


Figure 116. Microstructure of 4A-SA-8, NaOH, 400x

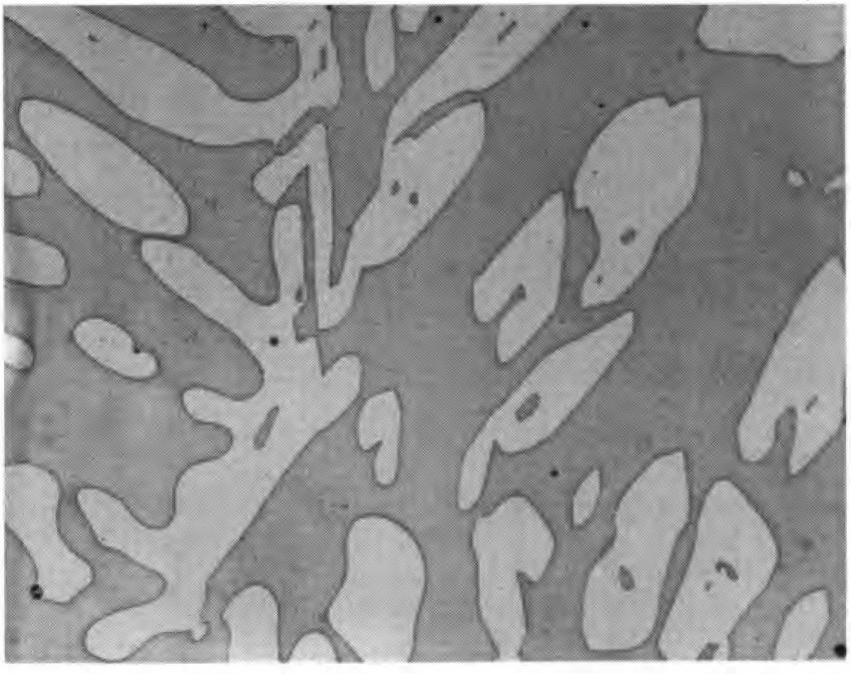


Figure 117. Microstructure of 4A-SA-9, NaOH, 400x

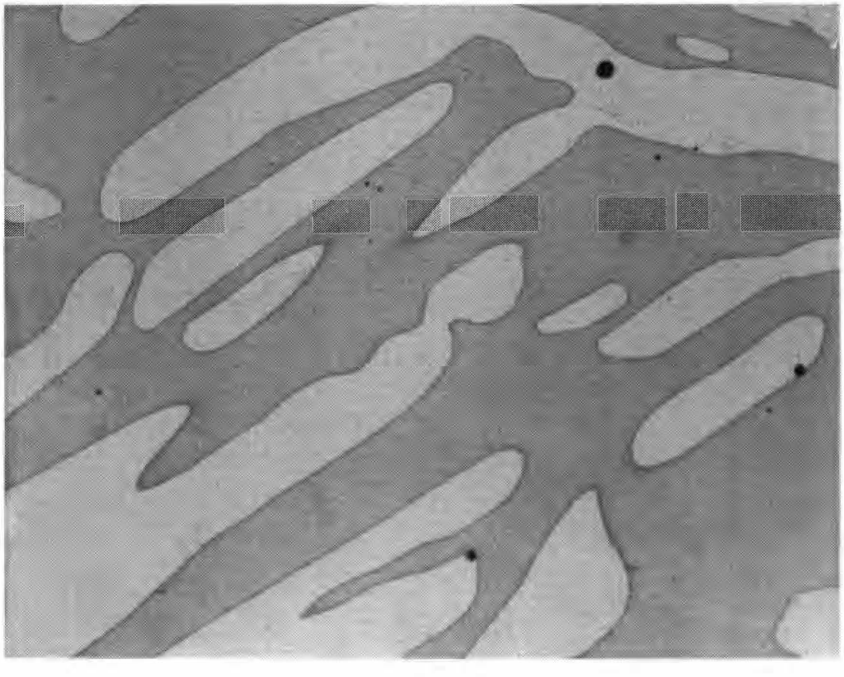


Figure 118. Microstructure of 4A-SA-10, NaOH, 400x

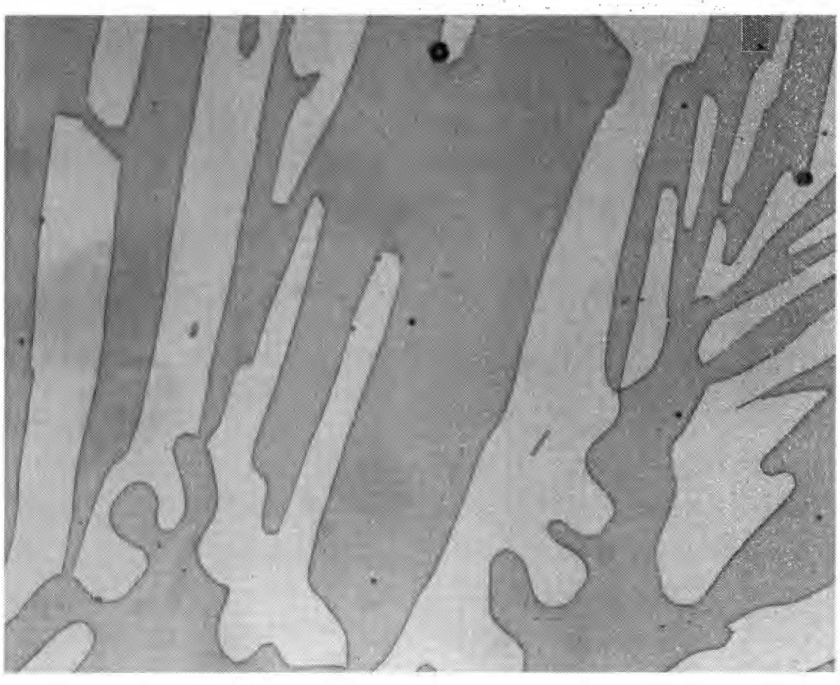


Figure 119. Microstructure of 4A-SA-11, NaOH, 400x

Table 18. Charpy Impact Toughness at –40°C (-40°F) for Foundry Solution Anneal Study

Material ID	Absorbed Energy (ft lbs)	Average Absorbed Energy (ft lbs)
4A-SA-1	1 – 100.5 2 – 100.5	100.5
4A-SA-2	1 – 94.0 2 – 75.5	84.8
4A-SA-3	1 – 79.0 2 –88.5	83.8
4A-SA-4	1 – 85.5 2 – 62.0	73.8
4A-SA-6	1 – 88.0 2 – 99.5 3 - 97.5 4 – 141.5	95.0
4A-SA-7	1 – 75.0 2 – 66.5 3 – 90.5 4 – 126.5	77.3
4A-SA-8	1 – 43.0 2 – 38.5 3 – 60.0 4 – 33.5	47.2
4A-SA-9	1 – 79.5 2 – 64.5 3 – 82.0 4 – 108.5	75.3
4A-SA-10	1 – 73.5 2 – 44.0 3 – 54.5 4 – 107.0	57.3
4A-SA-11	1 – 59.5 2 – 75.5 3 – 62.5 4 – 108.0	65.8

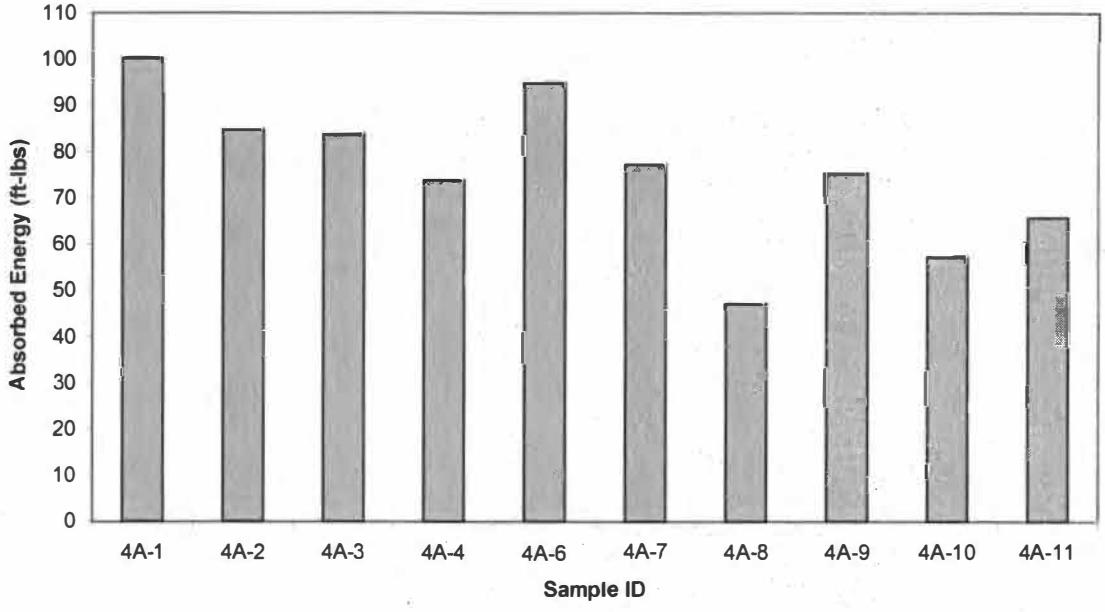


Figure 120. Charpy Impact Toughness at –40°C (-40°F) for Foundry Solution Anneal Study

Table 19. Corrosion Rates for Foundry Solution Anneal Study

Material ID	Corrosion Rate (mdd)
4A-SA-1	0.00
4A-SA-2	0.00
4A-SA-3	0.00
4A-SA-4	0.00
4A-SA-6	0.00
4A-SA-7	0.00
4A-SA-8	0.00
4A-SA-9	0.00
4A-SA-10	0.00
4A-SA-11	0.00

All foundry solution annealed castings passed ASTM A923 requirements. No intermetallic phases were evident in any of the samples per ASTM A923 method A (Figures 37-46). All samples showed average Charpy impact energies greater than 40 ft-lbs at -40°C per ASTM A923 method B (Figure 36). No weight loss was evident in any of the samples when exposed to a ferric chloride test solution per ASTM A923 method C (Table 10). Testing of the 10 heats of A890-4A (CD3MN) after a foundry solution annealing heat treatment shows that the specified foundry solution anneal was adequate to produce castings free from intermetallic phases.

VI. Conclusions

1. Lab-to-lab reproducibility of ASTM E562 is excellent for determining the amount of ferrite in cast DSS.
2. Both ASTM E562 and the Feritescope® are viable methods for determining the amount of ferrite present in DSS with ASTM E562 being more accurate. However, the Feritescope® is quicker and is also non-destructive.
3. Several factors such as operator bias, grid spacing, and specimen metallography can affect the accuracy of ferrite determination per ASTM E562.
4. ASTM A923 Methods adequately identify the presence of detrimental intermetallic precipitates in both wrought and cast DSS.
5. Cast DSS material gave results similar to those of wrought DSS in all three ASTM A923 methods.
6. The presence of detrimental intermetallic precipitates, per ASTM A923 Method A, is easier to identify in cast DSS than in wrought DSS.
7. The micrographs obtained in this study (Figures 106 - 109) can be used when incorporating A890-4A (CD3MN) cast materials into ASTM A923.
8. ASTM A923 Method B impact toughness testing in cast and wrought DSS is the most sensitive of the 3 methods for detecting the presence of intermetallic phases. Method A etch testing is adequate for detecting the presence of intermetallic phases but this method introduces operator bias as it requires greater skills to interpret the results. Method C corrosion weight loss testing is the least sensitive for detecting intermetallic phases.

9. Isothermal holds at 1550°C showed a steady progression in the formation of secondary phases.
10. "H" heat treatment (furnace cooled) was the most egregious thermal treatment as samples failed all ASTM A923 tests.
11. All "G" heat treatment (air cooled) samples passed Method A and Method C testing but showed low impact toughness per Method B.
12. Lab-to-lab reproducibility of microstructure classification per ASTM A923 method A is excellent for ASTM A890-4A cast DSS.
13. Lab-to-lab reproducibility of corrosion performance per ASTM A923 method C is excellent for ASTM A890-4A cast DSS unless there are "high" amounts of intermetallic phases present.
14. ASTM A923 is a viable standard for detecting the presence of detrimental intermetallic phase in ASTM A890-4A cast DSS.
15. The data obtained in this study suggests that ASTM A923 can be expanded to include the cast duplex materials ASTM A890-4A (CD3MN).
16. All foundry solution annealed castings passed ASTM A923 requirements. No intermetallic phases were evident in any of the samples per ASTM A923 method A (Figures 37-46). All samples showed Charpy impact energies greater than 40 ft-lbs at -40°C per ASTM A923 method B (Figure 36). No weight loss was evident in any of the samples when exposed to a ferric chloride test solution per ASTM A923 method C (Table 10).

17. Testing of the 10 heats of A890-4A (CD3MN) after a foundry solution annealing heat treatment shows that the specified foundry solution anneal was adequate to produce castings free from intermetallic phases.

References

1. Gunn, R., ed. *Duplex Stainless Steels – Microstructure, Properties, and Applications.* 1997, Abington Publishing: Cambridge England.
2. Soulignac P, Dupoiron F: *Stainless Steel Europe*, June 1990, 18-21.
3. Chung, H.M., Chopra, O.K., "Characterization of Duplex Stainless Steels by TEM, SANS, and APFIM Techniques," *Characterization of Advanced Materials*, Edited by W. Altergott and E. Henneke, Plenum Press, New York, 1991, pp. 123-147.
4. Roscoe C.V., Gradwell KJ, Lorimer GW: Goteborg '84, Vide ref 6, 563-577.
5. Sedriks AJ: *International Metal Reviews* **28**, 1983, 295.
6. Charles J.: Proc conf *Duplex Stainless Steels '94*, Glasgow, TWI, 1994, Vol. 1, paper KI.
7. Okamoto H.: Conf proc *Applications of Stainless Steel '92*, Stockholm, Jernkontoret, 1992, Vol 1, 360-369.
8. Nilsson J.-O, Jonsson P, Wilson A: Glasgow '94, vide ref. 1, Vol. 2, paper 39.
9. Hertzman S., Nilsson M., Jargelius-Pettersson R.: Glasgow '94, vide ref. 1, Vol. 1, paper 1.
10. Nilsson J.-O.: *Materials Science and Technology* **8**, 1992, 685-700.
11. Lundin, C.D., Wen, S., Zhou, G., Ruprecht, W., W. Liu, G. Lu, "Duplex Stainless Steels, A State-of-the Art Literature Review," *Steel Founders' Society of America Report Special Report No. 31*, March 2001.
12. Nilsson, J.-O., Wilson, A., Huhtala, T., Karlsson, L., Jonsson, P., "Structural Stability of Super Duplex Stainless Weld Metals and Its Dependence on Tungsten

and Copper," *Metallurgical and Materials Transactions A*, 27A (8), Aug. 1996, pp. 2196-2208.

13. Josefsson, B., Nilsson, J.-O., Wilson, A., "Phase Transformation in Duplex Steels and the Relation Between Continuous Cooling and Isothermal Heat Treatment," *Duplex Stainless Steels '91*, Vol. 1, pp. 67-78.
14. Southwick P.D., Honeycombe RWK: *Metal Science* 14(7), 1980, p. 253.
15. Hochman J. et al: MC 50-1, 1974/5.
16. Josefsson B., Nilsson J.-O., Wilson A.: Beaune '91, vide ref. 2, Vol. 1, 67-78.
17. Ravindranath, K., Malhotra, S.N., "Influence of Aging on Intergranular Corrosion of a 25%Cr-5%Ni Duplex Stainless Steel," *Corrosion*, 50(4), 1994, pp. 318-328.
18. Cheng, T.P., Tsai, W.T., Lee, J.T., "Electrochemical and Corrosion Behavior of Duplex Stainless Steels in Hank's Solution," *Journal of Materials Science*, 25(2A), Feb. 1990, pp. 936-943.
19. Sriram, R., Thomas, D., "Pitting Corrosion of Duplex Stainless Steels," *Corrosion*, 45(10), Oct., 1989, pp. 804-810.
20. Machado, I.F., Padilha, A.F., "Precipitation Behavior of 25% Cr – 5.5% Ni Austenitic Stainless Steel Containing 0.87% Nitrogen," *Steel Research*, 67(7), July 1996, pp. 285-290.
21. Radenkovic, G., Cvijovic, Z., Mihajlovic, D., "Effect of Quenching Temperature on the Microstructure and Properties of Cast Duplex Stainless Steel," *Acta Stereol*, 13(2), 1994, pp. 439-444.

22. Lai, J.K.L., Wong, K.W., Li, D.J., "Effect of Solution Treatment on the Transformation Behavior of Cold-Rolled Duplex Stainless Steels," *Materials Science and Engineering A*, 203(1-2), Nov. 1995, pp.356-364.

23. Charles, J., "Composition and Properties of Duplex Stainless Steels," *Welding in the World*, Vol. 36, 1995, pp. 43-55.

24. Kuroda, T., Matsuda, F., "Role of Secondary Austenite on Corrosion and Stress Corrosion Cracking of Sensitized Duplex Stainless Steel Weldments," Transactions of *JWRI*, 23(2), 1994, pp. 205-211.

25. Kotecki, D.J.a.S., T.A., "Heat Treatment of Duplex Stainless Steel Weld Metals," *Welding Journal*, 1989. 68(11): pp. 431s-441s.

26. Nilsson, J.-O., "Overview: Super Duplex Stainless Steels," *Materials Science and Technology*, 1992. 8(8): pp. 686-700.

27. Ogawa, T.a.K., T., "Effect of Composition Profiles on Metallurgy and Corrosion Behavior of Duplex Stainless Steel Weld Metals," *Welding Journal*, 1998. 68(5): pp. 181s-191s.

28. Miura, M., Koso, M., Hudo, T., Tsuge, H., "The Effects of Nickel and Nitrogen on the Microstructure and Corrosion Resistance of Duplex Stainless Steel Weldments," *Welding International*, 1990. 4(3): pp. 200-206.

29. Bernhardsson, S., "The Corrosion Resistance of Duplex Stainless Steels," *Duplex Stainless Steels 91*, 1991.

30. Gooch, T.G., "Corrosion Resistance of Welds in Duplex Stainless Steels," *Duplex Stainless Steel 91*, 1991.

31. Karlsson, L.a.P., S., "Influence of Intermetallic Phases on the Corrosion Properties of Duplex Stainless Steel Weld Metals," *Welding International*, 1995. 9(7): pp. 554-562.

32. Adhe, K.N., Kain, V., Madangopal, K., Gadiyar, H.S., "Influence of Sigma-Phase Formation on the Localized Corrosion Behavior of a Duplex Stainless Steel," *Journal of Materials Engineering and Performance*, 1996. 5(4): pp. 500-506.

33. Ravindranath, K.a.M., S.N., "The Influence of Aging on the Intergranular Corrosion of 22 Chromium – 5 Nickel Duplex Stainless Steel," *Corrosion Science*, 1995. 37(1): pp. 121-132.

34. Otero, E., Merino, C., Fosca, C., Fernandez, P., "Electrochemical Characterization of Secondary Phases in Duplex Stainless Steel by EPR Test," *Duplex Stainless Steels, 94*. 1994.

35. Merino, P., Novoa, X.R., Pena, G., Porto, E., Espada, L., "Intergranular Corrosion Susceptibility of Austenitic-Ferritic Duplex Stainless Steels: Application of Potentiokinetic Reactivation Tests," *Materials Science and Technology*, 1993. 9(2): pp. 168-171.

36. Nicholls, J.M., "Corrosion Properties of Duplex Stainless Steels: General Corrosion, Pitting and Crevice Corrosion," *Duplex Stainless Steels 94*. 1994.

37. Charles, J. "Super Duplex Stainless Steel: Structure and Properties," *Duplex Stainless Steels*. 1991.

38. Charles, J. "Structure and Mechanical Properties of Duplex Stainless Steels," *Duplex Stainless Steels 94*. 1994.

39. Vander Voort, G.F., "Metallographic Techniques for Duplex Stainless Steels," *Duplex 6th World Conference & Expo*, 2000.

40. Farrar, R.A., "The Importanceof Microstructural Transformations for Welding and the Stability of Long Term Service Properties," *Welding in the World*, Vol. 36, 1995, pp. 143-151.

41. Atamert, S., King, J.E., "Elemental Partitioning and Microstructural Development in Duplex Stainless Steel Weld Metal," *Acta. Metall. Mater.*, 39(3), 1991, pp. 273-285.

42. Atamert, S., King, J.E., "Super Duplex Stainless Steels Part I: Heat Affected Microstructures," *Materials Science and Technology*, 7(2), pp. 137-145.

43. Bonnefois, B., Charles J., Dupoiron, F., Soulignac, P., "How to Predict Welding Properties of Duplex Stainless Steels," *Duplex Stainless Steel '91*, Vol.1, 1991, pp. 347-361.

44. Cao, H.L., Hertzman, S., "The Realtionship between Impact Properties and Welding Simulated Microstructures in Three Duplex Stainless Steels," *Duplex Stainless Steel '91*, Vol. 1, 1991, pp. 363-372.

45. Lindbolm, B.E.S., Hannerz, N., "Austenite Reformation in HAZ of Ferritic Austenitic Steels," *Duplex Stainless Steels '91*, Vol. 2, 1991, pp. 951-958.

46. Dufrance, J.J., "Heat Affected Zone Simulation of Super Duplex Stainless Steel UNS S 32760 – Zeron 100," *Duplex Stainless Steel '91*, Vol. 2, 1991, pp. 967-975.

47. Draugelates, U., Schram, A., Boppert, C., Liu, J., "Investigation on the Effect of the Peak Temperature and Cooling Time on the Heat Affected Zone in Duplex Cast Steel," *Duplex Stainless Steel '91*, Vol. 2, 1991, pp. 977-984.

48. Draugelates, U., Schram, A., Boppert, C., "Effect of the Thermal Welding Process Conditions on the Structure and Properties in the Heat Affetced Zone of Duplex Cast Steel," *Duplex Stainless Steel '91*, Vol. 2, 1991, pp. 985-992.

49. Roberti, R., Nicodemi, W., La Vecchia, G.M., Basha, Sh., "Fracture Toughness of Simulated Duplex Stainless Steel Heat Affected Zones," *Duplex Stainless Steel '91*, Vol. 2, 1991, pp. 993-1000.

50. Boppert, C., Draugelates, U., "Mechanical Properties and Corrosion Resistance of Welded Superduplex Cast Alloys," *Duplex Stainless Steel '94*, Vol. 3, Paper 73.

51. Lippold, J.C., Lin, W., Brandi, S., Varol, I., Baeslack III, W.A., "Heat Affected Zone Microstructure and Properties in Commercial Duplex Stainless Steels," *Duplex Stainless Steel '94*, Vol. 1, 1994, Paper 116.

52. Kivineva, E.I., Hannerz, N.E., "The Properties of Gleeble Simulated Heat Affected Zone of SAF 2205 and SAF 2507 Duplex Stainless Steels," *Duplex Stainless Steel '94*, Vol. 1, 1994, Paper 7.

53. Hoffmeister, H. Lothongkum, G., "Quantitative Effects of Nitrogen Contenets and Cooling Rates on δ-γ transformation, Chromium Nitride Precipitation and Pitting Corrosion after Weld Simulation of Duplex Stainless Steels," *Duplex Stainless Steel '94*, Vol. 1, 1994, Paper 55.

54. Jana, S.,"Effect of Heat Input on the HAZ Properties of Two Duplex Stainless Steels," *Journal of Materials Processing Technology*, Vol. 33, 1992, pp. 247-261.

55. Ferreira, P.J., Hertzman, S., "δ-Ferrite Grain Growth in Simulated High Temperature HAZ of Three Duplex Stainless Steels," *Duplex Stainless Steel '91*, Vol. 2, Edited by J. Charles, S. Bernhardsson, pp. 959-966.

56. Lindblom, B.E.S., Lundvist, B., Hannerz, N.E., "Grain Growth in HAZ of Duplex Stainless Steels," *Duplex Stainless Steel '91*, Vol. 1, Edited by J. Charles, S. Bernhardsson, pp. 373-381.

57. Atamert, S., Reed, R.C., King, J.E., "Modeling of Multipass Duplex Stainless Steel Weld Deposit Microstructures," *Duplex Stainless Steel '91*, Vol. 1, Edited by J. Charles, S. Bernhardsson, pp. 393-402.

58. Walker, R.A., Noble, D.N., "Effect of Welding Conditions on Corrosion Resistance of Duplex Stainless Steels," Proceedings: *Weldability of Materials*, Edited by R.A., Patterson, K.W., Mahin, Oct. 1990, pp. 117-125.

59. Lundvist, B., Norberg, P., "Weldability Aspects and Weld Joint Properties of Duplex Stainless Steels," *Welding Journal*, 67(7), July 1988, pp. 45-51.

60. Karlsson, L., "Welding Super Duplex Stainless Steels," *Anti-Corrosion Methods and Materials*, 42(6), 1995, pp. 30-35.

61. Varol, I., Lippold, J.C., Baeslack III, W.A., "Welding of Duplex Stainless Steels," Key Engineering Materilas, Vol. 69 & 70, 1992, pp. 217-252.

62. Kotecki, D.J., Siewert, T.A., "WRC-1992 Constitution Diagram for Stainless Steel Weld Metals: A Modification of the WRC-1988 Diagram," *Welding Journal*, 71(5), 1992, pp. 171s-178s.

63. Kotecki, D.J., "Ferrite Control in Duplex Stainless Steel Weld Metal," *Welding Journal*, 65(10), 1986, pp. 352s-361s.

64. Kotecki, D.J., "Extension of the WRC Ferrite Number System," *Welding Journal*, 61(11), 1982, pp. 352-361.

65. Schaeffler, A., "Constitution Diagram for Stainless Steel Weld Metal," *Metal Progress*, 56(5), 1949, pp. 680, 680B.

66. Delong, W.T., "Ferrite in Austenitic Stainless Steel Weld Metal," *Welding Journal*, 53(7), 1974, pp. 273s-286s.

67. Lake, F.B., "Effect of Cu on Stainless Steel Weld Metal Ferrite Content, " Paper Presented at AWS Annual Meeting, 1990.

68. Kotecki, D.J., "Ferrite Measurement and Control in Duplex Stainless Steel Welds," *Proceedings of Weldability of Materials*, ASM International, Oct. 1990, pp. 127-133.

69. Kotecki, D.J., "Duplex Alloy Weld Ferrite Content: Measurement and Mechanical Property effects," *ASM Metal/Materials Technology Series*, 8201-021, Oct. 1982.

70. Lefebvre, J., "Guidance on Specifications of Ferrite in Stainless Steel Weld Metal," *Welding in the World*, 31(6), Nov./Dec. 1993, pp. 390-406.

71. "Standard Procedures for Calibrating Magnetic Instruments to Measure the Delta Ferrite Content of Austenitic and Duplex Austenitic-Ferritic Stainless Steel Weld Metal," *ANSI/AWS A4.2-91*, American Welding Society, February 1991.

72. Neumaier, P. "ON-site Eddy Current Measurement of Ferrite Content in Austenitic and Duplex Steel Components," *Materials Evaluation*, 48(9), Sept. 1990, pp. 1065-1072.

73. Kotecki, D.J., "Ferrite Determination in Stainles Steel Welds – Advances Since 1974," *Welding Journal*, 76(1), 1997, pp. 24s-37s.

74. Brantsma, L.H., Nijhof, P., "Ferrite Measurements: An Evaluation of Methods and Experiences." *Duplex Stainless Steel '86*, Netherlands, 1986, Paper 45.

75. Taylor, R., "Duplex Stainless Steel Production," SFSA T&O Conference, 1994.

76. Nelson, D.E., Baselack III, W.A, Lippold, J.C., "An Investigation of Weld Hot Cracking in Duplex Stainless Steels," *Welding Journal*, 66(8), 1987, pp. 241s-250s.

77. Lippold, J.C., Baeslack III, W.A., Varol, I., "Heat Affected Zone Liquation Cracking in Austenitic and Duplex Stainless Steels," *Welding Journal*, 71(11), 1992, pp. 387s-396s.

78. Shinozaki, K., Ke, L., North, T.H., "Hydrogen Cracking in Duplex Stainless Steel Weld Metal," *Welding Journal*, 71(11), 1992, pp. 387s-396s.

79. Ogawa, K., Miura, M., "Hydrogen Cracking in Duplex Stainless Steel Weldments," *Welding International*, 5(9), 1991, pp. 691-696.

80. Kotecki, D.J., "Phase Transformations and Weldability of Duplex Stainless Steels," *Proceedings: The First United States – Japan Symposium on Advances in Welding Metallurgy*, June 1990, pp. 251-263.

81. Hoffmeister, H., Volden, L., Grong, O., "Hydrogen Induced Weld Cracking of Duplex Stainless Steels as Affected by Shielding Gas Composition with TIG Welding," *Duplex Stainless Steels '94*, Vol. 1, Part III, 1994, Paper 54.

82. van der Mee, V., Meelker, H., van Nassau, L., "How to Avoid Hydrogen Cracking in (Super) Duplex Stainless Steel Weldments," *Duplex Stainless Steels '94*, Vol. 1, Part III, 1994, Paper 119.

83. Fang, P.J., Kirkwood, D., Power, L.J., Baxter, C.F.G., "The Resistance of Super Duplex Stainless Steel to Hydrogen Cracking," *Duplex Stainless Steels '94*, Vol. 1, Part III, 1994, Paper 51.

84. Lundin, C.D. et al, "Measurement of Diffusible Hydrogen and Hydrogen Effects on the Weldability of 2205/2209 Duplex Stainless Steel."

85. Walker, R.A., Gooch, T.G., "Hydrogen Cracking of Welds in Duplex Stainless Steel," *Duplex Stainless Steels '91*, Vol. 2, 1991, pp. 1053-1063.

86. van Nassau, Meelker, H., Hilkes, J., "Welding Duplex and Super Duplex Stainless Steels," *Welding in the World*, 31(5), Sept./Oct. 1993, pp. 322-343.

87. Bekkers, K., "Practice in Welding Duplex and Super Duplex Stainless Steel Worldwide," *Welding in the World*, Vol. 36, 1995, pp. 111-123.

88. Noble, D.N., Gunn, R.N., "Welding of Duplex Stainless Steel – A Reader's Digest: Part 1," *Stainless Steel Europe*.

89. Fager, S. –A. Odegard, L., "Influence of Different Welding Conditions on Mechanical Properties and Corrosion Resistance of Sandvik SAF 2507," *Corrosion Review*, 11(3-4), 1993, pp.83-100.

90. Hilkes, J., Bekkers, K., "Welding Duplex Stainless Steel," *Welding Journal*, 74(11), Nov.1995, pp. 51-54.

91. Holmberg, B., "Welding of Super Duplex Steel Avesta 2507," *Welding Review International*, 11(1), 1992, pp. 22-27.

92. Doyen, R., Niset, M., "Welding of Duplex and Super Duplex Stainless Steels," *Duplex Stainless Steels '91*, Vol. 2, 1991, pp. 1043-1051.

93. Karlsson, L., Pak, S., "Welding of Duplex Stainless Steels – Properties of SMAW-, FCAW-, and SAW- Welded Joints," *Duplex Stainless Steels '91*, Vol. 1, 1991, pp. 413-420.

94. Kotecki, D.J., Hilkes, J., "Welding Process for Duplex Stainless steels," *Duplex Stainless Steels '94*, Vol. 2, 1994, Keynote Paper KVI.

95. "Guidelines for Welding Zeron 100 Super Duplex Stainless Steel," Weir Materials, Ltd.

96. Geipl, H., "Gas Mixture MAG (GMA) Welding of Corrosion Resistant Duplex Steels – Effect of Shielding Gas and Process Variations," *Duplex Stainless Steels '91*, Vol. 2, 1991, pp 1027-1034.

97. Gouch, P.C., Farrar, J.C.M., "Factors Affecting Weld Root Run Corrosion Performance in Duplex and Super Duplex Pipework," *Duplex Stainless Steels '91*, Vol. 2, 1991, pp. 1009-1025.

98. Bjorkman, G., Odegard, L., Fager, S.A., "Submerged Arc Welding of Sandvik 2507 with Different Heat Inputs. Mechanical Properties and Corrosion Resistance," *Duplex Stainless Steels '91*, Vol. 2, 1991, pp. 1035-1042.

99. Suutala, N., Takalo, T., Moisio, T., "Ferritic-Austenitic Solidification Mode in Austenitic Stainless Steel Welds," *Metallurgical Transaction*, 11A, 1980, pp. 717-725.

100. Homberg, B., "Filler Metal Selection for Optimum Duplex Weldment Properties in Steel UNS 31803," *Duplex Stainless Steels '94*, Vol. 1, Part II, 1994, Paper 93.

101. Karlsson, L., Andersson, S.L., Huhtala, T., "New Ni-base Consumables for Welding of Duplex and Super Duplex Stainless Steels," *Duplex Stainless Steels '94*, Vol. 1, Part II, 1994, Paper 42.

102. Urmstom, S.A., Creffield, G.K., Cole, M.A., Huang, W., "Effect of Nitrogen Containing Shielding Gases on the Weldability and Corrosion Performance of Duplex Stainless Steels," *Duplex Stainless Steels '94*, Vol. 2, 1994, Paper 27.

103. Gunn, R.N., Anderson, P.C.J., "Development of Special Ar-He-N2 Gases for TIG Welding of Duplex and Superduplex Stainless Steels," *Duplex Stainless Steels '94*, Vol. 2, 1994, Paper 30.

104. Rabensteiner, G. Tosch, J., "The Specific Effect of Nitrogen in the Fabrication of a Super Duplex Stainless Steel Weld," *Duplex Stainless Steel '94*, Vol. 2, 1994, Paper 44.

105. Bradshaw, R., Cottis, R.A., "The Effect of Nitrogen Additions to Argon Shielding Gases on the properties of Duplex Stainless Steel GTA Welds," *Duplex Stainless Steels '94*, Vol. 2, 1994, Paper 31.

106. Bonnefois, B., Soulignac, P., Charles J., "Some Aspects of Nitrogen Introduction in the Duplex Weld Pool, " *Duplex Stainless Steels '91*, Vol. 1, 1991, pp. 469-478.

107. Stenbacka, N., Persson, K.A., Runnerstam, O., "Shielding Gas Technology when Ordinary and High Alloyed Stainless Steels," *Welding in the World*, Vol. 36, 1995, pp. 83-90.

108. Bonnet, C., Linden, G., Rouault, P., "A Shielding Gas for the Gas Metal Arc Welding of Duplex and Superduplex Stainless Steels," *Duplex Stainless Steels '94*, Vol. 2, 1994, Paper 102.

109. Fusari, F., Bertoni, A., "Welding of Duplex Stainless Steels: Easy or Difficult?" *Duplex Stainless Steels '94*, Vol. 3, Part II, 1994, Paper 57.

110. Warburton, G.R., Spence, M.A., Healiss, T., "Fabrication and Qualification Experiences with Duplex, Super Duplex, and Super Austenitic Alloys," *Duplex Stainless Steels '94*, Paper 24.

111. Odegard, L., "Welding of Stainless Steels Corrosion in Welds. Effect of Oxides, Slag, and Weld Defects on the Pitting Resistance," *Welding in the World*, Vol. 36, 1995, pp. 153-160.

112. Holmberg, B., "How to Weld Avesta SAF 2507," *Information 9168*, Avesta Welding.

113. Homerg, B., "How to Weld Avesta 2205."

114. Krysiak, K.F., Bhadha, P.M., "Shielding Gas Purification Improves Weld Quality," *Welding Journal*, 69(11), 1990, pp. 47-49.

115. "How to Weld Avesta 2205 Code Plus Two® Duplex Stainless Steel," Avesta Stainless Inc., June 1992.

116. "Your Guide to Easy Welding of Duplex Stainless Steel," Sandvik Steel Co., March 1992.

117. Davidson, R., Redmond, J., "Development of Qualification Tests for Duplex Stainless Steel Mill Products," *Corrosion 9*, 302, 1991.

118. Druce, S.G., Gage, G., Popkiss, E., "Effects of Notch Geometry on the Impact Fracture Behavior of a Cast Duplex Stainless Steel," *The International Journal of Pressure Vessels and Piping*, 33(1), 1988, pp. 59-81.

119. Niederau, H.J., Overbeck, G.W., "high Quality Castings from Duplex and Super-Duplex Stainless Steels for FGD and Off-shore Applications," *Duplex Stainless Steels '94*, Vol. 1, Part III, 1994, Keynote Paper 99.

120. *SCRATA Materials Fact Sheets on Duplex Cr-Ni Steels*, Section D, Apr. 1991.

121. Baxter, C., Young, M., "The Practicalities of Welding Duplex Stainless Steel Process Plant," *Duplex 6th World Conference & Expo*, 2000.

122. Holloway, G.B., Farrar, J.C.M., "Welding Consumables for Duplex and Superduplex Stainless Steels – Optimizing Properties After Heat Treatment," *Duplex 6th World Conference & Expo*, 2000.

123. Baxter, C., Laren, M., "Energy Input Control Nomographs for Welding Duplex and Super Duplex Stainless Steel," *Duplex 6th World Conference & Expo*, 2000.

124. dos Santos, R., Hofmann, E., "On the Control of the Microstructural Development During Solidification of Superduplex Steel Castings," *Duplex 6th World Conference & Expo*, 2000.

125. Charles, J., Verneau, M., "How to Improve Duplex Stainless Steel Properties with Copper Additions," *Duplex 6th World Conference & Expo*, 2000.

126. Salvago, G., Carucci, L., Gariboldi, E., Lecis, N., "Phase Distribution and Electrochemical Behaviour of Centrifugally Cast Duplex Stainless Steel Pipe," *Duplex 6th World Conference & Expo*, 2000.

127. Suk, J., Soo, J., Kim K., "The Effect of W Modification of Duplex Stainless Steel on the Behavior of Precipitation of Secondary Phases and Stress Corrosion Cracking," *Duplex 6th World Conference & Expo*, 2000.

128. Wessman, S., Pettersson, J., "Hydrogen Cracking of Cathodically Polarised Duplex Stainless Steels and Weld Metals," *Duplex 6th World Conference & Expo*, 2000.

129. Bonnet, C., Lethuiller, L., Rouault, P., "Comparison Between Different Ways of Ferrite Measurements in Duplex Welds and Influence on Control Reliability During Construction," *Duplex 6th World Conference & Expo*, 2000.

130. Farina, C., Grassini, U., "Experiences and NDT Controls with Duplex Stainless Steels in Chemical and Refinery Plants," *Duplex 6th World Conference & Expo*, 2000.

131. Karlsson, L., Rigdal, S., Pak, S., "Effects of Elemental Distribution on Precipitation Behaviour and Properties of Duplex Stainless Steel Weldments," *Duplex 6th World Conference & Expo*, 2000.

132. Jimenez, J.A., Ruano, O.A., Allende, R., Torralba, M., Carsi, M., "Effect of Composition on the Mechanical Properties of Two Duplex Stainless Steels," *Duplex 6th World Conference & Expo*, 2000.

133. Lee, C.S., Ahn, J.S., Lee, A., Kim, K.T., Park, C.G., Kim, K.Y., "Effect of χ-phase Precipitation on the Mechanical Properties of Duplex Stainless Steels," *Duplex 6th World Conference & Expo*, 2000.

134. "Your Guide to Easy Welding of Duplex Stainless Steel," Sandvik Steel, March 1992.

135. "Ferrite Measurement in Austenitic and Duplex Stainless Steel Castings," Ruprecht, W.J., December 1999.

136. "Fabrication and Service Performance of Welded Duplex Stainless Steels," Newman, V.

Appendix: Specifications

1. ASTM A890-94: "Standard Specification for Castings, Iron-Chromium-Nickel-Molybdenum Corrosion Resistant, Duplex (Austenitic/Ferritic) for General Application"
2. ASTM E562-01: "Standard Test Method for Determining Volume Fraction by Systematic Manual point Count"
3. ASTM A923-94: "Standard Test Methods for Detecting Detrimental Intermetallic Phase in Wrought Duplex Austenitic/Ferritic Stainless Steels"
4. ASTM A370: "Standard Methods and Definitions for mechanical Testing of Steel Products"
5. ASTM E23: "Standard Method for Notch Bar Impact Testing of Metallic Materials"
6. ASTM A799/A 799M-91: "Standard Practice for Stainless Steel Castings, Instrument Calibration, for Estimating Ferrite Content"

Vita

Steven Wayne Russell was born on February 26, 1976. A 1994 honors graduate from Cherokee Comprehensive High School in Rogersville, TN; he began his college career at Walters State Community College in Morristown, TN where he graduated Cum Laude in the spring of 1996 with an Associate of Science degree in Pre-Engineering.

Steven entered Tennessee Technological University in Cookeville, TN in the fall of 1996 where he achieved a Bachelor of Science degree in Mechanical Engineering in the spring of 1999.

In May 1999, Steven began his professional career as a project engineer for Flexial Corporation in Cookeville, TN, where he designed and coordinated the production of edge welded metal bellows and related components.

In January 2002, Steven re-entered academics at the University of Tennessee-Knoxville graduate program under the direction of Dr. Carl D. Lundin. He spent 18 months pursuing a Master of Science degree in Materials Science / Metallurgy prior to his graduation in August 2003.